Doctoral Dissertation
博士論文

Oscillon Formation and 21cm Forest by Ultra-Light Axion-like Particle

$\left(\begin{array}{c}\text{非常に軽いアクシオンによるオシロン形成と}\\ \text{21cm線を用いた観測}\end{array}\right)$

A Dissertation Submitted
for the Degree of Doctor of Philosophy
December 2020

令和 2 年 12 月博士（理学）申請

Department of Physics, Graduate School of Science,
The University of Tokyo

東京大学大学院理学系研究科物理学専攻

Eisuke Sonomoto

園元 英祐

Abstract

While the cosmological constant and cold dark matter (ΛCDM) model succeeds in explaining the large scale structure of the universe, it contains astrophysical problems on small scales around kpc, which represents the excess of the matter density in numerical simulations. Ultra-Light Axion-like Particle (ULAP) generated from the dimensional reduction in string theory is one of the famous solutions to these problems. This is because the cosmological structure below its de Broglie wavelength, which corresponds to the relevant scale $\sim$ kpc if the ULAP mass is about $m \simeq 10^{-22}$ eV, are smeared out by its quantum pressure. When such a light scalar particle oscillates with an $\mathcal{O}(1)$ amplitude in a potential shallower than quadratic, the large fluctuations produced by parametric resonance can create localized dense objects, oscillons. Because of their longevity due to the approximate conservation of the adiabatic invariant, they can survive up to the recent universe around redshift $z \sim \mathcal{O}(10)$. One of the methods to probe the matter structure below the scale Mpc is 21cm line, which is generated from the energy difference due to the hyperfine splitting by the interaction between the electron and proton spins in neutral hydrogen.

In this thesis, we examine the possibility to detect ULAP oscillons by the 21cm forest, which is the consecutive absorption of the 21cm line by dark matter mini-halos. First, to precisely estimate the effect of oscillons on the matter structure, we derive the analytical formula of the oscillon power spectrum and confirm that it reproduces our simulation results. Then, using these values, we calculate the number of intersections of a background source with mini-halos depending on the optical depth. We find that the oscillons can enhance the number of 21cm line absorption when the ULAP mass is smaller than 10^{-19} eV and the fraction of ULAP to dark matter is much larger than 10^{-2} in the case of a monodromy type potential. These results are also applicable to any other scalar potentials that produce long-lived oscillons.

1

Contents

Chapter 1

Introduction

The nature of dark matter which dominates the matter energy density of the universe remains a huge mystery, though various observational results suggest its existence [1, 2, 3]. Thanks to the relentless efforts of cosmological observations over the past decades, especially in the observations of cosmic microwave background (CMB), cosmological constant and cold dark matter (ΛCDM) model with inflation is revealed to be the most promising on large scales among a number of cosmological models [4, 5, 6].

However, looking into the small scales around $\lesssim$ 1kpc, numerical simulations based on the ΛCDM model confronts three astrophysical problems. The first is the missing satellite problem (e.g. [7]): the observed number of sub-halos in Milky Way sized halos is much smaller than that of the simulation results. The second is the core cusp problem (e.g. [8]): the observed central density profiles of dark matter halos are much shallower than that of the simulation results. The last is the too-big-to-fail problem (e.g. [9]): the mass of sub-halos produced in simulations is too big to fail to form bright galaxies inside them. Because all these problems arise from the over-densities on small scales, we are struggling to construct the dark matter model that suppresses the small scale structure while behaves like cold dark matter on large scales.

One of the solutions to these problems is suggested from the perspective of string theory which succeeds in combining quantum field theory and general relativity. Due to the compactification of extra-dimensions and the spontaneous symmetry breaking of string theory, the simultaneous existence of many Axion-Like Particles (ALPs) are indicated over a vast mass range [10, 11]. Particularly, when the ALP mass is extremely small as $m \simeq 10^{-22}$ eV, for example, it is called Ultra-Light Axion-like Particle (ULAP) [12] [1] and could solve the small scale problems by the quantum pressure because the de Broglie wavelength of ULAP

$$\frac{\lambda}{2\pi} = \frac{\hbar}{mv} \simeq 1.92 \text{ kpc} \left(\frac{10^{-22} \text{ eV}}{m} \right) \left(\frac{10 \text{ km/s}}{v} \right), \tag{1.0.1}$$

is the same as the typical scale of the galactic center when $m \simeq 10^{-22}$ eV. It is indeed proved that smoothing out the central over density by the quantum pressure solves the

---

[1] It is also called fuzzy dark matter, wave dark matter, and so on in literature. To avoid confusion we call it ULAP in this thesis.
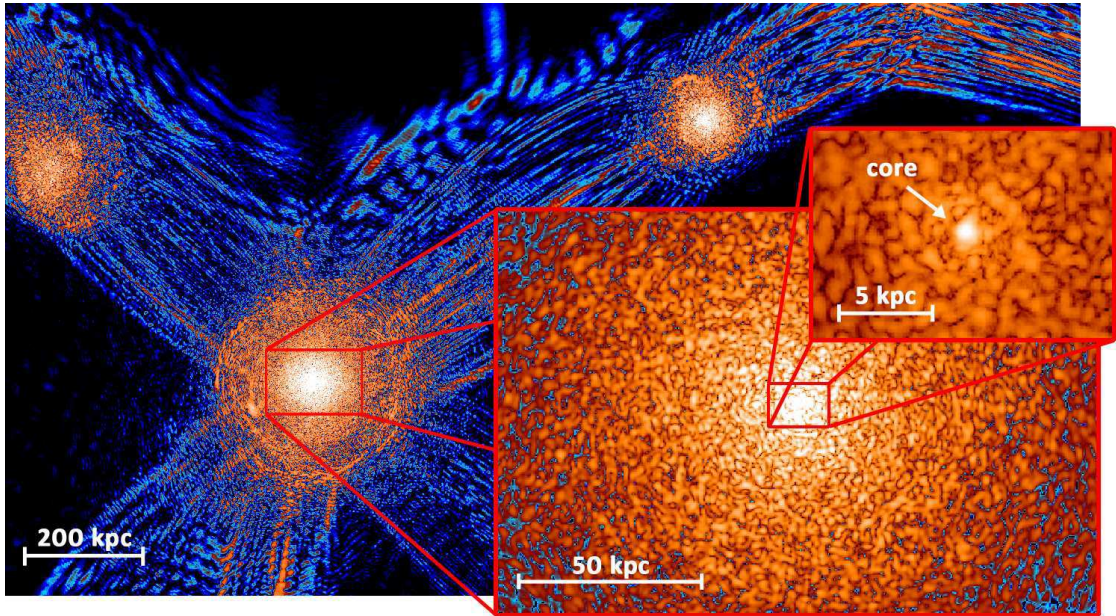
Figure 1.0.1: The simulation result taken from Refs. [13, 14] which shows the energy density of a scalar dark matter such as ULAP at redshift $z = 0.1$. The density is normalized by the cosmic mean density and the color map is logarithmically scaled from $10^{-1} - 10^8$ with cyan corresponding to $\lesssim 10$.

core cusp problem [13, 14, 15] as shown in Fig. 1.0.1 and the other problems are also expected to be solved [16].

In general, ULAP is assumed to be generated before or during inflation and homogeneously distributed over the universe. However, there is a possibility that this scalar particle exists in the form of localized dense objects, oscillons [17, 18, 19]. [2] For oscillon formation, two conditions are necessary; the first is a potential shallower than quadratic and the second is large fluctuations with an $O(1)$ amplitude of ULAP. In the case of ALPs, a lot of potentials satisfying these conditions have already been suggested (e.g. Refs. [27, 28, 29, 30, 31, 32, 33, 34]).

The lifetime of oscillons is generally quite long because of the approximate conservation of the adiabatic charge [35, 36, 37]. The lifetime of oscillons is described as

$$\tau \sim 20 \text{ Gyr} \left(\frac{10^{-22} \text{ eV}}{m} \right) \left(\frac{\Gamma/m}{10^{-11}} \right)^{-1}, \tag{1.0.2}$$

where Γ is the decay rate of oscillons. Thus, if $\Gamma/m \lesssim 10^{-11}$, the produced oscillons can exist even in the current universe. To precisely estimate the oscillon lifetime, the numerical simulation used to be necessary, but the analytical method to calculate the decay rate of oscillons is developed recently in Refs. [38, 39]. While it is revealed that oscillons from the simple cosine type potential which is often assumed in analogy with quantum chromodynamics (QCD) axion is so small $O(100)m^{-1}$ [40], in some other types

---

[2]Oscillons of the axion in quantum chromodynamics (QCD) [20, 21, 22, 23, 24] are called axitons [25, 26].

of potentials, for example, a monodromy type potential [28, 27, 34] the resultant oscillons are proved to be quite long-lived as $\gtrsim \mathcal{O}\left(10^8\right) m^{-1}$ [41, 42].

In the phenomenological point of view, oscillons are mainly discussed with gravitational waves produced by the large fluctuations along with the oscillon formation [43, 44], but in any cases the detection is almost impossible because of its high frequency. However, such long-lived oscillons can open new possibilities for the detection of the scalar particle because we take advantage of the high energy density of oscillons to obtain the clue to it.

The scale affected by oscillons is determined by the the distance between oscillons and the horizon scale at the oscillon formation. Because the typical oscillon distance is the same as the wavenumber of the parametric resonance [45, 46, 47] $\sim m$, and oscillons are generally produced when the scale factor a becomes $\mathcal{O}(10)$ times larger than the initial value determined by the condition $H \simeq m$, the comoving scale affected by oscillon formation is $m/\sqrt{10} \lesssim k/a \lesssim m$, that is,

$$15 \text{ Mpc}^{-1} \left(\frac{m}{10^{-22} \text{ eV}}\right)^{1/2} \lesssim k \lesssim 50 \text{ Mpc}^{-1} \left(\frac{m}{10^{-22} \text{ eV}}\right)^{1/2}, \qquad (1.0.3)$$

One of the methods to explore such a small scale is the 21cm line, [3] which is produced by the hyperfine splitting due to the interaction between the electron and proton spins [48]. The 21cm line is adopted as a useful tracer of the recent universe because neutral hydrogen is ubiquitous in the early universe after the recombination, amounting to $\sim 75\%$ of the gas in the intergalactic medium (IGM). For example, the absorption could be detected as the spectrum distortion of CMB.

If there are luminous radio rich sources such as radio quasars and gamma-ray bursts (GRBs), the emitted continuum spectrum is consecutively absorbed by the neutral hydrogen; this consecutive absorption phenomenon is called 21cm forest [49, 50] in exact analogy with the Lyman-α forest. The absorption could be the most efficient when the emission spectrum goes through the neutral-hydrogen-rich region. Such regions are characterized by the virial temperature smaller than 10^4 K [51] which corresponds to the mini-halo mass $M \lesssim 10^7 M_\odot$ because under this temperature the metal-free cooling necessary for the star formation becomes ineffective and plenty of neutral hydrogen remains. These regions during the epoch of reionization and beyond are called mini-halos.

In this thesis, we study various properties of oscillons produced from a ULAP potential by classical lattice simulation and consider the way to probe ULAP with oscillons.

First, to obtain the matter power spectrum of oscillons, we calculate the mass distribution, the energy ratio, the number density, and the average mass of oscillons after the formation by numerical simulations. [4] Using these values, we compare the simulated density power spectrum to the analytic formula. Then, we study their time evolution by estimating the analytic decay rate of oscillons, which is the first time taking ULAP oscillons including the effects of their decay

---

[3]There is a possibility to probe the different ULAP mass range by the Lyman-α line, which is produced by absorption due to the transition of an electron in a neutral hydrogen atom between the ground state and the first excited state. However, because the precise calculation without numerical simulation is difficult due to the complexity of astrophysical phenomena in the low redshift universe at $z \sim \mathcal{O}(1)$, we focus on the 21cm line in this thesis.

[4]Please see Refs. [52, 53, 54] for similar previous works.

Second, we suggest the new possibility to detect ULAP oscillons by the 21cm forest. In the previous researches [55, 56], the contribution of ULAP to the 21cm forest is discussed, but the possibility of ULAP oscillon formation has never been considered. Here, we assume that dark matter of the universe is consist of unknown cold dark matter, homogeneous ULAP, and ULAP oscillons, and calculate the difference in the number of intersections with mini-halos produced by dark matter.

Throughout this thesis, we use the monodromy type potential [27, 28, 34] in which the oscillon formation and the longevity of produced oscillons has already been confirmed [52, 42, 57], for instance. Note that the procedure in this thesis is quite general and applicable to any other potentials that produce oscillons.

Organization of this Thesis

This thesis is composed of two parts.

Part I shows a review of the basic physics necessary for this thesis. First, in Chap. 2, we review the basics of oscillons and their stability. Next, in Chap. 3 we introduce ULAP from both the theoretical and phenomenological points of view and show cosmological constraints on its mass. In Chap. 4, we briefly describe the basics of the 21cm line and explain the subsequent absorption of the 21cm line, called 21cm forest.

Part II shows our original works based on Refs. [58, 59]. In Chap. 5, following Ref. [58], we analytically derive the matter power spectrum of a scalar field when a part of it exists as oscillons. Then, using a monodromy type potential as an example, we confirm by classical lattice simulation that the analytical result is a good approximation. Next, in Chap. 6, following Ref. [59], making use of the results of the previous section, we focus on the 21cm forest to detect ULAP oscillons and calculate the abundance of the 21cm absorption lines. Finally, in Chap. 7, we conclude our results.

Some of the basic formulae and simulation details relevant to this thesis are summarized in Appendix A, B, C. Please see them as needed.

Notations and Conventions

We summarize the notations and conventions of this thesis below.

- Units: Unless otherwise stated, we work in the "natural" units:

$$\hbar = c = 1, \tag{1.0.4}$$

  where $\hbar$ is the reduced Planck constant and c is the speed of light. We adopt the reduced Planck mass $M_{\mathrm{Pl}} = 1/\sqrt{8\pi G}$ where G is the gravitational constant. Note that we sometimes use centimeter-gram-second (CGS) units following the convention of astrophysics particularly when we mention the 21cm line.

- Metric: We use the metric with the signature $\eta_{\mu\nu} = (+, -, -, -)$ in Minkowski spacetime. When we take into account the cosmic expansion, we work in the spatially flat Friedmann-Robertson-Walker (FRW) universe with metric

$$ds^2 = dt^2 - a^2 \left(dx^2 + dy^2 + dz^2 \right).$$

- Indices: We adopt the Einstein summation convention, which sums over repeated indices as

$$a^i b_i \equiv \sum_i a^i b_i.$$

Greek indices $\mu, \nu, \sigma, \cdots$, etc. denote the four dimensional spacetime running over $0, 1, 2, 3$, while Roman indices $i, j, k, \cdots$, etc. denote only the three spatial component $1, 2, 3$.

- Fourier transformation: In this thesis, Fourier transformation in D dimensions is defined by

$$f(x) = \int \frac{d^D x}{(2\pi)^D} f(k) e^{ik \cdot x}, \tag{1.0.5}$$

$$f(k) = \int d^D k f(x) e^{-ik \cdot x}. \tag{1.0.6}$$

Part I

Review

Chapter 2

Oscillon

In this chapter, we review the basics of oscillon [17, 18, 19]. First, we define the adiabatic invariant in analogy with classical mechanics [60, 35, 36] which supports the stability of oscillons. Second, we derive the equation that the oscillon profile must satisfy and show that a scalar field with a potential shallower than quadratic can produce oscillons. Finally, we explain how to calculate the classical decay rate of oscillons following Refs. [38, 39].

In this chapter, we focus on the Lagrangian of a single scalar field

$$\mathcal{L} = \frac{1}{2} \left(\partial_\mu \phi \right)^2 - V(\phi), \tag{2.0.1}$$

and assume that the potential $V(\phi)$ is dominated by the quadratic term around the potential minimum as

$$V(\phi) = \frac{1}{2} m^2 \phi^2 + V_{\mathrm{nl}}(\phi), \tag{2.0.2}$$

to achieve a periodic motion which is necessary for oscillon formation as we will see later.

2.1 Adiabatic Invariant

In Ref. [35], oscillon is redefined as a configuration that approximately conserves the "adiabatic invariant" which is originally introduced in classical mechanics [60]. In this section, we derive the definition of the adiabatic invariant in scalar field theory in analogy with classical mechanics.

First, let us consider a classical mechanical system executing a finite motion characterized by some time-dependent parameter $\lambda(t)$. In such a system, "adiabatically" means that $\lambda(t)$ varies slowly compared to the period of the finite motion T,

$$T \frac{d\lambda}{dt} \ll \lambda. \tag{2.1.1}$$

Although the energy of the system E is not conserved in this case, there must be a relation between λ and dE/dt (the rate of change of the energy) because λ is only slowly varying. In other words, we can define a combination of E and λ which remains constant during the motion. In classical mechanics, this quantity is called "adiabatic invariant".

Let us briefly derive the adiabatic invariant I in a simple classical mechanical system. Suppose that $H(p, q; \lambda)$ be the Hamiltonian of the system where q and p are the coordinate and momentum. The rate of change of the energy averaged over the period of the motion T in which λ remains constant is described by

$$\overline{\frac{dE}{dt}} = \frac{d\lambda}{dt} \frac{1}{T} \int_0^T \frac{\partial H}{\partial \lambda} dt, \tag{2.1.2}$$

because of the adiabaticity of λ. Using Hamilton's equation $dq/dt = \partial H/\partial p$, we can define the integration over the complete range of coordinate variation during the period $\oint$ as

$$T = \int_0^T dt \equiv \oint dq \left(\frac{\partial H}{\partial p} \right)^{-1}. \tag{2.1.3}$$

Then, the integration of time in Eq. (2.1.2) is transformed into that of the coordinate q as

$$\overline{\frac{dE}{dt}} = \frac{d\lambda}{dt} \frac{\oint \frac{\partial H}{\partial \lambda} dq \left(\frac{\partial H}{\partial p} \right)^{-1}}{\oint dq \left(\frac{\partial H}{\partial p} \right)^{-1}}. \tag{2.1.4}$$

Because the adiabaticity makes λ constant during one period of the motion, the Hamiltonian also remains constant $H(p, q; \lambda) = E$ and the momentum is expressed as a definite function of the coordinate q, that is, $p = p(q; E, \lambda)$. Therefore, putting them and differentiating $H(p, q, \lambda) = E$ by λ, we have

$$\frac{dH}{d\lambda} = \frac{\partial H}{\partial \lambda} + \frac{\partial H}{\partial p} \frac{\partial p}{\partial \lambda} = 0. \tag{2.1.5}$$

Substituting it for Eq. (2.1.4), we obtain

$$\overline{\frac{dE}{dt}} = -\frac{d\lambda}{dt} \frac{\oint \frac{\partial p}{\partial \lambda} dq}{\oint \frac{\partial p}{\partial E} dq}, \tag{2.1.6}$$

$$\Leftrightarrow \quad \oint \left(\frac{\partial p}{\partial E} \overline{\frac{dE}{dt}} + \frac{\partial p}{\partial \lambda} \frac{d\lambda}{dt} \right) dq = 0. \tag{2.1.7}$$

Thus, we can easily find that if we define the adiabatic invariant I as

$$I \equiv \frac{1}{2\pi} \oint p \, dq, \tag{2.1.8}$$

where the integral is taken over the path for given E and λ, I remains constsant. The coefficient 2π is taken so that the partial derivative of E coincides with the frequency $\omega \equiv 2\pi/T$ as

$$2\pi \frac{\partial I}{\partial E} = \oint \frac{\partial p}{\partial E} dq = T. \tag{2.1.9}$$

$$\therefore \quad \frac{\partial E}{\partial I} = \omega.$$

from Eq. (2.1.3). This is the definition of the adiabatic invariant of a system with a single degree of freedom in classical mechanics.

To extend it to scalar field theory, we need to consider a system with multiple degrees of freedom executing a finite motion in all the coordinates. In general, the motion of a system with multiple degrees of freedom is not strictly periodic. However, when the canonical variables of the system are separable, in the course of a sufficient time the system gets arbitrarily close to the given state [60]. Thus, in scalar field theory we require that the variables are separable, which means that the gradient energy of the system is negligible everywhere.

Given scalar field theory with a Lagrangian

$$V(\phi, \lambda) = \frac{1}{2} m^2 \phi^2 + V_{\mathrm{nl}}(\phi, \lambda). \tag{2.1.10}$$

Note that the potential must be quadratic except for the slowly varying term $\lambda(x)$ because the system must execute a finite motion.

Let us consider the Noether current of spacetime translational transformation,

$$j^\mu \equiv \dot{\phi} \partial^\mu \phi - \eta^{\mu 0} \mathcal{L}, \tag{2.1.11}$$

where the dot represents the time derivative. The rate of change of this current averaged over the period of the motion T is described by

$$\overline{\partial_\mu j^\mu} = (\partial_\mu \lambda) \frac{1}{T} \int_0^T \frac{\partial j^\mu}{\partial \lambda} dt = (\partial_\mu \lambda) \frac{\oint \frac{\partial j^\mu}{\partial \lambda} \frac{d\phi}{\dot{\phi}}}{\oint \frac{d\phi}{\dot{\phi}}}. \tag{2.1.12}$$

where we have defined $\oint$ as the integral over the complete range of the field and further assumed that the space dependence of λ is so weak that

$$\left| \frac{\nabla \lambda}{\lambda} \right| \ll \frac{1}{T}, \tag{2.1.13}$$

to keep the term $\partial_\mu \lambda$ out of the integral $\oint$. Thus, the motion of ϕ is considered to be both periodic and homogeneous in the volume $[\boldsymbol{x} + T/2, \boldsymbol{x} - T/2]$ and the current has a conserved quantity J^μ. Differentiating $j^\nu (\phi, \partial_\mu \phi; \lambda) = J^\nu$ with λ, we obtain

$$\frac{dj^\nu}{d\lambda} = \frac{\partial j^\nu}{\partial (\partial_\mu \phi)} \frac{\partial (\partial_\mu \phi)}{\partial \lambda} + \frac{\partial j^\nu}{\partial \lambda} = 0, \tag{2.1.14}$$

$$\Leftrightarrow \quad \frac{\partial j^\nu}{\partial \lambda} \simeq \dot{\phi} \frac{\partial (\partial_\mu \phi)}{\partial \lambda}, \tag{2.1.15}$$

where we have ignored the non-diagonal terms because they are higher order in $\dot{\lambda}$ and $\nabla \lambda$. Substituting it for Eq. (2.1.12), we have

$$\overline{\partial_\mu j^\mu} = -\partial_\mu \lambda \frac{\oint \frac{\partial (\partial^\mu \phi)}{\partial \lambda} d\phi}{\oint \frac{d\phi}{\dot{\phi}}}, \tag{2.1.16}$$

$$\Leftrightarrow \quad \oint \left[\overline{\partial_\mu j^\mu} \frac{1}{\dot{\phi}} + \partial_\mu \lambda \frac{\partial (\partial^\mu \phi)}{\partial \lambda} \right] d\phi = 0, \tag{2.1.17}$$

$$\Leftrightarrow \quad \oint \left[\overline{\partial_\mu j^\nu} \frac{\partial (\partial^\mu \phi)}{\partial j^\nu} + \partial_\mu \lambda \frac{\partial (\partial^\mu \phi)}{\partial \lambda} \right] d\phi \simeq 0, \tag{2.1.18}$$

$$\Leftrightarrow \quad \overline{\partial_\mu \left(\oint \partial^\mu \phi d\phi \right)} = 0. \tag{2.1.19}$$

Thus, if the adiabatic invariant is defined as

$$I \equiv \frac{1}{m} \int d^3 x \overline{\dot{\phi}^2}, \tag{2.1.20}$$

we can easily find that I remains constant when we ignore the gradient term. Eq. (2.1.20) is the definition of the adiabatic invariant in scalar field theory and we will utilize it to describe the oscillon profile below.

2.2 Oscillon Profile

In this section, we first provide the equation that the spatial profile of oscillon should satisfy and show that the profile equation is realized as the minimum energy state with a given adiabatic charge. We also provide conditions for the existence of the solution as well as the stability of oscillons against perturbations. Throughout this thesis, we focus only on the spherically symmetric solution $\Phi(r)$ because it exhibits the lowest energy configuration.

Let us begin with the Lagrangian of a single scalar field Eq. (2.0.1) which derives the equation of motion of ϕ as

$$\ddot{\phi} - \nabla^2 \phi + m^2 \phi + \frac{dV_{\mathrm{nl}}(\phi)}{d\phi} = 0. \tag{2.2.1}$$

We assume that the oscillon profile $\phi_{\mathrm{osc}}(x)$ is well approximated by a single frequency solution [1] as

$$\phi_{\mathrm{osc}}(x) = \Phi(r) \cos \omega t, \tag{2.2.2}$$

where $\Phi(r)$ is the spatial oscillon profile. Substituting Eq. (2.2.2) for the equation of motion Eq. (2.2.1), we obtain

$$\left(-\omega^2 - \nabla^2 + m^2 \right) \Phi \cos \omega t + \frac{dV_{\mathrm{nl}} \left(\Phi \cos \omega t \right)}{d\phi} = 0. \tag{2.2.3}$$

Multiplying it by $\cos \omega t$ and taking average over the period of the motion, we have the equation of $\Phi(r)$ as

$$\nabla^2 \Phi = \left(m^2 - \omega^2 \right) \Phi + 2 \frac{dU_{\mathrm{nl}}(\Phi)}{d\Phi}, \tag{2.2.4}$$

---

[1]The validity of the approximation of the single frequency solution with a small amplitude is proved in Ref. [39].

where we have defined the time averaged potential $U_{\mathrm{nl}}(\Phi) \equiv \overline{V_{\mathrm{nl}}(\Phi \cos \omega t)}$. To obtain a soliton configuration with finite energy, two boundary conditions are generally imposed as

$$\Phi|_{r \to \infty} = 0, \quad \left.\frac{d\Phi}{dr}\right|_{r \to 0} = 0. \tag{2.2.5}$$

The equation Eq. (2.2.4) with the boundary conditions Eq. (2.2.5) is called the profile equation of oscillons.

This profile equation is also derived as the solution to minimize the time-averaged energy with a given adiabatic invariant [35]. Let us derive it by Lagrangian multiplier method assuming $\phi(x) = \Phi(r) \cos \omega t$. Considering the motion subjected to the constraint $I = I_0$, the Lagrangian function E_λ with λ being the Lagrangian multiplier is calculated as

$$E_\lambda = \overline{E} + \lambda \left(I_0 - \frac{1}{\omega} \int d^3 x \overline{\dot{\phi}^2} \right), \tag{2.2.6}$$

$$= \int d^3 x \left[\left(1 - \frac{2\lambda}{\omega} \right) \frac{1}{2} \overline{\dot{\phi}^2} + \frac{1}{2} \overline{(\nabla \phi)^2} + \frac{1}{2} m^2 \phi^2 + \overline{V_{\mathrm{nl}}(\phi)} \right] + \lambda I_0, \tag{2.2.7}$$

$$= \frac{1}{2} \int d^3 x \left[\frac{1}{2} (\nabla \Phi)^2 + \frac{1}{2} \left(m^2 + \omega^2 - 2\lambda \omega \right) \Phi^2 + 2 U_{\mathrm{nl}}(\Phi) \right] + \lambda I_0, \tag{2.2.8}$$

where we have used the relation $U_{\mathrm{nl}}(\Phi) = \overline{V_{\mathrm{nl}}(\Phi(r) \cos \omega t)}$ in the last line. To derive the minimum (or maximum) energy configuration, we differentiate E_λ by Φ and obtain

$$\nabla^2 \Phi = \left(m^2 + \omega^2 - 2\lambda \omega \right) \Phi + 2 \frac{d U_{\mathrm{nl}}(\Phi)}{d\Phi}, \tag{2.2.9}$$

which is the same as the profile equation Eq. (2.2.4) when we set $\lambda = \omega$. Thus, oscillons is also regarded as the minimum energy configuration for a given adiabatic invariant, which leads to the quasi-stability of oscillons as we will discuss in the next section.

Conditions for the existence of the solution   We have derived the profile equation of oscillons above in single scalar field theory, but not all scalar potentials are allowed to produce oscillons. The necessary condition for solutions to exist is given by

$$\min \left[\frac{U(\Phi)}{\Phi^2} \right] < \omega^2 < m^2. \tag{2.2.10}$$

To understand this condition, let us consider Eq. (2.2.4) in three-dimensional space,

$$\frac{\partial^2 \Phi}{\partial r^2} + \frac{2}{r} \frac{\partial \Phi}{\partial r} = -\frac{d}{d\Phi} \left[\frac{1}{2} \omega^2 \Phi^2 - U(\Phi) \right]. \tag{2.2.11}$$

where

$$U(\Phi) \equiv \frac{1}{2} m^2 \Phi^2 + 2 U_{\mathrm{nl}}(\Phi). \tag{2.2.12}$$

This equation is regarded as the equation of motion of a particle moving in a potential $\omega^2 \Phi^2 / 2 - U(\Phi)$ with r dependent friction. The intuitive picture of this equation is shown
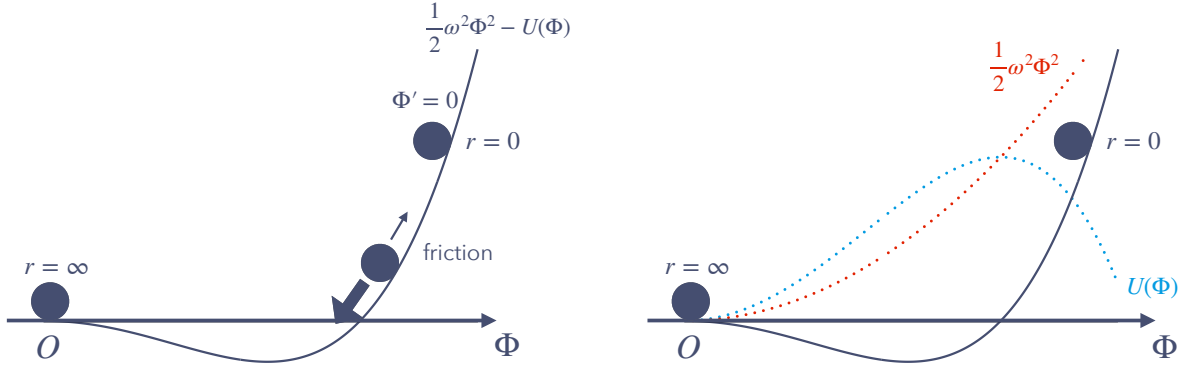
14

Figure 2.2.1: An intuitive picture for the condition of oscillon potential Eq. (2.2.10). The left figure shows that the profile equation Eq. (2.2.4) describes the motion of a particle in the potential $\omega^2\Phi^2/2 - U(\Phi)$ with the boundary conditions Eq. (2.2.5). The right figure shows that the profile equation has the solution only when the potential $U(\Phi)$ is smaller than the mass term near the origin and larger at some point as shown in Eq. (2.2.10).

in Fig. 2.2.1. First, to reach the origin with the initial zero velocity $\partial\Phi/\partial r|_{r\to 0} = 0$, the initial potential energy of the particle must be larger than zero, which requires the condition $U(\Phi) > \omega^2\Phi^2/2$ at some point. Then, to reach the origin at $r \to \infty$, the kinetic energy of the particle must be compensated by the potential energy near the origin, which requires the negative mass near the origin as $\omega < m$. From these two requirements, we can fined that the condition Eq. (2.2.10) is necessary for the existence of the solution.

Note that this condition is only necessary and not sufficient. This is because large fluctuations of the field $\delta\phi/\phi \sim \mathcal{O}(1)$ is also needed for oscillon formation. To calculate the evolution of the field value, we have to perform numerical simulation and we will do so later in Part II.

Stability condition When the scalar field follows the oscillon profile $\phi = \phi_{\rm osc}$, the adiabatic charge Eq. (2.1.20) is the same as the total number inside the oscillon as

$$I = \frac{1}{\omega}\int \dot{\phi}_{\rm osc}^2 d^3x = \frac{\omega}{2}\int 4\pi r^2 \Phi(r)^2 dr. \tag{2.2.13}$$

Related to the conservation of this total number, it is shown that oscillons are stable only when

$$\frac{dI}{d\omega} < 0, \tag{2.2.14}$$

which is the well-known Vakhitov and Kolokolov stability condition [61]. This condition can be intuitively understood by considering the limit $\omega \to m$. In this limit, because of the inequality Eq. (2.2.10), the oscillon solution must not exist and the adiabatic

15

invariant must converge to 0. In addition, the oscillon solution must be unique for a given I because it is the lowest energy state under a fixed I. To satisfy these two statements, $dI/d\omega$ must be negative, which indicates the stability condition of oscillons. Please see Refs. [61, 62, 63]) for the detailed derivation.

2.3 Decay Rate

As we have seen in the previous section, because the oscillon configuration is given as the minimum energy state with a given adiabatic charge, oscillons are generally quasi-stable. However, this adiabatic invariance is violated by the self-interactions and they gradually decay with the emission of self-radiation. Although various methods have already been suggested to investigate the decay rate of oscillons [64, 65], in this thesis we follow Refs. [38, 39] and review the calculation of the classical decay rate of oscillons

$$\Gamma \equiv \frac{1}{E} \left| \frac{\overline{dE}}{dt} \right|, \qquad (2.3.1)$$

where E is the total energy of an oscillon. We further assume $V_{\mathrm{nl}}(\phi) = V_{\mathrm{nl}}(-\phi)$ in this section unless otherwise stated.

Suppose that the scalar field is decomposed into the oscillon and its scalar radiation ξ as

$$\phi(t, \boldsymbol{x}) = \Phi(r) \cos \omega t + \xi(t, r), \qquad (2.3.2)$$

where $\Phi(r)$ obeys the oscillon profile equation Eq. (2.2.4) and we only consider the radial mode of ξ with $|\xi| \ll \Phi$ here. Substituting this expansion into the equation of motion of ϕ

$$\left(\partial_\mu \partial^\mu + m^2 \right) \phi(t, \boldsymbol{x}) = -\frac{\partial V_{\mathrm{nl}}(\phi)}{\partial \phi}, \qquad (2.3.3)$$

and using the profile equation Eq. (2.2.4), we can derive the equation of motion of ξ as

$$\left(\partial_\mu \partial^\mu + m^2 \right) \xi(t, r) = - \left(\partial_\mu \partial^\mu + m^2 \right) \Phi \cos \omega t - \frac{\partial V_{\mathrm{nl}}(\phi)}{\partial \phi}, \qquad (2.3.4)$$

$$= 2 \frac{dU_{\mathrm{nl}}(\Phi)}{d\Phi} \cos \omega t - \frac{\partial V_{\mathrm{nl}}(\phi)}{\partial \phi}. \qquad (2.3.5)$$

To solve this equation, let us expand $V_{\mathrm{nl}}(\phi)$ around the oscillon profile as

$$V_{\mathrm{nl}}(\phi) = V_{\mathrm{nl}} \left(\Phi \cos \omega t \right) + V'_{\mathrm{nl}} \left(\Phi \cos \omega t \right) \xi + \mathcal{O} \left(\xi^2 \right), \qquad (2.3.6)$$

where the dash represents the derivative with respect to ϕ. Then, the equation of ξ is rewritten as

$$\left[\partial_\mu \partial^\mu + m^2 + V''_{\mathrm{nl}} \left(\Phi \cos \omega t \right) \right] \xi(t, r) = 2 \frac{dU_{\mathrm{nl}} \left(\Phi \right)}{d\Phi} \cos \omega t - V'_{\mathrm{nl}} \left(\Phi \cos \omega t \right), \qquad (2.3.7)$$

up to the first order of ξ. We can calculate the oscillon decay rate by solving this equation.

Because the frequency of the oscillation inside an oscillon is described by a single mode and we assume $V_{\rm nl}(\phi) = V_{\rm nl}(-\phi)$, we can expand $V_{\rm nl}$ in a Fourier series in time as

$$V_{\rm nl}\left(\Phi\cos\omega t\right) = -\frac{1}{2}\mathcal{U}_0\left(\Phi\right) - \sum_{j=2}^{\infty}\mathcal{U}_j\left(\Phi\right)\cos(j\omega t)\big|_{j={\rm even}}, \qquad (2.3.8)$$

$$V_{\rm nl}'\left(\Phi\cos\omega t\right) = -\sum_{j=1}^{\infty}\mathcal{S}_j\left(\Phi\right)\cos(j\omega t)\big|_{j={\rm odd}}, \qquad (2.3.9)$$

$$V_{\rm nl}''\left(\Phi\cos\omega t\right) = \frac{1}{2}\mathcal{E}_0\left(\Phi\right) + \sum_{j=2}^{\infty}\mathcal{E}_j\left(\Phi\right)\cos(j\omega t)\big|_{j={\rm even}}, \qquad (2.3.10)$$

where

$$\mathcal{U}_j(\Phi) = -\frac{\omega}{\pi}\int_{-\pi/\omega}^{\pi/\omega} dt'\,\cos(j\omega t')V_{\rm nl}\left(\Phi\cos\omega t'\right), \qquad (2.3.11)$$

$$\mathcal{S}_j(\Phi) = -\frac{\omega}{\pi}\int_{-\pi/\omega}^{\pi/\omega} dt'\,\cos(j\omega t')V_{\rm nl}'\left(\Phi\cos\omega t'\right), \qquad (2.3.12)$$

$$\mathcal{E}_j(\Phi) = -\frac{\omega}{\pi}\int_{-\pi/\omega}^{\pi/\omega} dt'\,\cos(j\omega t')V_{\rm nl}''\left(\Phi\cos\omega t'\right). \qquad (2.3.13)$$

Then, from the definition of $U_{\rm nl}$ and $U_{\rm nl}'$,

$$U_{\rm nl}\left(\Phi\right) = \overline{V_{\rm nl}\left(\Phi\cos\omega t\right)} = -\frac{1}{2}\mathcal{U}_0\left(\Phi\right), \qquad (2.3.14)$$

$$U_{\rm nl}'\left(\Phi\right) = \overline{V_{\rm nl}'\left(\Phi\cos\omega t\right)} = -\frac{1}{2}\mathcal{S}_1\left(\Phi\right). \qquad (2.3.15)$$

Besides, expanding ξ in a Fourier series as

$$\xi(t,r) = \sum_{j=3}^{\infty}\xi_j(r)\cos(j\omega t), \qquad (2.3.16)$$

the equation of motion of ξ Eq. (2.3.7) is calculated as

$$\left[\partial_\mu\partial^\mu + m^2 + V_{\rm nl}''\left(\Phi\cos\omega t\right)\right]\xi(t,r) = \sum_{j=3}^{\infty}\mathcal{S}_j\left(\Phi\right)\cos(j\omega t)\big|_{j={\rm odd}}. \qquad (2.3.17)$$

$$\therefore \quad \left(\nabla^2 + \kappa_j^2\right)\xi_j(r) = -\mathcal{S}_j\left(\Phi\right) + \frac{1}{2}\sum_{l=3}^{\infty}\left(\mathcal{E}_{j+l} + \mathcal{E}_{|j-l|}\right)\xi_l(r) \equiv -S_j, \qquad (2.3.18)$$

17

where we have defined the effective mass term as $\kappa_j \equiv \sqrt{(j\omega)^2 - m^2}$.

Considering that the right hand side of this equation equals to $-\mathcal{S}_j(\Phi)$ when we ignore the effective mass term κ_j^2, we can derive a solution using the Green's function method as [39]

$$\xi_j(r) = \frac{\cos(\kappa_j r)}{\kappa_j r} \int_0^r dr' S_j(r') r' \sin(\kappa_j r') + \frac{\sin}{r} \int_r^\infty dr' S_j(r') r' \cos(\kappa_j r'), \quad (2.3.19)$$

without the homogeneous solutions. In the limit where r is much larger than the size of the oscillon, the solution ξ_j is approximated as

$$\xi_j(r) \approx \frac{\cos(\kappa_j r)}{\kappa_j r} \int_0^r dr' S_j r' \sin(\kappa_j r') = \frac{1}{4\pi} \frac{\tilde{S}_j(\kappa_j) \cos \kappa_j r}{r}, \quad (2.3.20)$$

where we have used the relation that the integration simply shows the Fourier transformation of $S_j(r)$ evaluated at $k = \kappa_j$ as

$$\tilde{S}_j(k) = \int d^3 r' S_j(r') e^{-i\boldsymbol{k}\cdot\boldsymbol{r}'}. \quad (2.3.21)$$

Then, substituting this solution to Eq. (2.3.16) and ignoring the incoming wave part, we obtain the time variation of the oscillon energy E as

$$\xi^{\mathrm{rad}}(t, r) \approx \frac{1}{4\pi r} \sum_{j=3} \tilde{S}_j(\kappa_j) \cos(\kappa_j r - j\omega t). \quad (2.3.22)$$

$$\therefore \quad \Gamma(E) \equiv \frac{1}{E} \overline{\frac{dE}{dt}}, \quad (2.3.23)$$

$$= 4\pi r^2 \overline{\partial_t \xi^{\mathrm{rad}} \partial_r \xi^{\mathrm{rad}}} \equiv \sum_{j=3} \Gamma_j, \quad (2.3.24)$$

where

$$\Gamma_j \equiv -\frac{1}{8\pi E} \omega_j \kappa_j \tilde{\mathcal{S}}_j(\kappa_j)^2. \quad (2.3.25)$$

This energy variation is exponentially suppressed because $\tilde{S}_j(\kappa_j)$ is constructed from the spatially localized profile $\Phi(r)$. Given that the width of the oscillon profile is generally $w \gtrsim \mathcal{O}(1) m^{-1}$, the wavenumber $\kappa_j \gtrsim m$ is larger than w^{-1}. Thus, the exponential suppression factor due to the Fourier transformation makes oscillons quasi-stable objects.

Furthermore, $\tilde{S}_j(\kappa_j) \gg \tilde{S}_{j+1}(\kappa_{j+1})$ is generally expected because the larger j corresponds to the higher order of momentum. However, this relation does not hold only if $\tilde{S}_j(\kappa_j)$ is accidentally vanished. We will see a specific example in Part II.

Chapter 3

Ultra-Light Axion-like Particle

In this chapter, we introduce ultra-light axion-like particle (ULAP). First, we briefly explain the original axion, quantum chromodynamics (QCD) axion [20, 21, 22, 23, 24], which is introduced to solve strong CP problem [66, 67]. Next, we briefly explain the theoretical motivation of axion-like particles (ALPs) and show that ultra-light ones are fascinated as a solution to the small scale problems of astrophysics. Finally, we summarize current constraints on the ULAP mass from recent works.

3.1 QCD Axion

In standard model, QCD Lagrangian generally contains a charge-parity (CP) violating term originated from quantum anomaly as

$$\mathcal{L}_\theta = \frac{g^2 N_f}{32\pi^2} \theta G_{\mu\nu}^a \tilde{G}^{a\mu\nu}, \tag{3.1.1}$$

where g is the coupling constant in QCD, N_f is the number of fermions coupling to the QCD gauge fields, $G_{\mu\nu}^a$ is the field strength of gluons, and $\tilde{G}_{\mu\nu}^a = \epsilon^{\mu\nu\rho\sigma} G_{\rho\sigma}/2$. This term is often called θ term and it is natural to assume $\theta \sim \mathcal{O}(1)$. However, from experiments of neutron electric dipole moment [68, 69], θ is revealed to be extremely small that

$$\theta \lesssim 10^{-10}. \tag{3.1.2}$$

Therefore, the CP symmetry in the QCD sector is hardly broken. This discrepancy between the theory and experiments is called strong CP problem.

The most famous solution to strong CP problem is Peccei-Quinn (PQ) mechanism [66, 67]. In this mechanism, we impose an additional global $U(1)$ chiral symmetry, which makes all fermions coupling to QCD gauge fields symmetric in the chiral rotation

$$q_i \rightarrow e^{i\gamma_5\alpha_i} q_i. \tag{3.1.3}$$

Because the quantum anomaly Eq. (3.1.1) cannot retain physical meaning due to this symmetry, the strong CP problem is solved. This symmetry is often called Peccei-Quinn symmetry $U(1)_{\mathrm{PQ}}$.

Because particles that relates to the PQ mechanism are still not observed, $U(1)_{\mathrm{PQ}}$ symmetry must be spontaneously broken at least on a scale much higher than the electroweak scale. When the PQ symmetry is spontaneously broken at some scale v, the PQ field, which has a PQ charge α, is written as

$$\Phi_{\mathrm{PQ}} = \frac{1}{\sqrt{2}} v e^{i\alpha a/v}. \tag{3.1.4}$$

where the phase field a is the Nambu-Goldstone boson called QCD axion. As a result, the θ term is deformed to

$$\mathcal{L}_\theta = \frac{g^2 N_f}{32\pi^2} \left(\theta - \frac{a}{v} \right) G_{\mu\nu}^a \tilde{G}^{a\mu\nu}. \tag{3.1.5}$$

Because the QCD axion has shift symmetry due to the $U(1)_{\mathrm{PQ}}$ symmetry, this term can be safely removed from the Lagrangian [70]

After the QCD phase transition, the QCD axion acquires potential by a non-perturbative effect. With the dilute gas approximation [71] it is derived as

$$V(a) = m^2 F^2 \left(1 - \cos \frac{a}{F} \right), \tag{3.1.6}$$

where $m \propto F^{-1}$ is the QCD axion mass and $F = v/N_f$ is the decay constant of the QCD axion.

The lower bound on F is obtained by the observation of the supernova SN1987A [72, 73, 74] as $F \gtrsim 10^8$ GeV, which corresponds with $m \simeq 10^{-2}$ eV. On the other hand, the upper bound on the decay constant depends on the scale of inflation of the early universe. When inflation occurs before PQ symmetry breaking, because the field value of the QCD axion is uniform due to the exponential expansion of space by inflation, we can take an arbitrary scale of F if we tune the initial amplitude of the QCD axion. However, If the inflation scale is higher than the PQ symmetry scale, we have to take into account two cosmological constraints. The first is the domain wall problem [75]. Because the potential Eq. (3.1.6) has $Z(N_f)$ symmetry, domain walls are produced after the QCD axion acquires mass. In this case, because the energy density of domain walls follows $\rho_{\mathrm{DW}} \propto t^{-1}$, $N_f = 1$ must be satisfied not to overclose the universe. The second is the overclosure of the universe by the coherent oscillations of the axion. Because the variance over the entire universe of the initial amplitude of the QCD axion is randomized as $\langle (a/F)^2 \rangle = \pi^2/3$, the decay constant is constrained to avoid the overclosure of the universe as $F \lesssim 10^{12}$ GeV according to previous researches [76, 77, 78]. [1] This constraint corresponds to $m \sim 10^{-6}$ eV. Thus, the typical scale of the QCD axion is

$$10^8 \text{ GeV} \lesssim F \lesssim 10^{12} \text{ GeV} \quad \Leftrightarrow \quad 10^{-6} \text{ eV} \lesssim m \lesssim 10^{-2} \text{ eV}.$$

3.2 Axion-like Particle

In this section, first, we briefly introduce axion-like particle (ALP) in the theoretical point of view. Next, we focus on the phenomenological aspects of ALP, which is highly motivated in terms of astrophysical problems on small scales if it is ultra-light.

---

[1]This constraint is much stronger if we further consider the radiative axion emitted from the string-wall system [79].

3.2.1 Theoretical Motivation

In string theory, plenty of massless scalar fields is predicted when the ten-dimensional spacetime is compactified into observable four dimensions. Here, we first give a simple example that a massless scalar field is created by spacetime compactification. Please see Refs. [11, 16] for more reviews.

Let us consider four-dimensional Minkowski spacetime plus extra fifth dimensional space which is compactified into a circle. When the theory includes a massless scalar field ψ in these five dimensions, we can expand it in Fourier series as

$$\psi\left(x^{\sigma}\right) = \sum_{n} \phi_n\left(x^{\mu}\right) e^{inx^4/R}, \tag{3.2.1}$$

where $\sigma = 0, \cdots 4$ denotes the spacetime index in five dimensions and R is the radius of the compact dimension. Then, the total action in five dimensions is reduced to

$$\int d^5x \partial_{\sigma}\psi \partial^{\sigma}\psi = \int d^4x \int_0^{2\pi R} dx^4 \left(\partial_{\mu}\psi \partial^{\mu}\psi + \partial_4\psi \partial^4\psi\right), \tag{3.2.2}$$

$$= \int d^4x \sum_n \left(\partial_{\mu}\phi_n^{\dagger}\partial^{\mu}\phi_n + \frac{n^2}{R^2}\phi_n^{\dagger}\phi_n\right), \tag{3.2.3}$$

in four dimensions. Therefore, we can find that the compactification gives us a massless scalar mode ($n = 0$) and massive ones separated by $1/R$ in mass. This result is fairy intuitive because to create a massless mode in four dimensions from a massless scalar field with $\Delta_5\psi = \left(\partial_{\mu}\partial^{\mu} + \partial_4\partial^4\right)\psi = 0$, $\partial_4\partial^4\psi = 0$ should be satisfied for the massless mode. This condition only holds for $n = 0$, which corresponds to the massless mode.

In higher dimensional space like string theory, much more massless fields are generally expected. We do not mention the details here because it is beyond our scope, but those fields created from the dimensional reduction of massless fields in the ten-dimensional string spectrum are called axion-like particles.

Those particles are originally generated as massless, but the shift symmetry which supports its massless could be non-perturbatively violated. Suppose an ALP field as θ periodic in $0 - 2\pi$, the effective Lagrangian is parameterized as

$$\mathcal{L} = \frac{F^2}{2}\left(\partial_{\mu}\theta\right)^2 - \Lambda^4 U(\theta), \tag{3.2.4}$$

where F is a ULAP parameter, often called the decay constant in analogy with the QCD axion. Because the shift symmetry is violated non-perturbatively in this case, Λ is represented as

$$\Lambda^4 = \mu^4 e^{-S}, \tag{3.2.5}$$

where $S \sim 2\pi/\alpha_G \sim \mathcal{O}(100)$ is the instanton action with α_G being the Standard Model gauge coupling on the grand unified energy scale $M_G \sim 1.1 \times 10^{16}$ GeV. If ALP arises from the superpotential of string instantons, the scale μ is determined by the Planck scale (the scale of string theory) and supersymmetry (SUSY) breaking scale F_{SUSY} as

$$\mu^4 \sim F_{\text{SUSY}} M_{\text{Pl}}^2. \tag{3.2.6}$$

21

Therefore, ALP mass m is represented by

$$m = \frac{\Lambda^2}{F} \sim \frac{F_{\text{SUSY}}^{1/2} M_{\text{Pl}}}{F} e^{-S/2}.$$ (3.2.7)

The range of F_{SUSY} is roughly 10^4 GeV $\lesssim F_{\text{SUSY}}^{1/2} \lesssim 10^{18}$ GeV and that of the decay constant is

$$10^{16} \text{ GeV} \lesssim F \lesssim 10^{18} \text{ GeV}.$$ (3.2.8)

Substituting these values into Eq. (3.2.7), we can find that string theory allows a vast range of ALP mass mainly due to the suppression of supersymmetry. In the next subsection, we focus on ultra-light ALPs, $m \sim 10^{-22} - 10^{-21}$ eV, and see why ULAP is fascinating in the point of astrophysics.

3.2.2 Phenomenological Motivation

ALPs with extremely light mass, known as ultra-light axion-like particle (ULAP), are motivated as the solution to astrophysical problems. Here, we briefly explain these astrophysical problems and show why ULAP can solve these problems. See also Ref. [80] for a review of astrophysical problems on small scales.

Regardless of the success of ΛCDM model on large scales, it contains three astrophysical problems on small scales $\lesssim \mathcal{O}(10)$ kpc.

1. Missing satellite problem

   The first is the missing satellite problem. In the simulations of Milky Way sized dark matter halos based on the ΛCDM paradigm, the number of subhalos greatly exceeds the observed values [7, 81]. While we can expect the existence of thousands of subhalos by recent high resolution simulations [82, 83, 84, 85, 86], only ~ 50 dwarf satellites are found to orbit within Milky Way [87]. Even though recent observations have discovered about $\mathcal{O}(10)$ more satellites (e.g., [88, 89]), there still remains a large discrepancy between the simulations and the observations.

2. Core-cusp problem

   The second is the core-cusp problem. While N-body simulations of ΛCDM model which only includes dark matter predict that the density profiles around the center of dark matter halos are steep as $\rho(r) \propto r^{-\alpha}$ with $\alpha \sim 0.8 - 1.4$ (e.g., [90, 91, 92]), many observations of low mass galaxies suggest $\alpha \sim 0 - 0.5$ (e.g., [93, 94, 95]). In Fig. 3.2.1, we show the rotation curve of dark matter halos with a maximum velocity $V_{\text{max}} \simeq 40$ km/s. From this figure, the theoretical prediction rises more rapidly than the observational values well fitted by the cyan line because of the central over-density. This tension between the cusp profiles in simulations and core profiles in observations is called core-cusp problem.

3. Too-big-to-fail problem

   The third is the too-big-to-fail problem. Because the largest satellites predicted from the simulations are massive enough to produce bright galaxies inside them,
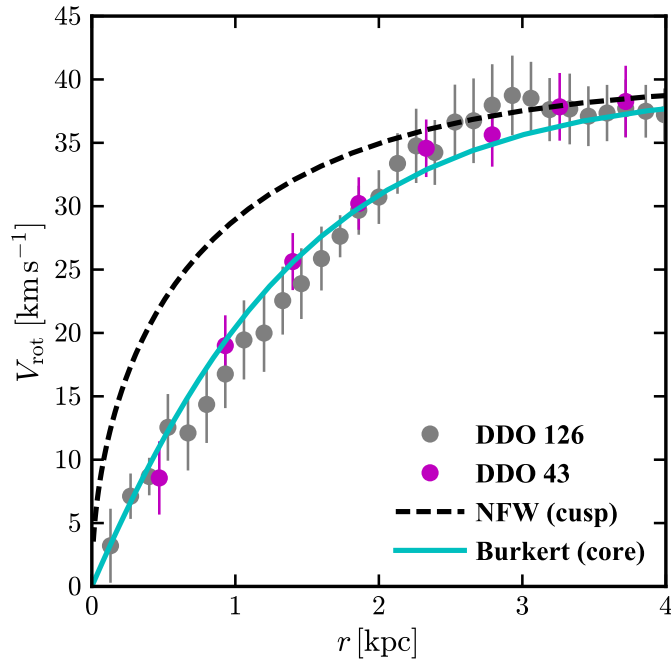
Figure 3.2.1: The figure of core-cusp problem taken from Ref. [80]. The horizontal axis shows the distance from the galactic center and the vertical axis shows the rotation velocity. The dashed line shows the theoretical prediction derived from dark matter only simulations (NFW profile) while the cyan one does the density profiles with a constant core. The data points shown by gray and magenta dots [99] are better fit by the cyan line [100].

> we can test the consistency of properties of the observed satellites to numerical simulations. In Milky Way, for example, it is revealed that the predicted central density of the most massive subhalos is much more concentrated than the known satellites [96, 9]. However, even if such massive subhalos indeed reside in Milky Way, why do galaxies fail to form in such massive subhalos, yet form in satellites with lower mass? That is why this problem is called too-big-to-fail problem. Similar results are subsequently obtained in Andromeda [97] and the Local Group [98].

All these problems are caused by the over-densities on small scales. Thus, a mechanism to suppress the small scale structure of the universe is necessary to solve them.

Within ΛCDM paradigm, one of the most common solutions is baryonic physics. Because of the stellar feedback from supernova explosions, the central cusps of dark matter halos could be wiped out [101, 102]. Recent high-resolution hydrodynamical simulations suggest that supernova-driven blowouts produce core-like density profile depending on the halo mass [103, 104] as shown in Fig. 3.2.2. For the smaller galaxies subject to too-big-to-fail problem which cannot be solved by the supernova feedback, other interactions of baryons such as tidal stripping and disk shocking can reduce the central overdensity and would solve the too-big-to-fail problem [105, 106, 107, 108]. However, it is important to note that the simulation results fairly depends on various parameters in galaxy formation modeling. Depending on their modeling, some papers do not exhibit cores [108],
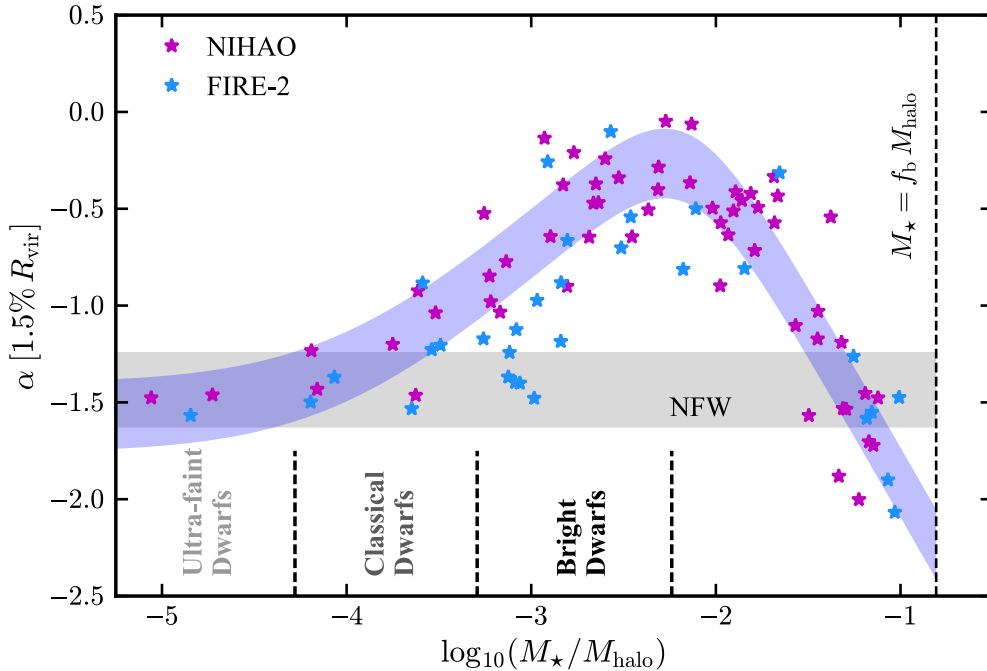
Figure 3.2.2: The figure of baryonic feedback to density profiles of dark matter halos taken from Ref. [80]. The horizontal axis shows the stellar mass M_* normalized by the host halo mass M_{halo} and the vertical axis shows α with $\rho \propto r^\alpha$ at $r = 0.015 r_{vir}$. The gray shaded region shows the theoretical prediction of the NFW profile. The magenta stars show the result of NIHAO hydrodynamical simulations [110] guided by the purple shaded region and cyan ones do the similar results from FIRE-2 simulations [111, 112].

while others obtain cores in galaxies with all stellar masses [109].

Another approach to solve the small scale problems is to slightly modify the property of cold dark matter. One of the prominent candidates is ULAP [12, 113, 114, 115], which is a scalar particle with an extremely small mass as $10^{-22}-10^{-21}$ eV. In this case, because the de Broglie length of ULAP is estimated as

$$\frac{\lambda}{2\pi} = \frac{1}{mv} = 1.92 \text{ kpc} \left(\frac{10^{-22} \text{ eV}}{m}\right)\left(\frac{10 \text{ km/s}}{v}\right), \qquad (3.2.9)$$

where v is the velocity of ULAP, the quantum pressure is expected to smear out the the small scale structure below the ULAP Jeans scale.

Indeed, it is suggested that the three astrophysical problems are solved in this model. As for the core-cusp problem, N-body and hydrodynamical simulations show that ULAP produces a core profile near the halo center [14, 13, 15] because the soliton-like objects are created by the balance between the quantum pressure and gravitational forces. This solitonic object is often called "dilute axion star" in contrast to "dense axion star" which refers to oscillons [116, 117]. This is because the self-interactions which support oscillons are generally much stronger than the gravitational forces due to the Planck scale suppression, which leads to the smaller radius and higher density of oscillons. Thus, these two kinds of objects are similar but distinct. The comparison between simulation results

24

and observations of dwarf spheroidal galaxies suggests that the best-fit ULAP mass is about 10^{-22} eV.

The other problems are also expected to be solved mainly because the structures below the Jeans scale of ULAP is suppressed by the wave property of scalar fields. This leads to the suppression of the matter power spectrum and a smaller number of halos. For the missing satellite problem, the further reason is that subhalos are more susceptible to tidal disruption. Because of the wave property, matter even within the tidal radius can tunnel through the potential barrier and be disrupted. Therefore, small subhalos cannot stably exist in ULAP halos. For the too-big-to-fail problem, another reason is that the subhalo masses are observationally estimated by the maximum circular velocity of baryons, which is generally smaller in ULAP than CDM [118]. This could result in the estimation of the smaller subhalo masses.

As such, ULAP is considered to be a strong candidate for dark matter and hence various constraints are suggested. In the next section, we will show major constraints on the ULAP mass and abundance.

3.3 Constraints

In this section, we exhibit constraints on ULAP mass. Here, we do not include the axion photon coupling

$$ -\frac{g_{a\gamma}}{4} a F_{\mu\nu} \tilde{F}^{\mu\nu}, \tag{3.3.1} $$

which is generated when PQ fields have an interaction with Electromagnetic field $F_{\mu\nu}$ because this coupling is not assumed in this thesis. Besides, although various fitting results based on the observed dark matter profiles are suggested, we focus only on the cosmological constraints mainly because of the astrophysical uncertainties. Please see, for example, Refs. [119, 120, 121, 122] for the fitting results.

CMB

Because ULAP behaves like dark energy before it starts to oscillate at $H \simeq m$, the proportions of the components are changed before and after the oscillation, which significantly affects the CMB spectrum. When the onset of the oscillation is before the radiation-matter equality $H_{\mathrm{eq}} \simeq 10^{-28}$ eV, the hight of the CMB acoustic peaks on small scales are amplified due to the decrease of the dark matter component. On the other hand, when the onset of the oscillation is after the radiation-matter equality, mainly the positions of the acoustic peaks are affected because the change of the abundance of dark energy alters the cosmic expansion rate. In Ref. [123], it is shown that the ULAP abundance Ω_ϕ must obey $\Omega_\phi/\Omega_{\mathrm{DM}} \leq 0.05$ at 95% confidence level with Ω_{DM} being the relic abundance of dark matter when the ULAP mass is in the range of

$$ 10^{-32} \text{ eV} \leq m \leq 10^{-25.5} \text{ eV}. \tag{3.3.2} $$

Because the ULAP mass is too small to oscillate enough even in the current universe for $m \lesssim 10^{-32}$ eV, we cannot constrain the smaller mass region, which suggests the possibility of ULAP dark energy. Please see Fig. 3.3.1 for the details of the constraint.
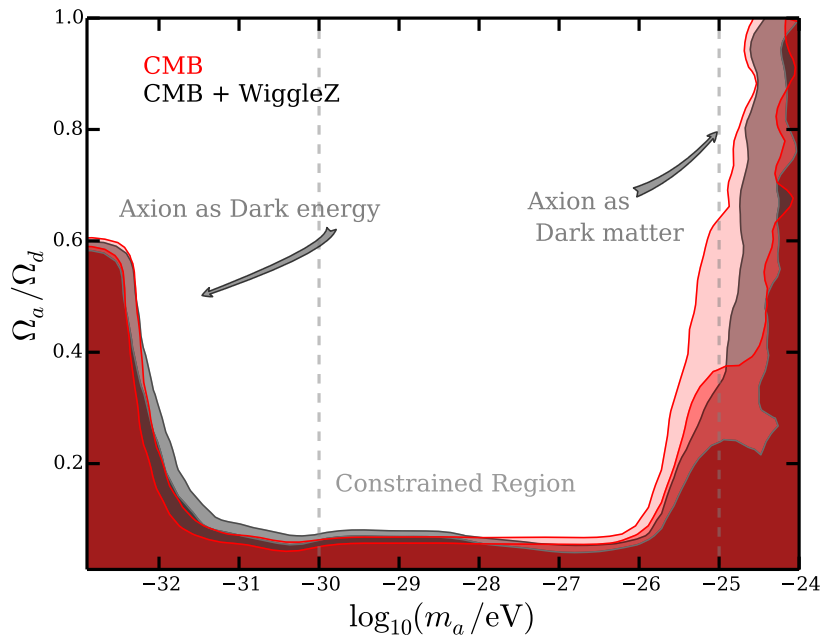
Figure 3.3.1: The constraint on the ULAP mass m_a taken from Ref. [123]. The colored regions show the marginalized 2σ and 3σ contours limiting the ratio of ULAP to the total dark matter energy density Ω_a/Ω_d as a function of m_a. The red regions are favored by CMB-only constraints, while grey regions also take the large-scale structure data into account.
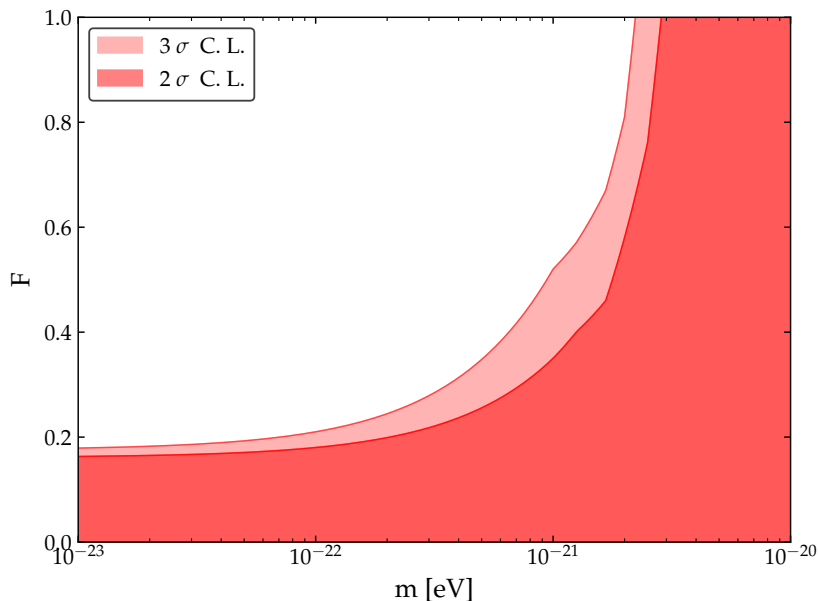
Figure 3.3.2: The constraint on the ULAP mass m and the fraction of ULAP $F = \Omega_\phi/\Omega_{DM}$ by Lyman-α forest taken from Ref. [125]. The colored regions indicating 2σ and 3σ confidence levels are favored with a physically motivated prior on the thermal evolution of the intergalactic medium. Note that the region of $m < 10^{-22}$ eV is simply extrapolated.

Lyman-α forest

Because ULAP suppresses the gravitational growth below its Jeans scale, the suppression of the matter power spectrum affects the signals of the Lyman-α forest which is a useful tracer for the small scale structure around $\sim \mathcal{O}(1)$ Mpc. Recent results of hydrodynamical and N-body simulations [124, 125] suggest that when the ULAP abundance Ω_ϕ obeys $\Omega_\phi/\Omega_{DM} \geq 0.3$, the ULAP mass should satisfy

$$m \gtrsim 10^{-21} \text{ eV.} \tag{3.3.3}$$

This constraint is the most stringent among all that does not take account of the photon-axion interaction, but note that this constraint highly depends on baryonic modeling. The details of the constraint is shown in Fig. 3.3.2.

UV-luminosity function

Similarly to the constraint of the Lyman-α forest, the constraint from the UV-luminosity function also uses the suppression of the small scale structure by ULAP. Because of this suppression, the number of high-z galaxies is also suppressed and the UV-luminosity function, which provides the number density of star-forming galaxies per absolute magnitude, is altered. In Ref. [126], the study of UV-luminosity function in the range $z = 6 - 10$ concludes that the ULAP mass must be

$$m \gtrsim 10^{-23} \text{ eV,} \tag{3.3.4}$$

27

when $\Omega_\phi/\Omega_{\mathrm{DM}} \geq 0.5$ at more than 8σ significance.

Dynamical Heating of the Milky Way

Starts in globular clusters or dwarf galaxies are torn apart by dynamical evolutionary processes of the stellar system and orbiting as a stellar stream at present. When these streams pass by massive objects, the velocity dispersion of the streams increases by the gravitational interaction. In contrast to the case of CDM that the number of halos gets smaller with decreasing galactic radius, perturbations become more effective because of the wave property of ULAP. Ref. [127] focuses on globular clusters in the Milky Way and points out that ULAP mass must satisfy

$$m > 1.5 \times 10^{-22} \text{ eV}, \tag{3.3.5}$$

when the profile of the Milky Way is described by the ULAP core.

Superradiance

If massive scalar fields exist in the theory, they can be exponentially produced by the superradiance instability around spinning black holes (called Kerr black holes) with mass $\sim (Gm)^{-1}$. Then, they form bound states around them and extract energy and angular momentum from the Kerr black holes by Penrose process [128] as they infall. Therefore, the spinning black holes should not be observed if ULAP with a corresponding mass exists in the theory. In Refs. [129, 130, 131],

$$6 \times 10^{-13} \text{ eV} < m < 2 \times 10^{-11} \text{ eV}, \tag{3.3.6}$$

with $F \gtrsim 10^{13}$ GeV is excluded by solar mass black holes and roughly $10^{-17} - 10^{-16}$ eV with $F \gtrsim 10^{16}$ GeV is also excluded by supermassive black holes. As we mentioned, this constraint does not depend on whether ULAP exists as dark matter or not and is quite generic in the theory with ultra-light scalar fields. See Refs. [129, 132] for more details.

Chapter 4

21cm Line

Thanks to the greatest efforts of observations, the cosmological structure up to the scale $\gtrsim \mathcal{O}(1)$ Mpc has already been probed. The small scale is mainly explored by the Lyman-α forest, which is produced by consecutive absorption due to the transition of an electron in a neutral hydrogen atom between the ground state ($n = 1$) and the first excited state ($n = 2$). Recently further efforts to probe smaller scale structure are made and one of the methods is 21cm absorption line, which is produced by the hyperfine splitting due to the interaction between the electron and proton spins in a neutral hydrogen atom [48]. Because neutral hydrogen is ubiquitous in the early universe before reionization $z \sim 6$, the 21cm line is generally adopted as the useful tracer of the universe before reionization $z \lesssim 6$.

In this chapter, we will review some of the basic formulae of 21cm line to be used in Chap. 6 in Part II. First, we derive general formulae in a two-level system: the radiative transfer equation and the optical depth from a specific intensity. Second, we explain the basics of 21cm line and then discuss the 21cm forest at last.

Here, we only consider a two-level system and denote the lower index $0, 1$ to represent the value of the ground and excited state, respectively. Note that the system of units is CGS unit in this chapter following the convention in astronomy. Thus, h, c, k_B represents Planck constant, speed of light, and Boltzmann constant, respectively.

4.1 Radiative Transfer Equation

To understand the basics of 21cm line, let us calculate the evolution of a specific intensity I_ν, which represents the radiative flux per frequency per unit solid angle. The radiative transfer equation for I_ν is

$$\frac{1}{c}\frac{dI_\nu(\boldsymbol{x}, t; \boldsymbol{n})}{dt} = -\alpha_\nu(\boldsymbol{x}, t; \boldsymbol{n})I_\nu(\boldsymbol{x}, t; \boldsymbol{n}) + \eta_\nu(\boldsymbol{x}, t; \boldsymbol{n}), \tag{4.1.1}$$

where α_ν is the specific extinction which represents the absorption of the system, and η_ν is the specific emissivity which represents the radiation from the system. Defining the optical depth as

$$\tau_\nu(s) \equiv \int^s \alpha_\nu\left(\boldsymbol{x}(t), t; \boldsymbol{n}(t)\right) d(ct), \tag{4.1.2}$$

29

where the integration is taken over the path of the incoming flux, we can simplify the radiative transfer equation Eq. (4.1.1) as

$$\frac{dI_\nu(\boldsymbol{x},t;\boldsymbol{n})}{d\tau_\nu} = -I_\nu(\boldsymbol{x},t;\boldsymbol{n}) + \frac{\eta_\nu(\boldsymbol{x},t;\boldsymbol{n})}{\alpha_\nu(\boldsymbol{x},t;\boldsymbol{n})}. \tag{4.1.3}$$

To solve this equation, we have to consider the three processes: the absorption, spontaneous emission, and stimulated emission. Because the relation between the energy density and the specific intensity is given by

$$I_\nu = \frac{c}{4\pi}\rho(\nu), \tag{4.1.4}$$

the effect on the specific intensity in a two-level system is derived as

$$dI_\nu = - dI_\nu|_{\text{Abs}} + dI_\nu|_{\text{Sti}} + dI_\nu|_{\text{Em}}, \tag{4.1.5}$$

$$= h\nu_{10}\left[-B_{01}\left(\nu_{10}\right)\frac{\rho\left(\nu_{10}\right)}{4\pi}n_0\phi_a(\nu) + B_{10}\left(\nu_{10}\right)\frac{\rho\left(\nu_{10}\right)}{4\pi}n_1\phi_e(\nu) + A_{10}n_1\phi_e(\nu)\right]d(ct),$$

$$= h\nu_{10}\left[-\frac{1}{c}\left(B_{01}\left(\nu_{10}\right)n_0\phi_a(\nu) - B_{10}\left(\nu_{10}\right)n_1\phi_e(\nu)\right)I_\nu + +A_{10}n_1\phi_e(\nu)\right]d(ct). \tag{4.1.6}$$

where ν_{10} is the frequency difference between the two states and $\phi_a(\nu), \phi_e(\nu)$ are the line profile of the incoming and emitted flux, respectively. Then, assuming that the profile functions satisfy $\phi(\nu) = \phi_a(\nu) = \phi_e(\nu)$ for simplicity, we have

$$\alpha_\nu(\boldsymbol{x},t;\boldsymbol{n}) = \frac{h\nu_{10}}{c}\left[B_{01}\left(\nu_{10}\right)n_0(\boldsymbol{x},t) - B_{10}\left(\nu_{10}\right)n_1(\boldsymbol{x},t)\right]\phi(\nu), \tag{4.1.7}$$

$$= \frac{h\nu_{10}}{c}B_{01}n_0\left[1 - \frac{B_{10}(\nu)n_1(\boldsymbol{x},t)}{B_{01}(\nu)n_0(\boldsymbol{x},t)}\right]\phi(\nu), \tag{4.1.8}$$

$$= \frac{h\nu_{10}}{c}n_0(\boldsymbol{x},t)A_{10}\frac{c^3}{8\pi h\nu_{10}^3}\frac{g_1}{g_0}\left[1 - \frac{g_0}{g_1}\frac{g_1}{g_0}\exp\left(-\frac{h\nu_{10}}{k_BT_s(\boldsymbol{x},t)}\right)\right]\phi(\nu), \tag{4.1.9}$$

$$\simeq \frac{g_1}{g_0}\frac{hc^2A_{10}}{8\pi k_B\nu_{10}}\frac{n_0(\boldsymbol{x},t)}{T_s(\boldsymbol{x},t)}\phi(\nu). \tag{4.1.10}$$

and

$$\frac{\eta_\nu(\boldsymbol{x},t;\boldsymbol{n})}{\alpha_\nu(\boldsymbol{x},t;\boldsymbol{n})} \simeq \frac{2\nu_{10}^2}{c^2}k_BT_s(\boldsymbol{x},t), \tag{4.1.11}$$

where we have used Einstein relations Eq. (A.0.6) and characterized the number density fraction between n_0 and n_1 by $T_s \gg h\nu_{10}/k_B$ (we will look into details of T_s in the next section).

When the radiation follows the Planck distribution, we can define the brightness temperature by Rayleigh-Jeans approximation as

$$T_b\left(\nu\right) \simeq \frac{c^2}{2k_B\nu^2}I_\nu, \tag{4.1.12}$$

with $h\nu \ll k_B T_b$, which is the case for the 21cm line. Using this relation, we can solve Eq. (4.1.3) as

$$\frac{dT_b(\nu)}{d\tau_\nu} = -T_b(\nu) + \left(\frac{\nu_{10}}{\nu}\right)^2 T_s\left(\boldsymbol{x}, t\right). \tag{4.1.13}$$

$$\therefore \quad \delta T_b \equiv T_b\left(\nu, \boldsymbol{x}(\tau_\nu), \tau_\nu\right) - T_b\left(\nu, \boldsymbol{x}(0), 0\right), \tag{4.1.14}$$

$$= \left(1 - e^{-\tau_\nu}\right)\left[\left(\frac{\nu_{10}}{\nu}\right)^2 T_s - T_b\left(\nu, \boldsymbol{x}(0), 0\right)\right]. \tag{4.1.15}$$

Therefore, when $T_s < T_b$, the brightness temperature should be decreased, which shows that the photons from the background sources are absorbed by the neutral hydrogen. On the other hand, when $T_s > T_b$, the brightness temperature is enhanced by the emission of the 21cm photons from the neutral hydrogen.

4.2 Spin Temperature

In the following sections, we focus on 21cm line and introduce various relations that will be used in Part II.

As we mentioned at the beginning, the $1s$ state of neutral hydrogen is splitted into two states by the spin-spin interaction between the nucleon and electron. Because of its simple structure, the energy difference between these two states are precisely determined as

$$\Delta E = \frac{8}{3}\frac{e^2}{2a_0}g_p\frac{m_p}{M_{\mathrm{Pl}}}\alpha_{\mathrm{em}}^2 \simeq 5.8 \times 10^{-6} \text{ eV}, \tag{4.2.1}$$

where e is the electric charge, a_0 is the Bohr radius, $g_p = 5.56$, and $\alpha_{\mathrm{em}} = 1/137$. Because this energy difference corresponds to the wavelength of 21cm, the emission (or absorption) line by the transition between these states is called 21cm line. The situation is roughly described in Fig. 4.2.1.

To calculate the brightness temperature, we need to estimate the number density ratio between the excited state n_1 and the ground state n_0. The common way to describe it is the spin temperature T_s [133]. Assuming that the neutral hydrogen follows the Boltzmann distribution, the spin temperature T_s is defined as

$$\frac{n_1}{n_0} \equiv \frac{g_1}{g_0}\exp\left(-\frac{h\nu_{10}}{k_B T_s}\right) \equiv 3\exp\left(-\frac{T_*}{T_s}\right), \tag{4.2.2}$$

where $g_1 = 3$, $g_0 = 1$ are the degrees of freedom of the excited state and the ground state of neutral hydrogen respectively, and $T_* \equiv h\nu_{10}/k_B \simeq 68$ mK.

As we mentioned, in a two-level system of neutral hydrogen the three processes, spontaneous emission, excitation, and stimulated emission, should be taken into account. The rate of spontaneous emission has already been calculated as $A_{10} = 2.85 \times 10^{-15}$ s^{-1}. This rate $\sim 10^7$ year per particle is too small for the emission to be observed in laboratory experiments, but in the cosmological context where plenty of neutral hydrogen exists, this interaction highly matters.

The transition rate of the other two processes depends on the details of interactions, so we briefly focus on each of them below.
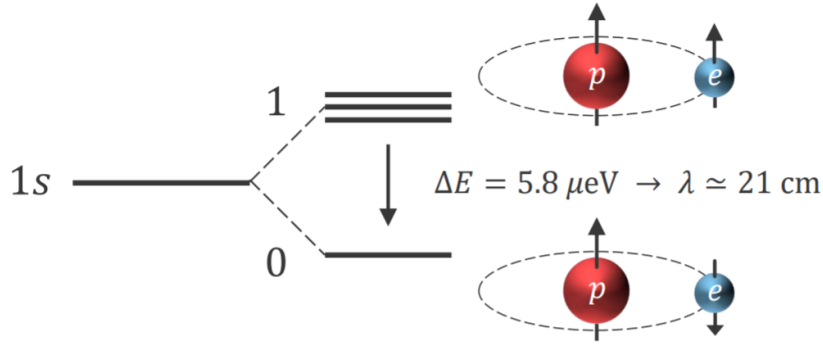
Figure 4.2.1: The picture of 21cm line. The $1s$ state of neutral hydrogen is splitted by the spin-spin interaction of the proton and the electron and each state numbered by 0 and 1 has 1 and 3 degrees of freedom, respectively. The energy difference between them is precisely calculated as $\Delta E \simeq 5.87$ μeV, which corresponds to $\nu_{10} \simeq 1.42$ GHz and $\lambda_{10} \simeq 21.11$ cm.

Collisions

First, let us consider collisional processes of neutral hydrogen. The angular momentum of neutral hydrogen, i.e. the spin in the case of the $1s$ state, is altered by collisions with other spinful particles. In the early universe, there are three main processes of collision interactions: $H - H$, $e - H$, and $p - H$ collisions. Each interaction affects the number density of n_0 and n_1 so that the spin angular momentum in the system is conserved. Suppose that the deexcitation rate of these collisional processes per excited particle is defined as C_{10}, it is decomposed into three parts,

$$C_{10} = n_{HI}\kappa_{10}^{HH} + n_e\kappa_{10}^{eH} + n_p\kappa_{10}^{pH}, \tag{4.2.3}$$

where $\kappa_{10}^{HH}, \kappa_{10}^{eH}$, and κ_{10}^{pH} are the cross sections of $H - H$, $e - H$, and $p - H$ collisions, respectively and n_{HI}, n_e, and n_p are the number densities of the neutral hydrogen, electrons, and protons, respectively. As we can find from Fig. 4.2.2 showing the values of κ's, the cross section of $e - H$ and $p - H$ collisions are larger than that of the $H - H$ collision. However, their contribution to C_{10} is generally negligible because the fraction of free electrons and protons before the reionization on which we generally focus in the 21cm line context is smaller than n_{HI}. Thus, we will ignore the effect of the $e - H$ and $p - H$ collisions, that is, we approximate

$$C_{10} \simeq n_{HI}\kappa_{10}^{HH}. \tag{4.2.4}$$

In a similar way, we also define the excitation rat as C_{01}.

Background Photons

The second is an interaction with background photons, which makes neutral hydrogen being excited or deexcited. The primary source of the background photons is CMB.
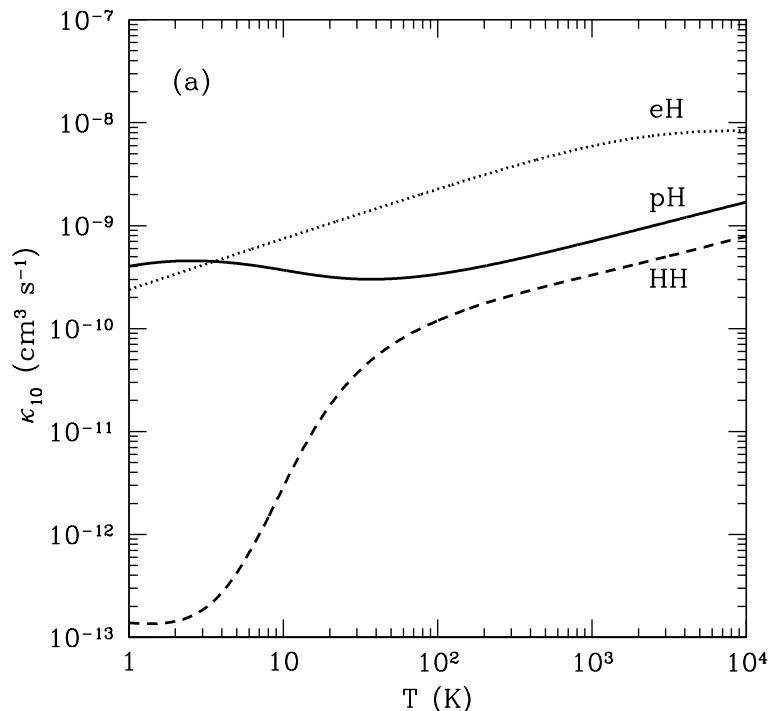
Figure 4.2.2: The cross section of $e - H$, $p - H$, and $H - H$ collisions reproduced from [134]. The dotted, solid, and dashed lines represent $e - H$, $p - H$, and $H - H$ collisions, respectively.

[1] As we define the Einstein coefficients in Appendix. A, we define the transition rates for the excitation and stimulated emission by $B_{01}(\nu)\rho_{\mathrm{CMB}}(\nu)$ and $B_{10}(\nu)\rho_{\mathrm{CMB}}(\nu)$. Here, $\rho_{\mathrm{CMB}}(\nu)$ is the energy density of CMB following the Planck distribution.

Lyman-α photons

The transition via Lyman-α energy levels which are the energy difference between the $2p$ state and the $1s$ state affect the number density of neutral hydrogen. Because of the electric dipole selection rules, the difference of the total angular momentum must satisfy $\Delta F = 0, 1$ except for the transition $F = 0 \rightarrow 0$ being prohibited. This effect is called Wouthuysen–Field effect [135, 136].

The Lyman-α photons are mainly created from stars, but the star formation process within $z \lesssim 30$ strongly depends on the astrophysics and contains uncertainties. Thus, we ignore the Lyman-α contribution for just simplicity in this thesis in Part II. We define the excitation and deexcitation rates as P_{01} and P_{10}, respectively.

Finally, let us comment on the variation of the fraction of neutral hydrogen. So far we have focused on the process that does not change the total number density of neutral

---

[1]We ignore the contribution from the emission of 21cm line as the background sources because it is small compared to CMB.

hydrogen $n_{HI} \equiv n_0 + n_1$, but the fraction of neutral hydrogen changes as the evolution of the universe due to the ionization effects. Thus, n_{HI} is indeed written as

$$n_{HI}(t) = x_{HI}(t)n_H, \tag{4.2.5}$$

where n_H is the number density of the total hydrogen and x_{HI} is the time-depending neutral fraction of hydrogen. However, the time variation of x_{HI} is ignorable in most of the epoch of 21cm line observations. Therefore, we ignore it throughout this thesis.

When the time scale of these three processes are much shorter than the Hubble expansion rate, we can safely assume that these three processes are in equilibrium. In this case, because the rate of change of the number density are equal to each other,

$$\dot{n}_0 = \dot{n}_1, \tag{4.2.6}$$
$$\Leftrightarrow \quad (C_{01} + P_{01})\, n_0 - B_{10}(\nu)\rho_{\mathrm{CMB}}(\nu)n_1 = (C_{10} + P_{10} + A_{10})\, n_1 - B_{01}(\nu)\rho_{\mathrm{CMB}}(\nu)n_0. \tag{4.2.7}$$

Using the relation that T_* is much smaller than T_γ, T_K, T_α and the Einstein relation derived in Appendix A, we can derive the spin temperature as

$$T_s^{-1} = \frac{C_{10}T_K^{-1} + P_{10}T_c^{-1} + A_{10}T_*^{-1}}{C_{10} + P_{10} + A_{10} + B_{10}(\nu)\rho_{\mathrm{CMB}}(\nu)}, \tag{4.2.8}$$
$$\simeq \frac{T_\gamma^{-1} + x_c T_K^{-1} + x_\alpha T_\alpha^{-1}}{1 + x_c + x_\alpha}, \tag{4.2.9}$$

where

$$x_c \equiv \frac{C_{10}}{A_{10}}\frac{T_*}{T_\gamma} \simeq \frac{\kappa_{10}^{HH}n_{\mathrm{HI}}(\boldsymbol{x})}{A_{10}}\frac{T_*}{T_\gamma}, \tag{4.2.10}$$
$$x_\alpha \equiv \frac{P_{10}}{A_{10}}\frac{T_*}{T_\gamma}. \tag{4.2.11}$$

From this formula, we can find that the spin temperature is determined by the process that gives the strongest coupling among the three processes.

4.3   21cm Forest

So far, we have discussed the general features of 21cm line. In this section, we explain what is the 21cm forest and its advantages on the 21cm line.

Generally, in the context of the 21cm line we use CMB as a backlight because it is ubiquitous around the universe and contains a vast range of frequencies. However, it is very challenging to determine the cosmic structure by CMB observations of 21cm lines mainly because of the observational difficulties. The amplitude of foregrounds of both galactic and extra-galactic sources is several orders of magnitude larger than the signals. Thus, further detailed simulations and analytical developments are necessary for those foregrounds to be safely removed. In addition, as you can see from Eq. (4.1.15) the spin temperature must be different from the CMB temperature $T_s \neq T_\gamma$ to observe the
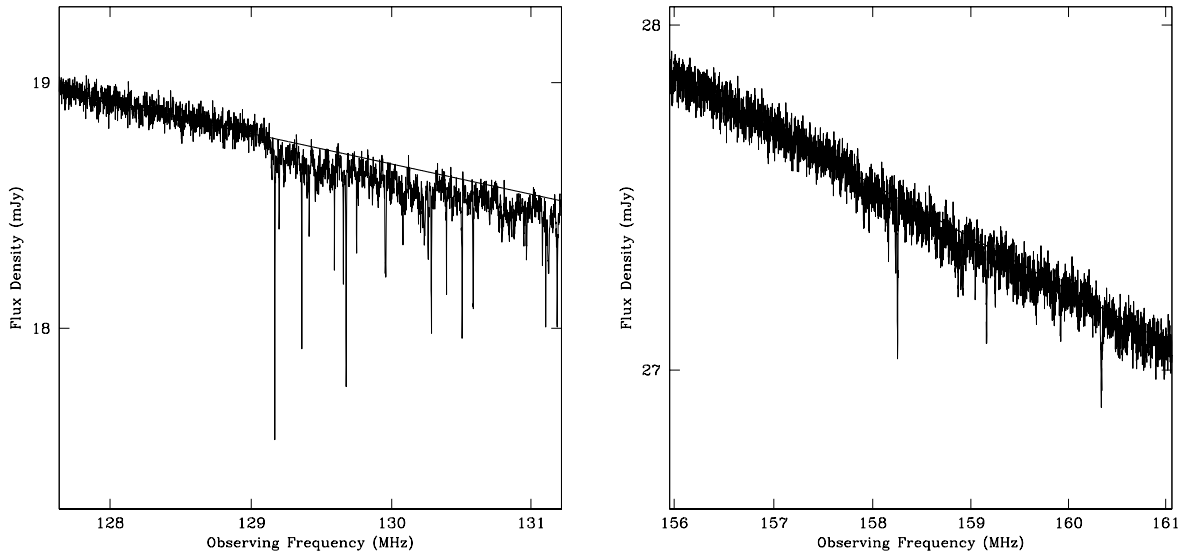
Figure 4.3.1: Mock spectra of radio sources at $z = 10$ (left) and $z = 8$ (right) taken from Ref. [49]. In both cases, a source (with luminosity equal to Cygnus A) is placed at the appropriate redshift and observed by an SKA-class instrument.

absorption or emission process by neutral hydrogen. This condition makes observations impossible during certain epochs before the reionization $z \gtrsim 6$.

An important alternative to the CMB is a radio rich source as a backlight, such as quasars or gamma-ray bursts (GRBs). The advantage of this method is the ease of observations because of the high signal-to-noise ratio of the bright source with the typical temperature $\sim 10^{11-12}$ K much higher than that of CMB. Besides, the 21cm line is always observed as absorption against the source because $T_s \ll T_b$ always holds. In this case, photons from the source are subsequently absorbed by IGM, cosmic web, and mini-halos, which creates a number of consecutive absorption lines in the spectrum due to the redshift. This phenomenon is called 21cm forest in analogy with Lyman-α forest [49, 50, 137]. Especially in the case of mini-halos, because the typical line width $\sim$ kHz produced by thermal broadening is distinguishable by observations, it enables us to resolve detailed information on small scales. The key problems of observations of the 21cm forest are the existence of background sources and the IGM temperature. We will discuss them in Sec. 6.5 in Part II.

Part II

Original Works

Chapter 5

Oscillon Power Spectrum

The cosmological effects of oscillons have long been discussed mainly with gravitational waves generated at oscillon formation and phenomenology of long-lived oscillons in the recent universe has never been considered. In this chapter, to discuss the effects of oscillons on the recent universe, we analytically derive the power spectrum produced by oscillons and confirm the agreement between the analytical result and the result of lattice simulations.

Here, we assume that ULAP consists of a coherently oscillating part and an oscillon part, that is, the power spectrum of ULAP P_ϕ on a comoving scale $\boldsymbol{k}$ is decomposed as

$$P_\phi(\boldsymbol{k}) = P_{\mathrm{coh}}(\boldsymbol{k}) + P_{\mathrm{osc}}(\boldsymbol{k}), \tag{5.0.1}$$

where $P_{\mathrm{coh}}(\boldsymbol{k})$ and $P_{\mathrm{osc}}(\boldsymbol{k})$ are the matter power spectrum of the coherent part and the oscillon part, respectively. We only focus on $P_{\mathrm{osc}}(\boldsymbol{k})$ in this chapter defined as

$$\langle \delta_{\mathrm{tot}}(\boldsymbol{k}) \delta_{\mathrm{tot}}(\boldsymbol{k}') \rangle = (2\pi)^3 \delta(\boldsymbol{k} + \boldsymbol{k}') P_{\mathrm{osc}}(\boldsymbol{k}), \quad \delta_{\mathrm{tot}}(\boldsymbol{k}) = \int d^3 x \delta_{\mathrm{tot}}(\boldsymbol{x}) e^{-i\boldsymbol{k}\cdot\boldsymbol{x}}, \tag{5.0.2}$$

where δ_{tot} is the energy fraction of all oscillons to the total energy density of ULAP (will be defined in Sec. 5.1).

Throughout this chapter, we will use the position $\boldsymbol{x}$ and the wavenumber $\boldsymbol{k}$ as the comoving value unless otherwise stated.

5.1   Analytical Formula

In this section, we analytically derive the oscillon power spectrum $P_{\mathrm{osc}}(k)$ to be compared with the simulation result later in Sec. 5.3. First, we roughly estimate the power spectrum ignoring oscillon sizes and the energy conservation in the horizon. Second, we calculate the more precise formula which coincides with the rough estimation except for some overall factors. Although we only focus on oscillons in this section, the procedure here is also applicable to all kinds of compact objects, such as primordial black holes, ultra-compact mini halos, and so on.

5.1.1   Rough Estimation

First, to clarify the overall picture, we roughly estimate the analytical formula of the power spectrum of oscillons. In this subsection, we make two assumptions for simplicity,

- we ignore the size of oscillons and treat them as point-like particles.

- oscillons are completely randomly distributed in the entire universe.

Note that in the actual case the second assumption is partially incorrect and we will take it into account in the next subsection.

Let us consider a box with a comoving volume V in which the number of oscillons with the energy E_i is represented by N_i. Because of the second assumption, N_i follows the Poisson distribution, i.e.

$$\langle (N_i - \langle N_i \rangle_N)(N_j - \langle N_j \rangle_N) \rangle_N = \langle N_i \rangle_N \delta_{ij}, \tag{5.1.1}$$

where $\langle \rangle_N$ shows statistical average over N_i. The density contrast of oscillons to ULAP is represented by

$$\delta_{\text{tot}} = r_{\text{osc}} \frac{\sum_i N_i E_i - \langle \sum_i N_i E_i \rangle_N}{\langle \sum_i N_i E_i \rangle_N}, \tag{5.1.2}$$

where r_{osc} is the energy fraction of oscillons to all ULAP defined as

$$r_{\text{osc}} \equiv \frac{\langle \sum_i N_i E_i \rangle_N}{\rho_\phi}. \tag{5.1.3}$$

with ρ_ϕ being the total energy density of ULAP. Then, defining the physical number density of oscillons as

$$n_{\text{osc}} = \frac{\sum_i \langle N_i \rangle_N}{a^3 V}, \tag{5.1.4}$$

the oscillon power spectrum is derived as

$$P_{\text{osc}}(\boldsymbol{k}) = V \langle \delta^2 \rangle_N, \tag{5.1.5}$$

$$= V \frac{r_{\text{osc}}^2}{\langle \sum_i N_i E_i \rangle_N^2} \sum_{i,j} E_i E_j \langle (N_i - \langle N_i \rangle_N)(N_j - \langle N_j \rangle_N) \rangle_N, \tag{5.1.6}$$

$$= V \frac{r_{\text{osc}}^2}{\langle \sum_i N_i E_i \rangle_N^2} \sum_i E_i^2 \langle N_i \rangle_N, \tag{5.1.7}$$

$$= \frac{r_{\text{osc}}^2}{n_{\text{osc}} a^3} \frac{\langle E^2 \rangle}{\langle E \rangle^2}. \tag{5.1.8}$$

where we have defined the average of the oscillon energy and squared oscillon energy as

$$\langle E \rangle \equiv \frac{\sum_i E_i \langle N_i \rangle_N}{\sum_i \langle N_i \rangle_N}, \quad \langle E^2 \rangle \equiv \frac{\sum_i E_i^2 \langle N_i \rangle_N}{\sum_i \langle N_i \rangle_N}. \tag{5.1.9}$$

From this formula, we can find that the power spectrum is inversely proportional to the comoving number density of oscillons $n_{\text{osc}} a^3$ except for the factor r_{osc}^2 when the oscillon

energies are monotonic. This simple result $P(k) = \text{const}$ on all scales is the typical feature of the Poisson power spectrum.

In the following subsection, we will consider the more realistic situation where the above two assumptions are slightly violated and show that these effects suppress the Poisson power spectrum at some corresponding scale.

5.1.2 Precise Calculation

In this subsection, to estimate the oscillon power spectrum more precisely we include two more factors: the oscillon size and the violation of the random distribution over the horizon as opposed to the previous subsection. The discussion in this subsection is more general than that of the previous subsection Eq. (5.1.8) which would be reproduced in the limit where the effects of these two factors are negligible.

For analytical calculations, we approximate the spatial oscillon profile as a Gaussian function.

$$\phi\left(x; \boldsymbol{x}_i\right) = \Phi\left(r; \boldsymbol{x}_i\right) \cos \omega t, \tag{5.1.10}$$

$$\simeq \Phi_0 \exp\left(-\frac{a^2 r^2}{2R^2}\right) \cos \omega t. \tag{5.1.11}$$

where ω is the oscillation frequency, $\boldsymbol{x}_i$ is the comoving position of the i-th oscillon, and $r = |\boldsymbol{x} - \boldsymbol{x}_i|$. We assume that the positions of oscillons are not correlated. The central amplitude of the oscillon Φ_0 and the physical radius of the oscillon R should be determined by the fitting to the analytical solution derived from Eq (2.2.4). The Gaussian fitting does not work well when the oscillon profile is flat-top. This kind of profile is realized, for example, when the central amplitude is close to the extremum, which results in the field remaining for a long time before beginning to roll. In this case, the cutoff scale $k/a \sim R^{-1}$ of the oscillon power spectrum would be changed as we will see later.

Then, the energy density of a single oscillon in the FRW universe is

$$\rho_{\text{osc}}\left(\boldsymbol{x}; \boldsymbol{x}_i\right) \simeq \frac{1}{2}\left[\left(\frac{d\phi}{dt}\right)^2 + \frac{1}{a^2}\left(\frac{d\phi}{dr}\right)^2 + m^2\phi^2\right], \tag{5.1.12}$$

$$\simeq \frac{1}{2}\Phi(r)^2\left[\omega^2 \sin^2 \omega t + \left(\frac{a^2 r^2}{R^4} + m^2\right)\cos^2 \omega t\right], \tag{5.1.13}$$

$$\simeq \frac{\omega^2 \Phi_0^2}{2} \exp\left(-\frac{a^2 r^2}{2R^2}\right), \tag{5.1.14}$$

where we have ignored the spatial gradient term in the last line because the energy density of the oscillon is dominant in $ar < R$. Defining the oscillon fraction to the total ULAP energy density as

$$\delta_{\text{osc}}(\boldsymbol{x}; \boldsymbol{x}_i) \equiv \frac{\rho_{\text{osc}}(\boldsymbol{x}; \boldsymbol{x}_i)}{\rho_\phi}, \tag{5.1.15}$$

where ρ_ϕ is the total energy density of ULAP, the oscillon fraction in k-space is calculated by Fourier transformation as

$$\delta_{\mathrm{osc}}(\boldsymbol{k};\boldsymbol{x}_i) = \int \delta_{\mathrm{osc}}(\boldsymbol{x};\boldsymbol{x}_i)e^{-i\boldsymbol{k}\cdot\boldsymbol{x}}d^3x, \tag{5.1.16}$$

$$\simeq \frac{\omega^2\Phi_0^2}{2\rho_\phi}\left(\pi\frac{R^2}{a^2}\right)^{3/2}\exp\left(-i\boldsymbol{k}\cdot\boldsymbol{x}_i - \frac{k^2R^2}{4a^2}\right), \tag{5.1.17}$$

$$\simeq \frac{E_i}{\rho_\phi a^3}\exp\left(-i\boldsymbol{k}\cdot\boldsymbol{x}_i - \frac{k^2R^2}{4a^2}\right). \tag{5.1.18}$$

where E_i is the total energy of the i-th oscillon defined by

$$E_i \equiv a^3\int_0^\infty d^3x\rho_{\mathrm{osc}}\left(\boldsymbol{x};\boldsymbol{x}_i\right) \simeq \frac{\omega^2\Phi_0^2}{2}\left(\pi R^2\right)^{3/2}. \tag{5.1.19}$$

Considering a large comoving volume $V = L^3$ which contains N_{osc} oscillons, the total fraction of the oscillons to ULAP is obtained by summing over all oscillons,

$$\delta_{\mathrm{tot}}(\boldsymbol{k};\boldsymbol{x}_i) = \sum_{i=1}^{N_{\mathrm{osc}}}\delta_{\mathrm{osc}}\left(\boldsymbol{k};\boldsymbol{x}_i\right). \tag{5.1.20}$$

Then, the expected value of the oscillon power spectrum is given by averaging over the all positions of the oscillons as

$$P_{\mathrm{osc}}(k) \equiv \left(\prod_{i=1}^{N_{\mathrm{osc}}}\int\frac{d^3x_i}{V}\right)\frac{|\delta_{\mathrm{tot}}\left(\boldsymbol{k};\boldsymbol{x}_i\right)|^2}{V}, \tag{5.1.21}$$

$$= \frac{1}{(\rho_\phi a^3)^2}\frac{1}{V}\left(\prod_{i=1}^{N_{\mathrm{osc}}}\int\frac{d^3x_i}{V}\right)\left|\sum_{i'=1}^{N_{\mathrm{osc}}}E_{i'}\exp\left[-i\boldsymbol{k}\cdot\boldsymbol{x}_{i'} - \frac{k^2R\left(M_{i'}\right)^2}{4a^2}\right]\right|^2. \tag{5.1.22}$$

To perform the integration, we need to make a practical assumption: there is a comoving scale $(R/a <) L_s < L$ inside which the total energy of oscillons conserves. This assumption naively reflects the energy conservation inside the horizon at oscillon formation and will be confirmed in Sec. 5.3. Besides, just for simplicity, we further assume that the number of oscillons in each volume L_s^3 is equal as $N_s \equiv N_{\mathrm{osc}}/\left(L/L_s\right)^3$.

First, let us consider fluctuations on a comoving scale larger than L_s, that is, $kL_s < 1$. In this case, we can safely ignore the exponential factor in Eq. (5.1.22)

$$\exp\left[-\frac{k^2R\left(M_i\right)^2}{4a^2}\right], \tag{5.1.23}$$

and only the phase factor matters.

$$\left(\prod_{i=1}^{N_{\mathrm{osc}}}\int\frac{d^3x_i}{V}\right)\left|\sum_{i'=1}^{N_{\mathrm{osc}}}E_{i'}e^{-i\boldsymbol{k}\cdot\boldsymbol{x}_i}\right|^2 = \left(\prod_{i=1}^{N_{\mathrm{osc}}}\int\frac{d^3x_i}{V}\right)\sum_{i',i''=1}^{N_{\mathrm{osc}}}E_{i'}E_{i''}e^{-i\boldsymbol{k}\cdot(\boldsymbol{x}_{i'}-\boldsymbol{x}_{i''})}. \tag{5.1.24}$$

Because of the random distribution of the oscillon positions, we can seperately consider each direction. Let us consider the x direction, for example, and define the j-th region of the volume V in x direction as $[(j-1)L_s, jL_s]$ for $j = 1, \cdots, L/L_s$ and the position and the oscillon energy of the i-th oscillon in the j-th region as $\boldsymbol{x}_{ij}, E_{ij}$, respectively. Using the integration

$$\int_{(j-1)L_s}^{jL_s} \frac{dx_{ij}}{L_s} e^{-ikx_{ij}} \equiv \epsilon e^{-ijkL_s}, \quad \epsilon \equiv \frac{1}{ikL_s}\left(1 - e^{-ikL_s}\right), \tag{5.1.25}$$

the phase factor in x dimension is calculated as

$$\left(\prod_{i=1}^{N_{\rm osc}} \int \frac{dx_i}{L_s}\right) \sum_{i',i''=1}^{N_{\rm osc}} E_{i'} E_{i''} e^{-ik(x_{i'}-x_{i''})} \tag{5.1.26}$$

$$= \left(\prod_{j=1}^{L/L_s} \prod_{i=1}^{N_s} \int_{(j-1)L_s}^{jL_s} \frac{dx_{i,j}}{L_s}\right) \left[\sum_{j',j''=1}^{L/L_s} \sum_{i',i''=1}^{N_s} E_{i'j'} E_{i''j''} e^{-ik\left(x_{i'j'}-x_{i''j''}\right)}\right]. \tag{5.1.27}$$

$$= \sum_{j=1}^{L/L_s} \left(\sum_{i'=1}^{N_s} E_{i'j}^2 + |\epsilon|^2 \sum_{i'\neq i''}^{N_s} E_{i'j} E_{i''j}\right) + |\epsilon|^2 \sum_{j'\neq j''}^{L/L_s} \sum_{i',i''=1}^{N_s} E_{i'j'} E_{i''j''} e^{-i(j'-j'')kL_s}, \tag{5.1.28}$$

$$= \sum_{j=1}^{L/L_s} \sum_{i=1}^{N_s} \left(1 - |\epsilon|^2\right) E_{ij}^2 + |\epsilon|^2 E_s^2 \frac{L}{L_s} + |\epsilon|^2 E_s^2 \left[\left|\sum_{j=1}^{L/L_s} e^{-ijkL_s}\right|^2 - \frac{L}{L_s}\right], \tag{5.1.29}$$

$$= \sum_{j=1}^{L/L_s} \sum_{i=1}^{N_s} E_{ij}^2 \left[1 - \left(\frac{2}{kL_s}\right)^2 \sin^2\left(\frac{kL_s}{2}\right)\right], \tag{5.1.30}$$

where we have used the energy conservation in the box L_s as

$$\sum_{i=1}^{N_s} E_{ij} = E_s, \tag{5.1.31}$$

and

$$\sum_{j=1}^{L/L_s} e^{-ijkL_s} = 0. \tag{5.1.32}$$

The first, second, and third term in the third line correspond to the terms of $i' = i''$ and $j' = j''$, $i' \neq i''$ and $j' = j''$, and $j' \neq j''$, respectively. In three dimenstions, the overall sum $\sum^{L/L_s}$ is replaced by $\sum^{(L/L_s)^3}$ and the power spectrum in $k < 2\pi/L_s$ becomes

$$P_{\rm osc}(k) = \frac{1}{(\rho_\phi a^3)^2} \frac{N_{\rm osc} \langle E^2 \rangle}{V} \left[1 - \left(\frac{2}{kL_s}\right)^2 \sin^2\left(\frac{kL_s}{2}\right)\right], \tag{5.1.33}$$

where the bracket $\langle \rangle$ represents the ensemble average over $N_{\rm osc}$ oscillons.

On the other hand, when we consider the fluctuations on a scale smaller than L_s, that is, $kL_s > 1$, we should take into account the exponential factor of the oscillon

41

profile while the suppression factor ϵ converges to 0. Thus, we can easily calculate the integration in this case as

$$\left(\prod_{i=1}^{N_{\text{osc}}} \int \frac{d^3 x_i}{V} \right) \left| \sum_{i'=1}^{N_{\text{osc}}} E_{i'} e^{-i\boldsymbol{k}\cdot\boldsymbol{x}_i} \right|^2 = N_{\text{osc}} \left\langle E^2 \exp\left[-\frac{k^2 R\left(E\right)^2}{2a^2} \right] \right\rangle. \tag{5.1.34}$$

The above formula coincides with Eq. (5.1.33) when $kR/a < 1 < kL_s$. Therefore, defining the physical number density of oscillons n_{osc} and the energy ration of oscillons to ULAP r_{osc} as

$$n_{\text{osc}} \equiv \frac{N_{\text{osc}}}{a^3 V}, \quad r_{\text{osc}} \equiv \frac{n_{\text{osc}}\langle E \rangle}{\rho_\phi}, \tag{5.1.35}$$

the power spectrum of oscillons is approximated as

$$P_{\text{osc}}(k) = \frac{1}{(\rho_\phi a^3)^2} \frac{N_{\text{osc}} \left\langle E^2 \exp\left[-\frac{k^2 R(E)^2}{2a^2} \right] \right\rangle}{V} \left[1 - \left(\frac{2}{kL_s} \right)^2 \sin^2\left(\frac{kL_s}{2} \right) \right], \tag{5.1.36}$$

$$= \frac{r_{\text{osc}}^2}{n_{\text{osc}} a^3} \frac{\left\langle E^2 \exp\left[-\frac{k^2 R(E)^2}{2a^2} \right] \right\rangle}{\langle E \rangle^2} \left[1 - \left(\frac{2}{kL_s} \right)^2 \sin^2\left(\frac{kL_s}{2} \right) \right], \tag{5.1.37}$$

where we have ignored the fluctuations around the ensemble average because they vanish in the large limit of V.

This power spectrum has three qualitative features.

- $k \ll L_s^{-1}$: On a scale smaller than the energy conservation scale L_s, the oscillon power spectrum is proportional to k^2 as calculated above. This cutoff scale L_s is roughly estimated by the horizon size at oscillon formation, but more precisely it should be determined by lattice simulation.

- $L_s^{-1} \ll k \ll (R/a)^{-1}$: On a scale between the energy conservation scale L_s and the comoving oscillon size R/a, both suppression factors are ignored and the power spectrum is almost a constant. This formula reproduces the simple Poisson distribution of oscillons $P_{\text{osc}} \sim r_{\text{osc}}^2/(n_{\text{osc}} a^3)$ which is obtained when $\boldsymbol{x}_i$ is randomly distributed in the previous section.

- $(R/a)^{-1} \ll k$: On a scale smaller than the comoving oscillon size R/a, the power spectrum is exponentially cut off because we have assumed the oscillon profile as a Gaussian function. A different form of the profile, of course, affects the k-dependence of the cutoff.

These three features are realized if the assumptions are satisfied that oscillons with the size $\sim m^{-1}$ are randomly produced inside the horizon and the total energy on a scale larger than the horizon scale is conserved. Let us verify these assumptions by classical lattice simulation in the next section.
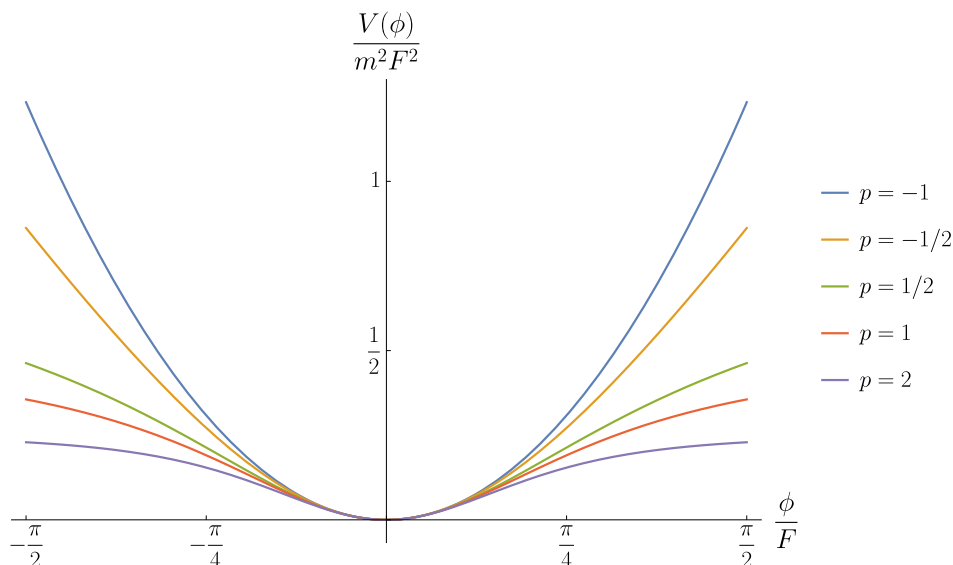
Figure 5.2.1: The shape of the ULAP potential Eq. (5.2.1) for various p's. The quadratic potential is realized when $p = -1$ and the potential gets shallower than quadratic as p gets larger.

5.2 Simulation Setup

In this section, we explain the setup of the classical lattice simulation to calculate the oscillon power spectrum. As the ULAP potential, we choose the monodromy type potential [28, 27, 34] for instance,

$$V(\phi) = \frac{m^2 F^2}{2p} \left[1 - \left(1 + \frac{\phi^2}{F^2} \right)^{-p} \right], \tag{5.2.1}$$

where m is the ULAP mass and F is the ULAP decay constant. The oscillon formation with $p > -1$ (except for $p = 0$) has already been confirmed in Refs. [57, 42] and the long lifetime of resultant oscillons is also investigated in Refs. [41, 38, 39]. We will confirm the validity of the analytical formula of the oscillon power spectrum Eq. (5.1.37) in various p's. Note that any potentials should be fine with the discussion below if it can produce oscillons.

5.2.1 Simulation Parameters

In our simulations, the units of the field, time, and space, etc. are taken to be F and m^{-1}, that is,

$$\bar{\phi} \equiv \frac{\phi}{F}, \quad \bar{\tau} \equiv m\tau, \quad \bar{x} \equiv mx, \quad \dots \text{ etc.} \tag{5.2.2}$$

where the overline denotes the dimensionless program variables and τ is the conformal time. In this normalization, the energy of an oscillon E is normalized as

$$\overline{E} = \frac{m}{F^2} E, \tag{5.2.3}$$

43

Table 5.1: Simulation parameters. Note that we also simulate in two dimensions only for $p = -1/2$.

	Index p			
	$-3/4$	$-1/2$		2
Box Size L	32	1024	32	16
Grid Size N	1024^3	32768^2	1024^3	1024^3
Time Step $\Delta\bar{\tau}$	8.0×10^{-3}	4.0×10^{-3}	8.0×10^{-3}	8.0×10^{-3}
Final Time		81.0		
Initial Value $\bar{\phi}_0$	12π	5π	$5\pi/2$	$7\pi/10$
Threshold $\bar{\rho}_{\text{th}}$	0.05	0.025	0.05	0.01

because of the relation $E = \int \rho_{\text{osc}} d^3 x = F^2/m \int \bar{\rho}_{\text{osc}} d^3 \bar{x}$.

Then, the equation of motion of $\bar{\phi}$ is represented by

$$\bar{\phi}'' + 2\frac{\bar{a}'}{\bar{a}}\bar{\phi}' - \bar{\Delta}\bar{\phi} + \bar{a}^2 \frac{\partial \overline{V}}{\partial \bar{\phi}} = 0, \quad \overline{V} = \frac{1}{2p}\left[1 - \left(1 + \bar{\phi}^2\right)^{-p}\right]. \tag{5.2.4}$$

where the dash denotes the derivative with respect to $\bar{\tau}$.

As the initial condition, we take the initial Hubble parameter as $H_i = 1/2t = m$ because we are interested in ULAP which starts to oscillate in the radiation dominated era. The initial scale factor is set to be unity as $\bar{a}_i = 1$, which produces $\bar{a} = \bar{\tau}$ in the radiation dominated universe. The initial field value and its derivative are set as

$$\bar{\phi}_i(\boldsymbol{x}) = \bar{\phi}_0 \left[1 + \zeta(\boldsymbol{x})\right], \quad \bar{\phi}_i(\boldsymbol{x})' = 0. \tag{5.2.5}$$

where $\bar{\phi}_0$ is chosen to maximize the oscillon fraction (see Appendix C.2 for the details) shown in Table. 5.1. $\zeta(\boldsymbol{x})$ is the initial noise defined by the scale-free power spectrum

$$\langle \xi(\boldsymbol{k})\xi(\boldsymbol{k}')\rangle = (2\pi)^3 \delta^3(\boldsymbol{k} + \boldsymbol{k}')\frac{2\pi^2}{k^3}\mathcal{P}_\xi, \tag{5.2.6}$$

with a small constant $\mathcal{P}_\xi = 2.1 \times 10^{-9}$ just for reference [1].

Other simulation parameters are shown in Table 5.1. Note that we perform simulations of $p = -1/2$ in both two and three dimensions to correctly calculate the behavior on large scale.

---

[1]Note that this definition slightly changes in two dimension as

$$\langle \xi(\boldsymbol{k})\xi(\boldsymbol{k}')\rangle = (2\pi)^2 \delta^2(\boldsymbol{k} + \boldsymbol{k}')\frac{2\pi}{k^2}\mathcal{P}_\xi.$$
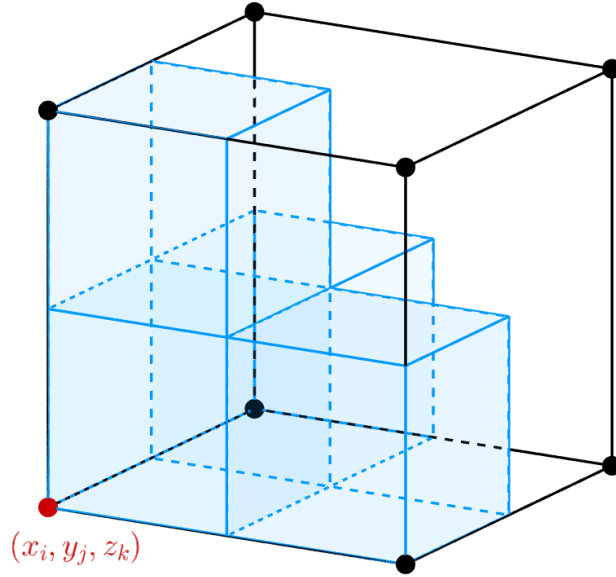
(x_i, y_j, z_k)

Figure 5.2.2: The intuitive picture of the method of the oscillon identification. When the energy density at the orange point (x_i, y_j, z_k) is larger than $\bar{\rho}_{\mathrm{th}}$, we take the average to calculate the midpoint value and identify the blue box regions as the oscillon. This method can include the tails of oscillon profiles to some extent.

We utilize our own lattice simulation code in which the time evolution is calculated by the fourth-order symplectic integration scheme and the spatial derivatives are calculated by the fourth-order central difference scheme. The details of the classical lattice simulation we use are explained in Appendix B. We impose the periodic boundary condition on the boundary and have confirmed that the results hardly depend on the box size.

5.2.2 Oscillon Identification

To calculate the oscillon power spectrum, we need to identify oscillons in the simulation box. In this subsection, we show how to identify oscillons and their energies in our simulations.

First, we assume that regions where the energy density $\bar{\rho}$ is larger than some threshold value $\bar{\rho}_{\mathrm{th}}$

$$\bar{\rho} > \bar{\rho}_{\mathrm{th}}, \tag{5.2.7}$$

are oscillons. The threshold value shown in Table 5.1 is chosen so that $\bar{\rho}_{\mathrm{th}} = \alpha \bar{\rho}_{\mathrm{th}} (\bar{\tau}_{\mathrm{end}})$ where α is $\mathcal{O}(0.1)$ parameter and $\bar{\tau}_{\mathrm{end}}$ is the end of the simulation. Then, to include the contribution from the tail of the oscillon profile correctly, we also regard one more grid outside the connected region of $\bar{\rho} > \bar{\rho}_{\mathrm{th}}$ as oscillons. The intuitive picture of this identification method is show in Fig. 5.2.2.

Following this method, the energy of an oscillon in D dimensional space is estimated

45

by summing over the energy density inside the identified region as

$$\overline{E} = \sum_{\boldsymbol{x}_i \in V_{\mathrm{osc}}} \overline{\rho}(\boldsymbol{x}_i) \left(\frac{\bar{a}L}{N}\right)^D ,$$

(5.2.8)

where the sum is over the grid inside the oscillon volume V_{osc}. The number of oscillons inside the simulation box N_{osc} is counted as the number of disconnected regions with $\overline{\rho} > \overline{\rho}_{\mathrm{th}}$.

We define the energy ratio of oscillons to the total energy of ULAP, the normalized physical number density of oscillons $\bar{n}_{\mathrm{osc}}$, and the average energy of the oscillons $\langle E \rangle$ as

$$r_{\mathrm{osc}} \equiv \frac{\sum_i^{N_{\mathrm{osc}}} \overline{E}_i}{\overline{\rho}(\bar{a}L)^D}, \quad \overline{n}_{\mathrm{osc}} = \frac{N_{\mathrm{osc}}}{(\bar{a}L)^D}, \quad \langle \overline{E} \rangle = \frac{1}{N_{\mathrm{osc}}} \sum_i^{N_{\mathrm{osc}}} \overline{E}_i.$$

(5.2.9)

Note that in these expressions we replace the statistical average of the number of oscillons in Eq. (5.1.8) with the simulation value. Because of the contribution from the surface region, the threshold value and the spatial resolution slightly change $\langle E \rangle$ and hence r_{osc}. We have confirmed that the estimation of r_{osc} differs less than 5% even if we vary the spatial resolution and the threshold value by a factor of 2. Please see Appendix C.1 for the details.

5.3   Simulation Result

In this section, we exhibit the results of our classical lattice simulations and confirm that the results coincide with the analytical formula Eq. (5.1.37).

5.3.1   Energy Distribution of Oscillons

To calculate the oscillon power spectrum Eq. (5.1.37), we need to derive the energy distributions of oscillons numerically. Here, we exhibit them and summarize the related values. We have simulated in each setup three times with different random seeds to reduce the stochastic noise.

The energy distributions of oscillons at the simulation end in three dimensions are shown in Fig. 5.3.1. We only exhibit the result of $p = -1/2, 2$ to avoid redundancy, but the same figure is also obtained for $p = -3/4$ and the two-dimensional case. From these figures, we can find that the smaller p leads to the larger E. This is mainly because the potential of $p = 2$ is shallower than that of $p = -1/2$ as shown in Fig. 5.2.1. As you can see from the profile equation Eq. (2.2.4), when we fix ω, the central amplitude must be larger in a shallower potential. In other words, when we fix the central amplitude, ω must be larger in a shallower potential. That is why the shallower potential, i.e., smaller p, generally produces larger oscillons. [2]

Using these mass distributions, we calculated $r_{\mathrm{osc}}, \overline{n}_{\mathrm{osc}}, \langle \overline{E} \rangle$ for each p, which are summarized in Table 5.2. We will use these results to calculate the analytical formula of

---

[2]Note that this explanation is not always correct because the size of produced oscillons is also affected by other parameters such as the initial amplitude and the shape of the potential.
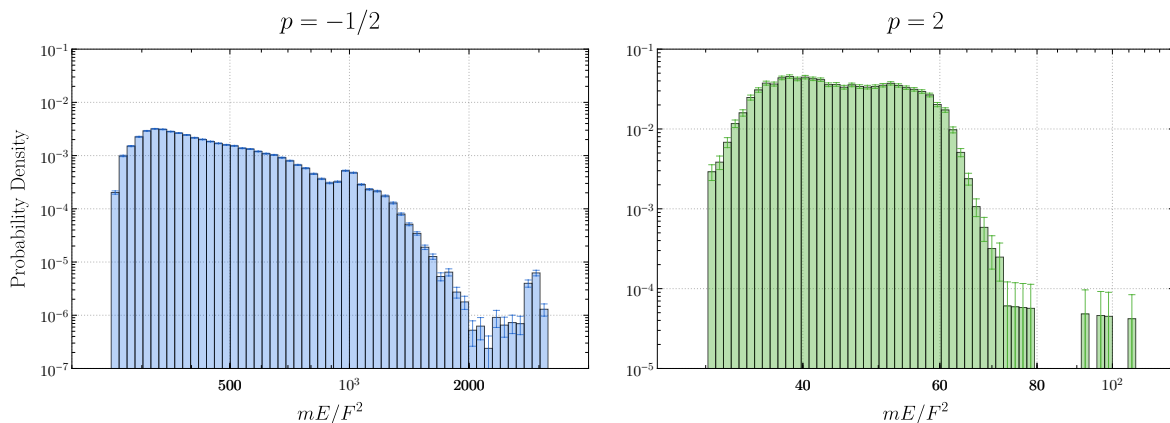
Figure 5.3.1: The left and right figures show the simulation results of the energy distribution of oscillons for $p = -1/2, 2$, respectively. The vertical axis shows the probability distribution and the horizontal axis shows the normalized energy of oscillons. The statistical error of each bar is calculated by $\sqrt{N_i}/(N_{\text{osc}}\Delta b_i)$ where N_i is the number of data in the i-th bin and Δb_i is the width of the i-th bin.

the oscillon power spectrum in the next subsection. From the value of $\overline{n}_{\text{osc}}$, the typical comoving distance between oscillons is estimated as

$$\left(n_{\text{osc}}a^3\right)^{-1/3} \sim \frac{m^{-1}}{a_m} \simeq 10^2 \text{ kpc} \left(\frac{m}{10^{-22} \text{ eV}}\right)^{1/2}, \tag{5.3.1}$$

where a_m is the scale factor at the simulation start $H = m$ when the current scale factor is normalized as 1. Thus, there is approximately one oscillon per 10^2 kpc with the physical size $\sim m^{-1} \simeq 0.1$ pc when $m = 10^{-22}$ eV.

Table 5.2: The summary of the simulation results only in three dimensions.

	Index p		
	$-3/4$	$-1/2$	2
r_{osc}	0.73	0.69	0.60
$\overline{n}_{\text{osc}}\overline{a}^3$	0.98	0.83	0.79
$\langle \overline{E} \rangle$	2100	570	47

5.3.2 Power Spectrum of Oscillons

In this subsection, we show the result of numerical calculations of the power spectrum after oscillon formation to validate the analytical estimation of the power spectrum Eq. (5.1.37). We only show the results of $p = -1/2$ here, but similar results are also obtained for $p = -3/4$ and 2.

47

In Fig. 5.3.2, the purple and green dots show the simulation results of the power spectrum at the end of the simulation when the oscillon formation has already finished. The red line shows the analytical power spectrum Eq. (5.1.37) based on the oscillon distribution calculated in the previous section Fig. 5.3.1 with the cutoff scale in Eq. (5.1.37) being $2\pi/(a_m L_s) = 0.35m$. From this figure, we can easily find that the numerical power spectra (purple and green dots) are well approximated by the analytical formula (red line).

As we discussed in Sec. 5.1.2, the power spectrum consists of three parts. The center plateau region corresponds to the Poisson distribution of the oscillons discussed in Sec. 5.1.1. The agreement between the analytical and numerical calculation suggests that the oscillons are produced randomly inside the horizon. On the scale smaller than the oscillon size $k/a_m \gtrsim \mathcal{O}(10)m$, the power spectrum decreases following the exponential oscillon profile. Because the dimensional difference of the spherically symmetric Laplacian of the oscillon profile equation Eq. (2.2.4) leads to the smaller friction and the smaller oscillon size in two dimensions, the two-dimensional result does not match the analytical formula at large k.

On the scale larger than L_s, the power spectrum decreases because of the energy conservation as we discussed in Sec. 5.1.2. This suppression, however, does not hold in the small k. For the three dimensional result (green dots), this is because the periodic boundary condition produces correlations on large scales that should not be correlated. This possibility is confirmed by the fact that the deviation scale heavily depends on the simulation box size. On the other hand, because the result of two dimensions does not depend on the box size, the deviation could have a physical meaning. One of the possibilities is that the total energy fluctuation inside each horizon produced by the fluctuation of the oscillon formation rate could result in another source of the Poisson noise. Because the assumption Eq. (5.1.31) does not hold in this case, we can find that the sum of the third term in Eq. (5.1.29) is replaced by

$$\left| \sum_{j=1}^{L/L_s} E_{sj} e^{-ijkL_s} \right|^2, \tag{5.3.2}$$

where E_{sj} is the total energy in the j-th box. When we assume that E_{sj} randomly fluctuates $\delta E_{sj}/E_s \gtrsim \mathcal{O}(1) \times 10^{-2}$ (see Fig. (C.2.1) in Appendix (C)), the contribution of the violation of the energy conservation is estimated as

$$|\epsilon|^2 E_s^2 \left| \sum_{j=1}^{L/L_s} \frac{\delta E_{sj}}{E_s} e^{-ijkL_s} \right|^2 \sim E_s^2 \frac{L}{L_s} \times 10^{-2}. \tag{5.3.3}$$

When it is divided by $\sum_i^{N_{\text{osc}}} E_i$, we can find that this contribution is roughly 10^{-2} times smaller than the power spectrum of the original plateau region, which reproduces the simulation result in Fig. 5.3.2.
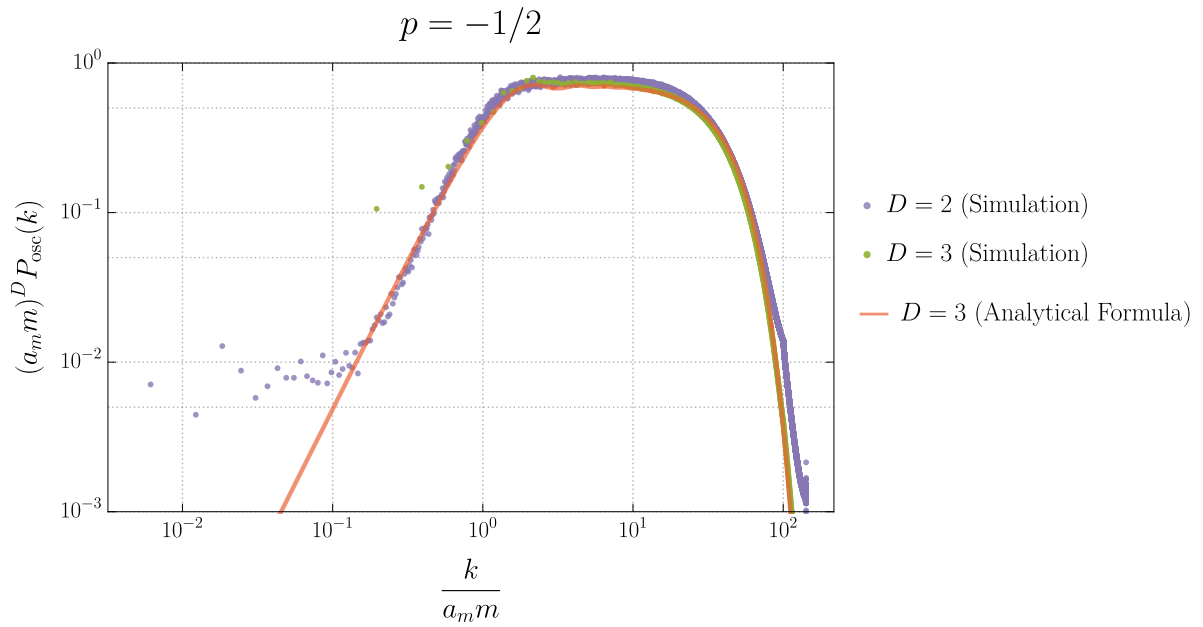
Figure 5.3.2: The comparison of simulation results and the analytical formula Eq. (5.1.37) of the oscillon power spectrum. The purple and green dots show the simulation results in two and three dimensions, respectively, and the red line shows the analytical formula with $k_s/a_m = 0.35m$.

Chapter 6

Detection of Oscillons of Ultra-Light Axion-like Particle by 21 cm Forest

In this chapter, we suggest that the long-lived ULAP oscillons could be detected by 21cm forest, the consecutive absorption of 21cm line. First, in Sec. 6.1, we analytically derive the matter power spectrum under the situation where the ULAP oscillons are present in the universe following the previous chapter. Next, in Sec. 6.2 we calculate the abundance of mini-halos using the power spectrum. Then, defining the halo and baryon profiles in Sec. 6.3, we calculate the abundance of 21cm absorption lines in Sec. 6.4. Finally, Sec. 6.5 is devoted to discussing the result.

Throughout this section, we use the same potential as the previous one

$$V(\phi) = \frac{m^2 F^2}{2p} \left[1 - \left(1 + \frac{\phi^2}{F^2} \right)^{-p} \right], \tag{6.0.1}$$

with $p > -1$ (except for $p = 0$). We assume that dark matter of the universe is consist of unknown cold dark matter, homogeneous ULAP, and ULAP oscillons as

$$\Omega_{\mathrm{DM}} = \Omega_{\mathrm{CDM}} + \Omega_{\mathrm{ULAP}}, \tag{6.0.2}$$
$$= \Omega_{\mathrm{CDM}} + \left(\Omega_{\mathrm{homo}} + \Omega_{\mathrm{osc}} \right). \tag{6.0.3}$$

For later use, we define the fraction of ULAP to dark matter f_{ULAP} as

$$\Omega_{\mathrm{ULAP}} \equiv f_{\mathrm{ULAP}} \Omega_{\mathrm{DM}}. \tag{6.0.4}$$

Note that the discussion in this chapter is applicable to any ULAP models if the decay rate of the oscillons is so small that we can observe them around $z \sim \mathcal{O}(10)$. All cosmological parameters in this paper are extracted from the result of Planck 2018 [6].

6.1 Matter Power Spectrum

First, in this section, we estimate the matter power spectrum of the dark matter consists of unknown cold dark matter, homogeneous ULAP, and ULAP oscillons following the calculation of the previous chapter.

The matter power spectrum $P(k)$ is decomposed as

$$P(k,t) = P_{\text{CDM}}(k,t) + P_{\text{ULAP}}(k,t), \qquad (6.1.1)$$
$$= P_{\text{CDM}}(k,t) + [P_{\text{coh}}(k,t) + P_{\text{osc}}(k,t)]. \qquad (6.1.2)$$

where $P_{\text{coh}}(k,t)$ and $P_{\text{osc}}(k,t)$ show the matter power spectra of homogeneous ULAP and ULAP oscillons, respectively, and we have assumed that the homogeneous part and the oscillon part are not correlated.

We calculate $P_{\text{CDM}}(k,t) + P_{\text{coh}}(k,t)$ from AxionCAMB code [123] originated from the public Boltzmann code CAMB [138, 139] in which the initial fluctuations of ULAP are treated as adiabatic fluctuations . Because ULAP suppresses the small scale structure, the matter power spectrum is also suppressed on scales smaller than ULAP Jeans scale k_J. Because the sound speed of ULAP is $c_s \simeq k/(ma)$ [140, 141], the Jeans scale at the matter-radiation equality $a_{\text{eq}} \sim 1/3400$ is estimated as

$$k_J \sim \frac{\sqrt{\rho_{\text{eq}}}}{c_s M_{\text{Pl}}} a_{\text{eq}} \sim \frac{H_{\text{eq}}}{k_J} m a_{\text{eq}}^2, \qquad (6.1.3)$$
$$\Leftrightarrow \quad k_J \sim \left(m H_{\text{eq}} a_{\text{eq}}^2\right)^{1/2} = \left(m H_m a_m^2\right)^{1/2} = m a_m. \qquad (6.1.4)$$

where the lower index m shows the onset of the oscillation of ULAP $H_m \simeq m$ and we have used the relation $a \propto t^{1/2} \propto H^{-1/2}$. Then,

$$H_m^2 \sim \frac{\rho_m}{M_{\text{Pl}}^2} \left(\frac{1}{a_{\text{eq}}}\right)^3 \left(\frac{a_{\text{eq}}}{a_m}\right)^4 = H_0^2 \Omega_m \frac{a_{\text{eq}}}{a_m^4}, \qquad (6.1.5)$$
$$\Leftrightarrow \quad a_m \sim \left(\frac{H_0^2 \Omega_m a_{\text{eq}}}{H_m^2}\right)^{1/4} = \left(\frac{H_0^2 \Omega_m a_{\text{eq}}}{m^2}\right)^{1/4}. \qquad (6.1.6)$$

$$\therefore \quad k_J \sim \left(m^2 H_0^2 \Omega_m a_{\text{eq}}\right)^{1/4} \sim 7 \left(\frac{m}{10^{-22}\text{ eV}}\right)^{1/2} h\text{Mpc}^{-1}. \qquad (6.1.7)$$

The results of the calculation of $P_{\text{CDM}} + P_{\text{coh}}$ at $z = 10$ is shown in Fig. 6.1.1. As we can find from these figures, the matter power spectrum is suppressed from the derived Jeans scale Eq. (6.1.7) compared to the ΛCDM result $P_{\text{CDM}} + P_{\text{homo}} < P_{\Lambda\text{CDM}}$, which generally reduces the number of 21cm absorption. The mass dependence of the suppression scale, that is, Jeans scale, can be easily confirmed from the left figure. On the other hand, when the ULAP mass is fixed with, for example, $m = 10^{-22}$ eV, the suppression gets more effective as f_{ULAP} gets larger.

In the following subsections, we calculate the power spectrum of oscillons to be added to $P_{\text{CDM}} + P_{\text{coh}}$ including two extra effects: the partial decay of produced oscillons and the gravitational growth of the isocurvature fluctuations.

6.1.1 Oscillon Decay

First, let us consider the decay process of the produced oscillons. As we discussed in Sec. 2.3, the oscillon distribution evolves because oscillons are getting smaller by emitting the self-radiation.
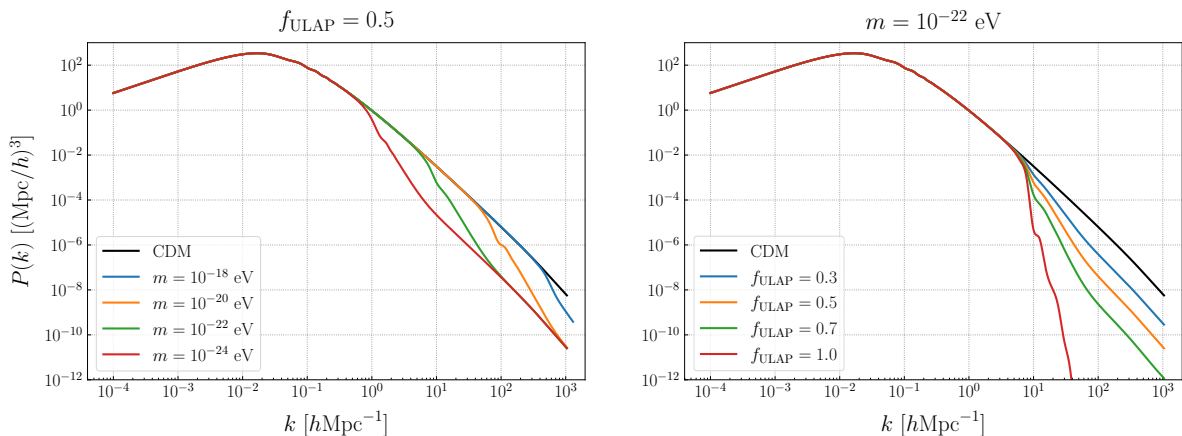
Figure 6.1.1: The matter power spectrum of ULAP at $z = 10$ when all ULAP is coherently oscillating. The left figure shows the case of the fixed ULAP fraction $f_{\mathrm{ULAP}} = 0.5$ and the right does that of the fixed ULAP mass $m = 10^{-22}$ eV for instance.

Following the calculation in Sec. 2.3, we analytically derive the oscillon decay rate Γ as in Fig. 6.1.2. In this calculation, we only consider Γ_3 in Eq. (2.3.24), which roughly means that we expand the potential up to the fourth-order of ϕ/F. As we mentioned in Sec. 2.3, poles, where the decay rate is extremely small, could be compensated by the higher-order terms, such as $\Gamma_5, \Gamma_7, \cdots$, and so on. Thus, we should consider p only whose poles hardly affect the evolution of the oscillon distribution. Therefore, to exclude the effect of small decay rate at the poles we use $p = -3/4$ hereafter whose smallest decay rate is smaller than that of poles for instance.

Using this decay rate, we can evolve the oscillon distribution from the formation time. The simulation result and the evolved distributions are shown in Fig 6.1.3. The simulation setup is shown in Sec. 5.2. Because of the poles around $\omega \simeq 0.78$, the energy distribution is split into two peaks, but this does not affect the calculation of the oscillon power spectrum much.

6.1.2 Gravitational Growth

The second is the growth of the fluctuations in the radiation and matter dominated era. In the parameter region of ULAP mass $m \gtrsim 10^{-28}$ eV where we are interested, oscillons are produced in the radiation dominated era. The fluctuations linearly grow after the matter-radiation equality and the oscillon power spectrum in the matter dominated era ($t > t_{\mathrm{eq}}$) is

$$P_{\mathrm{osc}}(k, t) = \left(\frac{3}{2}\frac{a}{a_{\mathrm{eq}}}\right)^2 P_{\mathrm{osc}}\left(k, t_{\mathrm{form}}\right), \tag{6.1.8}$$

where $P_{\mathrm{osc}}\left(k, t_{\mathrm{form}}\right)$ is the oscillon power spectrum around oscillon formation calculated from Eq. (5.1.37) and the simulations and $a_{\mathrm{eq}} \simeq 1/3400$ is the scale factor at the matter-radiation equality.

Considering these two effects, the oscillon matter power spectrum at $z = 10$ is calculated as shown in Fig. 6.1.4. In the figure, we also take into account the non-linearity of
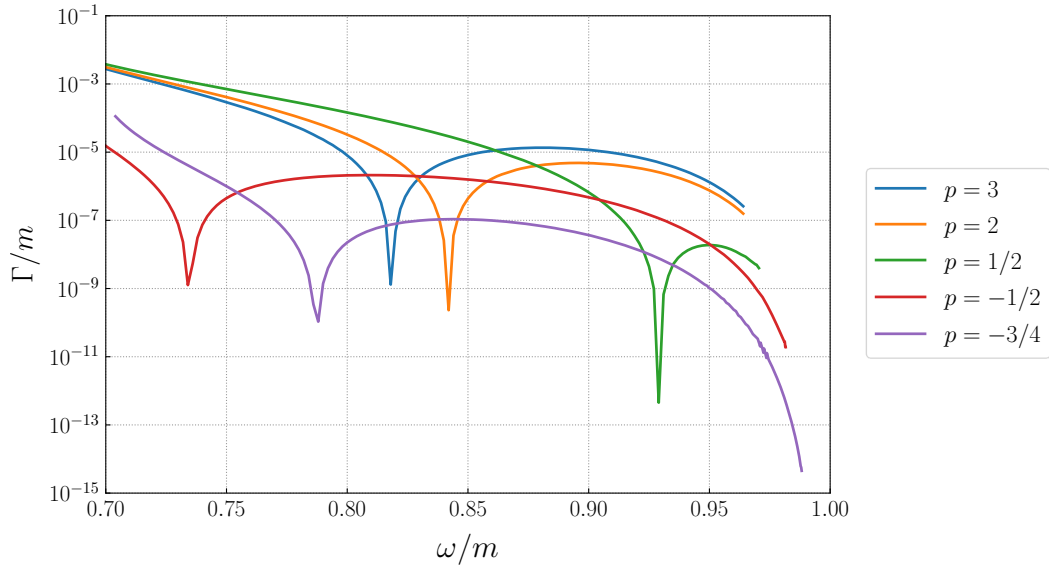
Figure 6.1.2: The decay rate of oscillons for various p's. The vertical axis shows the decay rate of oscillons and the horizontal axis shows the oscillation frequency of the scalar field inside the oscillon. The upper limit of ω is determined by the oscillon coniditon Eq. (2.2.14).
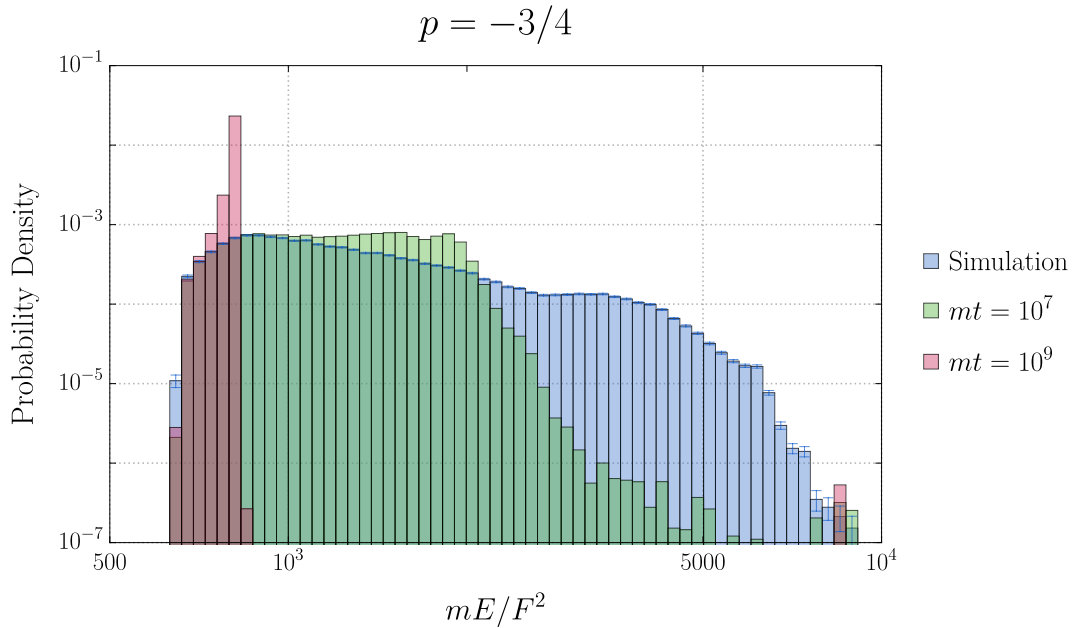
$$p = -3/4$$

Figure 6.1.3: The probability density of the oscillon mass distribution derived from the lattice simulation which contains $\sim 10^5$ oscillons. The blue region shows the oscillon distribution at the formation time, and the green and red regions show the distribution at $mt = 10^7$ and $mt = 10^9$, respectively. The width of the i-th bin is $\Delta b_i \equiv 10^{14/5} \left(10^{(i+1)/50} - 10^{i/50} \right)$ and statistical error of the simulation result is given by $\sqrt{N_i}/(N_{\text{osc}} \Delta b_i)$ where N_i is the number of data in the i-th bin and N_{osc} is the total number of data.
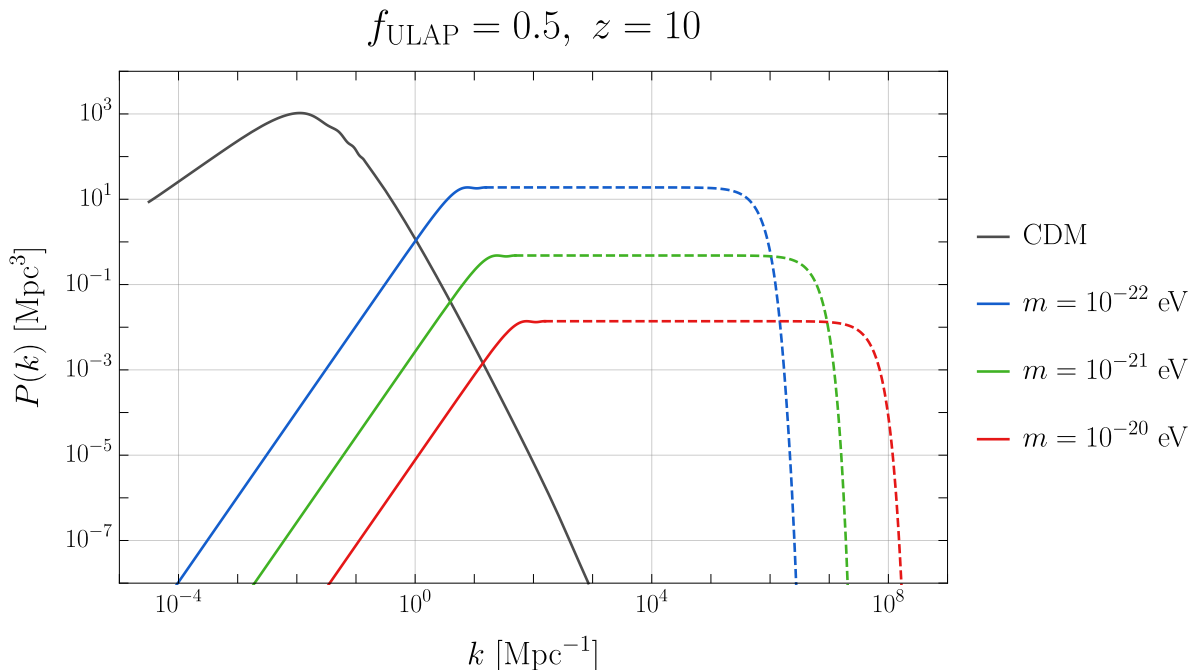
Figure 6.1.4: The matter power spectrum of oscillons when $f_{\mathrm{ULAP}} = 0.5$ at $z = 10$. The blue, green, and red lines show the oscillon matter power spectrum of $m = 10^{-22}$ eV, $m = 10^{-21}$ eV, and $m = 10^{-20}$ eV respectively. We truncated the matter power spectrum at the point where the oscillon number equals to 10 because the fluctuation of a single oscillon is non-linear. These regions are plotted as dashed lines. Note that the exponential cutoff on the right side of the figure $k/a \sim m$ is because of the radius of a oscillon. We also plotted the matter power spectrum of ΛCDM model as the black line for comparison.

the energy density of oscillons. The linear matter power spectrum must be truncated at least below the scale where the oscillon number is smaller than 2 because the fluctuation is non-linear in that scale. Thus, we cut off the power spectrum on the scale k_{cut} where the number of oscillons equals to 10 as $n_{\mathrm{osc}}(2\pi/k_{\mathrm{cut}})^3 = 10$, for instance. These lines are shown as dotted lines in Fig. 6.1.4.

6.2 Halo Mass Function

From the power spectrum we derived in the previous section, we can calculate the number of mini-halos that affects the abundance of 21cm absorption lines. In this chapter, we use the Press-Schechter formalism [142] to calculate the halo-mass function. Although the Sheth-Tormen mass function [143] is more precise in a low redshift, the situation is currently unclear for $z \sim 10$. Thus, we use the Press-Schechter formalism in this chapter and briefly review it below.

First, we define the coarse-grained fluctuation as

$$\delta_{\mathrm{cg}}(\boldsymbol{x}, R) \equiv \int d^3 x \delta(\boldsymbol{x}) W(\boldsymbol{x}, R), \qquad (6.2.1)$$
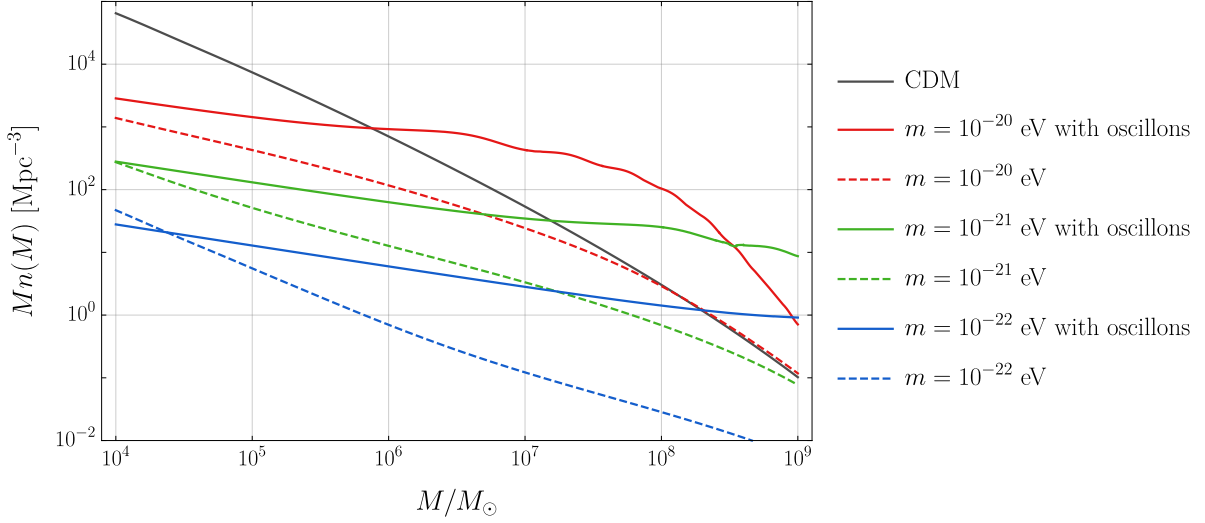
54

Figure 6.2.1: The halo-mass function when $f_{\mathrm{ULAP}} = 0.5$. The red, green, and blue lines show the result of $m = 10^{-20}$ eV, $m = 10^{-21}$ eV, and $m = 10^{-22}$ eV. The solid and dashed lines show the halo mass function with ULAP oscillons and without ULAP oscillon respectively. We also plotted the halo-mass function of ΛCDM model as the black line for comparison.

where $\boldsymbol{x}$ is the comoving coordinate and R is the comoving coarse-grained scale. We use the real space top-hat function as the window function $W(\boldsymbol{x}, R)$ described as

$$W(\boldsymbol{x}, R) = \frac{3}{4\pi R^3} \Theta\left(R - |\boldsymbol{x}|\right). \tag{6.2.2}$$

$$\therefore \quad W(\boldsymbol{k}, R) = \frac{3}{(kR)^3}\left(\sin kR - kR \cos kR\right) \tag{6.2.3}$$

Assuming that the energy density fraction follows the Gaussian distribution, the probability that we can find the over-dense region where $\delta_{\mathrm{cg}} > \delta_c \simeq 1.686$ in the linear perturbation theory is

$$P(> \delta_c) = \frac{1}{\sqrt{2\pi}\sigma(R)} \int_{\delta_c}^{\infty} \exp\left(-\frac{\delta_{\mathrm{cg}}^2}{2\sigma(R)^2}\right) d\delta_{cg}, \tag{6.2.4}$$

where $\sigma(R)$ is the coarse-grained variance where

$$\sigma(R)^2 \equiv \langle \delta_{cg}^2(\boldsymbol{x}, R) \rangle = \int P(k) \left|W(kR)\right|^2 d^3k. \tag{6.2.5}$$

Because the coarse-grained comoving radius R is related to the halo mass M as

$$M = \frac{4\pi R^3}{3}\rho_{m0}, \tag{6.2.6}$$

we can take σ as the function of M instead of R. Then, the comoving number density of halos with the mass M is calculated from the Press-Schechter formalism as

$$n(M, z)dM = 2\frac{\rho_{m0}}{M}\frac{\partial P(> \delta_c)}{\partial M}dM, \qquad (6.2.7)$$

$$= \sqrt{\frac{2}{\pi}}\frac{\rho_{m0}}{M}\frac{\delta_c}{\sigma(M)^2}\exp\left(-\frac{\delta_c^2}{2\sigma(M)^2}\right)\left|\frac{\partial\sigma(M)}{\partial M}\right|dM. \qquad (6.2.8)$$

The calculation results are shown in Fig. 6.2.1. When ULAP without oscillons exists as dark matter, the number of halos is suppressed compared to the CDM case because of the quantum pressure of ULAP as shown in dashed lines. On the other hand, the solid lines which exhibit the halo-mass function with ULAP oscillons are always larger than the corresponding dashed lines, because of the amplification of the matter power spectrum by ULAP oscillons. They are even larger than that of the CDM case depending on the ULAP mass.

6.3 Halo Profile

6.3.1 Dark Matter Profile

The dark matter halo profile at the low redshift is well described by the Navarro, Frenk, and White (NFW) profile [144, 145], [1]

$$\rho_{DM}(r) = \frac{\rho_{DM0}}{r/r_s\left(1 + r/r_s\right)^2} \equiv \frac{\rho_{DM0}}{xy\left(1 + xy\right)^2}. \qquad (6.3.1)$$

where r_s is the scale parameter, x, y are defined as $x \equiv r/r_{\rm vir}$, $y \equiv r_{\rm vir}/r_s$, and $r_{\rm vir}$ is the virial radius. y is often called the concentration parameter and fitted in Ref. [146] [2] as

$$y = \frac{14.8}{1 + z}\left(\frac{M}{1.3 \times 10^{13}h^{-1}M_\odot}\right)^{-0.14}, \qquad (6.3.2)$$

where we set M as the virial mass, $M_\odot = 1.33 \times 10^{33}$ kg is the solar mass, and $h = 0.68$ is the normalized Hubble parameter here.

The virial radius $r_{\rm vir}$ is calculated by the spherical collapse model [148], which derives

$$r_{\rm vir} = \left(\frac{M}{\frac{4\pi}{3}\rho_m(z)\Delta}\right)^{1/3}, \qquad (6.3.3)$$

$$= 0.53 \text{ kpc} \left(\frac{M}{10^8 h^{-1}M_\odot}\right)^{1/3}\left(\frac{\Omega_{m0}}{\Omega_m}\frac{\Delta}{18\pi^2}\right)^{-1/3}\left(\frac{1 + z}{10}\right)^{-1}. \qquad (6.3.4)$$

where $\Delta \equiv 18\pi^2 + 82d - 39d^2$, and $d \equiv \Omega_m(z) - 1$. $\rho_m(z)$ is the matter energy density at the redshift z and $\Omega_m(z) = \rho_m(z)/\rho_c(z)$ where $\rho_c(z)$ is the critical energy density at the redshift z. From the above relations, the central energy density ρ_{DM0} is determined as

$$\rho_{DM0} = \frac{M}{\int_0^{r_{\rm vir}}\left[r/r_s\left(1 + r/r_s\right)^2\right]^{-1}d^3r}. \qquad (6.3.5)$$

---

[1]We will discuss the validity of the NFW profile later in Sec. 6.5

[2]This fitting contains large uncertainty. See also [147, 145]

6.3.2 Gas Profile

For simplicity, we make two assumptions on the gas within halos.

- Isothermal: The gas within halos is isothermal because it is virialized. Defining the virial temperature as $\langle K \rangle = (3/2)k_B T_{\text{vir}}$ where $\langle K \rangle$ is the time-averaged kinetic energy per particle of the system, the virial theorem leads to

$$T_{\text{vir}} = -\frac{\langle V_{tot} \rangle}{3k_B} \simeq \frac{\mu}{2k_B} \frac{GM}{r_{\text{vir}}}. \tag{6.3.6}$$

Here k_B is the Boltzmann constant and $\mu = 1.22 m_p$ is the mean molecular weight of the gas [51]. [3]

- In hydrostatic equilibrium: At the distance r from the origin, the gas pressure $P(r)$ and the gravitational force are balanced [149],

$$\frac{dP(r)}{dr} = -\frac{GM(r)}{r^2}\rho_g(r), \tag{6.3.7}$$

where $\rho_g(r)$ shows the gas profile. The gas pressure is easily calculated from the equation of state as

$$P(r) = \frac{\rho_g(r)}{\mu}k_B T_{\text{vir}}. \tag{6.3.8}$$

From the above two assumptions, the gas profile $\rho_g(r)$ is

$$\rho_g(r) = \rho_{g0} \exp\left[-\frac{\mu}{2k_B T_{\text{vir}}} \left(v_{\text{esc}}(0)^2 - v_{\text{esc}}(r)^2 \right) \right], \tag{6.3.9}$$

where

$$v_{\text{esc}}(r)^2 = 2 \int_r^\infty \frac{GM(\tilde{r})}{\tilde{r}^2}d\tilde{r} = \frac{2GM}{r_{\text{vir}}} \frac{\log(1 + xy)}{x\left[\log(1 + y) - \frac{y}{1+y}\right]}. \tag{6.3.10}$$

The normalization of the gas profile ρ_{g0} is determined by the ratio of the baryon energy density Ω_b and matter energy density Ω_m as

$$\frac{M_g}{M} = \frac{\Omega_b}{\Omega_m}, \quad \Leftrightarrow \quad \rho_{g0} = \frac{\Delta}{3} \frac{y^3 e^A}{\int_0^y (1+t)^{A/t} t^2 dt} \frac{\Omega_b}{\Omega_m} \rho_m(z), \tag{6.3.11}$$

where

$$A \equiv \frac{3y}{\log(1 + y) - y/(1 + y)}. \tag{6.3.12}$$

From all above calculations, the number density profile of the neutral hydrogen is derived as

$$n_{HI}(r) = 0.74 \times \frac{\rho_g(r)}{m_p}, \tag{6.3.13}$$

where we assume that the all hydrogen is not ionized and completely neutral.

---

[3]We ignore the $\mathcal{O}(1)$ coefficient of the gravitational potential.

6.4　Absorption Abundance

Finally, let us derive the depending on the optical depth τ. From Eq. (4.1.10), defining the total number density in the two-level system as

$$n_{\rm tot} = n_0 + n_1 = n_0 \left(1 + \frac{n_1}{n_0} \right) \simeq \left(1 + \frac{g_1}{g_0} \right) n_0, \tag{6.4.1}$$

the optical depth defined by $\tau \equiv \alpha_\nu ct$ is calculated as

$$\tau(\nu; \boldsymbol{n}) \equiv \int \alpha_\nu cdt = \left(1 + \frac{g_0}{g_1} \right)^{-1} \frac{hc^2 A_{10}}{8\pi k_B \nu_{10}} \int \frac{n_{\rm tot}(\boldsymbol{x}, t)}{T_s(\boldsymbol{x}, t)} \phi(\nu) d(ct), \tag{6.4.2}$$

where the integration is taken along the direction of photons. Thus, the optical depth of a mini-halo is obtained by the integration of the absorption coefficient over the entire distance as

$$\tau(\nu, M, \alpha) = \frac{3hc^2 A_{10}}{32\pi k_B \nu_{10}} \int_{-R_{max}}^{R_{max}} \frac{n_{HI}(r)}{T_S(r)} \phi(\nu) dR, \tag{6.4.3}$$

where α is the impact parameter, h is Planck constant, $\nu_{10} = 1420$ MHz, c is the speed of light, $R = \sqrt{r^2 - \alpha^2}$ is the coordinate along the line of sight, and

$$\phi(\nu) = \frac{c}{\sqrt{\pi}b} \exp \left[-\frac{c^2 \left(\nu^2/\nu_{10}^2 - 1 \right)}{b^2} \right], \quad \left(b \equiv \frac{2k_B T_{\rm vir}}{m_p} \right) \tag{6.4.4}$$

is the line profile function. Here we only consider the Doppler broadening effect due to the thermal dispersion of the neutral hydrogen.

From the above relations, we can derive the number of systems intersected with the optical depth greater than τ per redshift interval as

$$\frac{dN(> \tau)}{dz} = (1 + z)^2 \frac{dr}{dz} \int_{M_{\rm min}}^{M_{\rm max}} n(M, z) \pi \alpha(\tau)^2 dM, \tag{6.4.5}$$

where $dr/dz = c/H(z)$ is the comoving line element and $\alpha(\tau)$ shows the maximum physical radius where the optical depth exceeds τ. As the halo mass function, we will use the matter power spectrum derived in Sec. 6.1.

The upper and lower bounds of the integration have a great effect on the abundance. The minimum mass of the minihalo $M_{\rm min}$ should be determined by the Jeans scale of IGM, which leads to

$$M_{\rm min} = \frac{4\pi \rho_m(z)}{3} \left(\frac{5\pi k_B T_{\rm IGM}}{3G\mu\rho_m(z)} \right)^{3/2} \simeq 3.58 \times 10^5 h^{-1} M_\odot \left(\frac{T_{\rm IGM}/K}{1 + z} \right)^{3/2}. \tag{6.4.6}$$

where $T_{\rm IGM}$ is the IGM temperature. The IGM temperature around $z \sim 10$ is still unclear because of the uncertainties of the astrophysics. In this paper, we choose $T_{\rm IGM} =$

10 K, 100 K which avoid recent constraints on T_{IGM} [150, 151]. [4]

The maximum mass M_{max} is determined by the condition

$$T_{\mathrm{vir}}(M) \lesssim 10^4 \ \mathrm{K}. \tag{6.4.7}$$

Below this temperature, the star formation becomes inefficient because of the weakness of the metal-free gas cooling [143, 153]. The corresponding mini-halo mass is about $3 \times 10^7 M_{\odot}$.

The result of the calculation is shown in Fig. 6.4.1. All dashed lines (ALP without oscillons) are smaller than the CDM case because the number of mini-halos is suppressed by homogeneous ULAP as mentioned in Sec. 6.1. On the other hand, the solid lines (ALP with oscillons) are larger than the dashed lines due to the enhanced number of mini-halos with $10^6 M_{\odot} \lesssim M \lesssim 10^7 M_{\odot}$. Because the number of intersections is smaller than 1 when $m \lesssim 10^{-21}\mathrm{eV}$ even for ULAP oscillons with $T_{\mathrm{IGM}} = 10$ K, it could be difficult to observe the difference of the 21cm absorption lines in this range. The range becomes smaller when the IGM temperature is larger as shown in the lower figure of Fig. 6.4.1, but this result still contains various uncertainties in T_{IGM} and the mini-halo profile. Thus, we should wait for observational and theoretical progress for more precise estimation.

6.5 Discussion

6.5.1 Detectable Parameter Regions

To constrain the ULAP parameters from the difference of the optical depth, we need to perform Fisher analysis. However, because the above calculation also includes the uncertainties of the IGM temperature and the halo profile discussed in the next subsection, we instead plotted the parameter region of ULAP that is essentially detectable by 21cm forest in Fig. 6.5.1, considering the following conditions.

- ULAP abundance: Because the energy density of ULAP is in proportional to a^{-3} like the matter, we can determine the total energy density of ULAP from the relation

$$\rho_{\mathrm{ULAP}}(t) = \frac{1}{2} m^2 F^2 \left(\frac{\phi(t_{\mathrm{end}})}{F} \right)^2 \left(\frac{a(t_{\mathrm{end}})}{a(t)} \right)^3, \tag{6.5.1}$$

where the parameters with the simulation end time t_{end} are evaluated by the lattice simulation. Thus, we can constrain the ULAP parameters by requiring $f_{\mathrm{ULAP}} < 1$, which excludes the blue region in Fig. 6.5.1. Note that this constraint would be changed depending on the initial value of the ULAP. It would be stricter when the

---

[4]The IGM temperature must be at least larger than the adiabatic temperature of the matter component. Because the matter temperature decreases adiabatically $\propto a^{-2}$ after the decoupling from the radiation via the Compton scattering around $z \simeq 150$ [152] without other heating, the adiabatic temperature is estimated as

$$T_{\mathrm{ad}} \simeq \frac{2.73}{1 + 150}(1 + z)^2 \simeq 1.8 \times 10^{-2}(1 + z)^2 \ \mathrm{K},$$

which is also excluded by recent observations around $z \sim 10$ [150, 151].

initial amplitude becomes larger than our simulation value $\phi_i/F = 12\pi$, and vice versa.

- Oscillon lifetime: The produced oscillons must live up to the observation time ($z = 10$ in this paper) because the density fluctuation may be smeared out after the oscillon decay due to the self-radiation. This constraint for $p = -3/4$ is shown as the red region in Fig. 6.5.1.

- Observations of matter power spectrum: The matter power spectrum on the large scale $k \lesssim \mathcal{O}(1)$ Mpc^{-1} is precisely determined by many observations, such as Planck [6], DES [5], and SDSS [154, 155]. Thus, we constrain the ULAP parameters by the condition $P_{\mathrm{osc}}(1/\mathrm{Mpc}) > P_{\Lambda\mathrm{CDM}}(1/\mathrm{Mpc})$ as the green region in Fig. 6.5.1. We did not include the Lyman-α constraint discussed in Refs. [124, 125] here because it is not obvious whether the produced oscillons affect the result of their simulations.

- The amplitude of the oscillon matter power spectrum: To detect the difference between the ULAP oscillon and the ordinary ΛCDM, the amplitude of the oscillon matter power spectrum must be at least larger than that of ΛCDM model. Thus, the region $P_{\mathrm{osc}}(k_{\mathrm{cut}}) < P_{\Lambda\mathrm{CDM}}(k_{\mathrm{cut}})$ is conservatively excluded where k_{cut} is the cut-off wavenumber mentioned in Sec. 6.1. This constraint is shown as the orange region in Fig. 6.5.1 and we find that ULAP is detectable if $f_{\mathrm{ULAP}} \gg 10^{-2}$.

6.5.2 Mini-halo Profile

When $p = -3/4$, the average oscillon energy at $z = 10$ is determined from Eq. (5.2.3) and the simulation result as

$$\langle E \rangle \sim 6 \times 10^6 M_\odot \left(\frac{F}{10^{15}\ \mathrm{GeV}} \right)^2 \left(\frac{10^{-22}\ \mathrm{eV}}{m} \right). \tag{6.5.2}$$

while the interested mini-halo mass range is $10^6 M_\odot \lesssim M \lesssim 10^7 M_\odot$. The contours of the constant oscillon mass $10^6 M_\odot$ and $10^7 M_\odot$ are plotted in Fig. 6.5.1 as black dotted lines. Between these lines, the NFW profile may not describe the internal structure of the mini-halo well because the mini-halo mass is almost the same as the produced oscillon mass. In this case, the mini-halo profile becomes more centered by oscillons, which results in more absorption abundance near the mini-halo center. However, it is unclear whether oscillons are disrupted by the gravitational force in the matter dominated era. Thus, we used the NFW profile here and we will work on the gravitational stability of oscillons in future work.

6.5.3 Number of Bright Sources

Finally, we briefly comment on the existence of observable radio-loud sources in $z \gtrsim 10$ by the next generation observatory, Square Kilometer Array (SKA). Using Eq. (4.1.15) with $\tau \ll 1$, the flux density difference by the absorption is represented by τF with F

being the flux density of the background source. To observe the absorption line with the signal-to-noise ratio $S/N = 5$, the minimum necessary background flux density is calculated as [49, 137]

$$F = 10.4 \text{ mJy} \left(\frac{0.01}{\tau}\right) \left(\frac{S/N}{5}\right) \left(\frac{1 \text{ kHz}}{\Delta\nu}\right)^{1/2} \left(\frac{5000 \text{ m}^2/K}{A_{\text{eff}}/T_{\text{sys}}}\right) \left(\frac{100 \text{ hr}}{t_{\text{obs}}}\right)^{1/2}, \quad (6.5.3)$$

where τ is the target 21cm optical depth, $\Delta\nu$ is the frequency resolution, $A_{\text{eff}}/T_{\text{sys}}$ is the ratio of the effective area to the system temperature, and t_{obs} is the observation time. [5] Recently, the radio loud sources around $z \sim 6$ with a flux $\gtrsim \mathcal{O}(10)$ mJy have been confirmed [156, 157] and a simple estimation indicates $10^4 \sim 10^5$ quasars around $z \simeq 10$ in the whole sky per redshift interval [158, 55, 56]. Besides, Population (Pop) III stars have been proposed to produce GRBs [159, 160, 161, 162], which could be unique sources in the high-redshift universe. These possibilities support the importance of studies on the 21cm forest.

---

[5]Note that the frequency resolution of SKA $\Delta\nu_{\text{SKA}} \simeq 1$ kHz is much larger than the width of the absorption lines due to the thermal broadening

$$\frac{\Delta\nu_{\text{thermal}}(z)}{\nu_{10}(z)} \simeq 1.3 \times 10^{-5} \left(\frac{T_{\text{vir}}}{10^3 \text{ K}}\right) < \frac{\Delta\nu_{\text{SKA}}}{\nu_{10}(z)} \simeq 7.0 \times 10^{-7}(1+z).$$
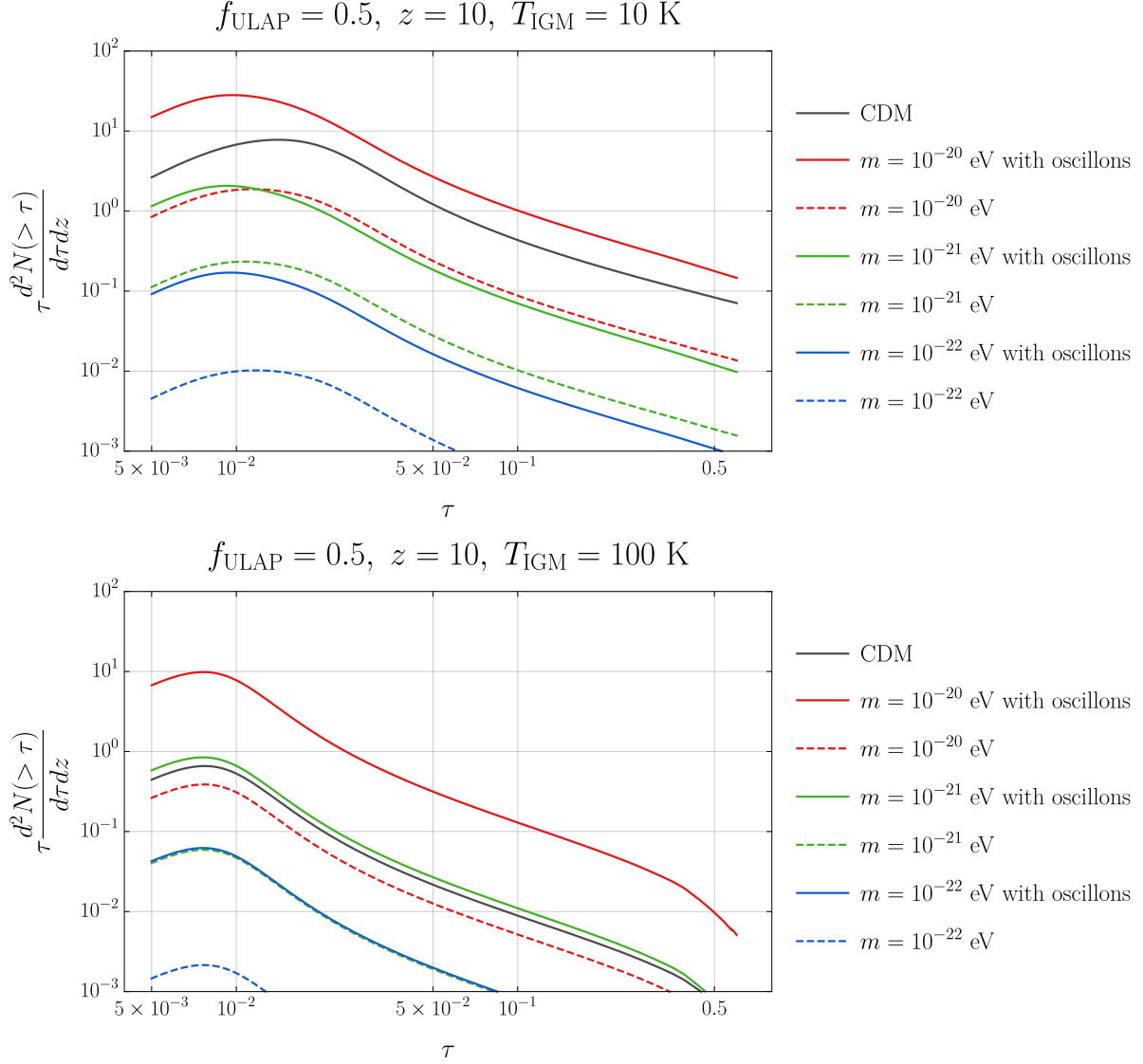
Figure 6.4.1: The adundance of 21cm absorbers. The upper and lower figures show the case of $T_{\text{IGM}} = 10$ K, 100 K respectively. The horizontal axis shows the optical depth and the vertical axis does abundance of the number of systems intersected with the optical depth τ per redshift interval. The red, green, and blue lines show the result of $m = 10^{-20}$ eV, $m = 10^{-21}$ eV, and $m = 10^{-22}$ eV. and the solid and dashed lines show the halo mass function with ULAP oscillons and without ULAP oscillon respectively. We also plotted the result of ΛCDM model as the black line for comparison.
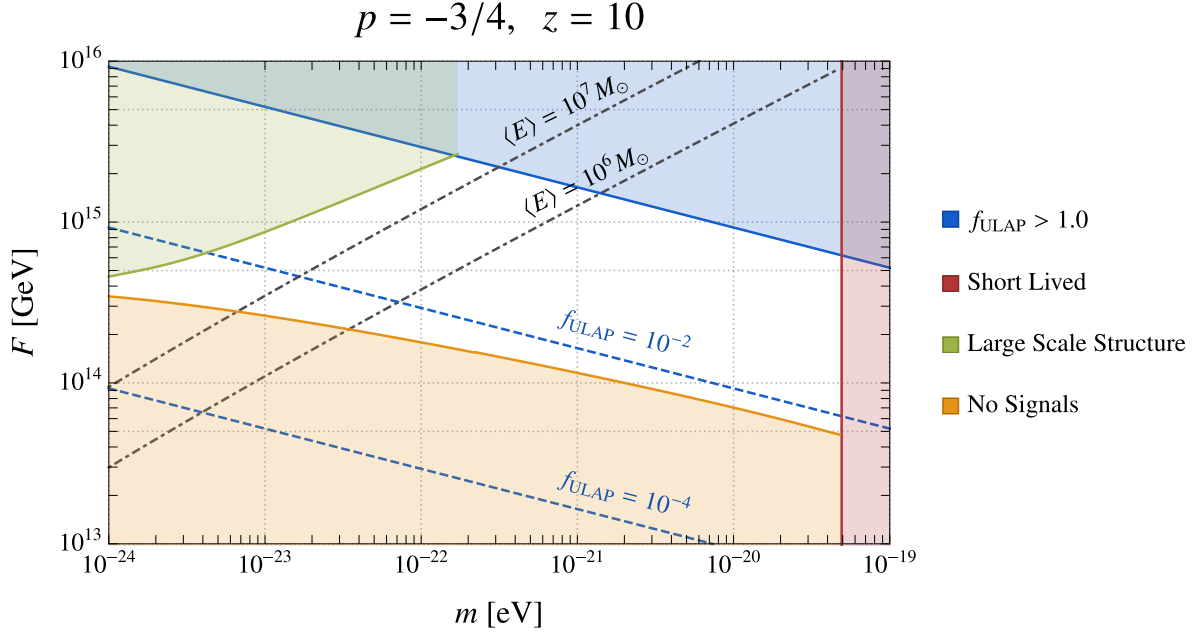
Figure 6.5.1: The detectable parameter region by 21cm forest with ULAP oscillons. The horizontal and vertical axis show the ULAP mass and the ULAP decay constant, respectively. The blue region is excluded because the ULAP abundance f_{ULAP} is larger than 1 when the initial amplitude of ULAP is $\phi_i/F = 12\pi$. The red region shows the case that the lifetime of produced oscillons for $p = -3/4$ is smaller than the cosmic time at $z = 10$. The green region is excluded by the condition $P_{\text{osc}}(1/\text{Mpc}) > P_{\Lambda\text{CDM}}(1/\text{Mpc})$ because the matter power spectrum on the large scale $\lesssim \mathcal{O}(1)$ Mpc^{-1} is constrained by observations. The orange region is excluded by $P_{\text{osc}}(k_{\text{cut}}) < P_{\Lambda\text{CDM}}(k_{\text{cut}})$ where k_{cut} is the cut-off wavenumber determined by the number of oscillons as mentioned in Sec. 6.1.

Chapter 7

Conclusions

In this thesis, we have studied the formation and evolution of ULAP oscillons and suggested a possibility to detect ULAP oscillons by 21cm line.

In Part I, we briefly reviewed the basics of oscillons, ULAP, and 21cm line necessary for the following discussion.

In Part II, we have calculated the power spectrum of oscillons both analytically and numerically and derived their cosmological implications by the 21cm forest.

In Chap. 5, we have analytically derived the oscillon power spectrum for the first time and confirmed that the formula coincides with the simulations. We have found that the oscillon power spectrum is well described by the plateau of Poisson distribution cut by two effects: the energy conservation inside the horizon $\propto k^2$ on small scales and the exponential cutoff due to the oscillon size on large scales. We used a monodromy type potential for instance, but the analytical formula derived in this section is applicable to any local objects that are produced inside the horizon.

In Chap. 6. we have focused on the 21cm forest for the ULAP detection and calculated the number of intersections with mini-halos partially consist of ULAP oscillons. We found that the number of intersections could be affected when the ULAP mass is $m \lesssim 10^{-19}$ eV and the ULAP fraction is $f_{\text{ULAP}} \gg 10^{-2}$ where the matter power spectrum can be changed. Unlike the previous researches, because the Poisson-like power spectrum is cut off by the energy conservation on large scales, we can focus on the phenomenologically interesting region $m \sim 10^{-22}$ eV in this case. Besides, because the oscillons produce large fluctuations, ULAP can be detectable even if f_{ULAP} is smaller than 1. The method used in this thesis is also applicable to all ULAP models which produce long-lived oscillons.

Before closing this thesis we should mention the interaction between other fields. In this thesis, we only considered the self-interactions, but of course, ULAP could have an interaction with other fields, such as the electromagnetic field. In this case, because the decay rate becomes larger, the lifetime of oscillons could become much smaller. If oscillons emit the relativistic ULAP when they completely decay, the relativistic ULAP smears out the small structure like warm dark matter, which may give us another constraint on ULAP to consider. Such possibilities would be investigated in future work.

Acknowledgements

Bibliography

[1] K. Begeman, A. Broeils and R. Sanders, *Extended rotation curves of spiral galaxies: Dark haloes and modified dynamics*, Mon. Not. Roy. Astron. Soc. **249** (1991) 523.

[2] M. Mateo, *Dwarf galaxies of the Local Group*, Ann. Rev. Astron. Astrophys. **36** (1998) 435–506 [`arXiv:astro-ph/9810070`].

[3] L. Koopmans and T. Treu, *The structure and dynamics of luminous and dark matter in the early-type lens galaxy of 0047-281 at z=0.485*, Astrophys. J. **583** (2003) 606–615 [`arXiv:astro-ph/0205281`].

[4] **WMAP** Collaboration, G. Hinshaw *et. al.*, *Nine-Year Wilkinson Microwave Anisotropy Probe (WMAP) Observations: Cosmological Parameter Results*, Astrophys. J. Suppl. **208** (2013) 19 [`arXiv:1212.5226`].

[5] **DES** Collaboration, T. Abbott *et. al.*, *Dark Energy Survey year 1 results: Cosmological constraints from galaxy clustering and weak lensing*, Phys. Rev. D **98** (2018), no. 4 043526 [`arXiv:1708.01530`].

[6] **Planck** Collaboration, N. Aghanim *et. al.*, *Planck 2018 results. VI. Cosmological parameters*, `arXiv:1807.06209`.

[7] B. Moore, S. Ghigna, F. Governato, G. Lake, T. R. Quinn, J. Stadel and P. Tozzi, *Dark matter substructure within galactic halos*, Astrophys. J. Lett. **524** (1999) L19–L22 [`arXiv:astro-ph/9907411`].

[8] W. de Blok, *The Core-Cusp Problem*, Adv. Astron. **2010** (2010) 789293 [`arXiv:0910.3538`].

[9] M. Boylan-Kolchin, J. S. Bullock and M. Kaplinghat, *The Milky Way's bright satellites as an apparent failure of ΛCDM*, Mon. Not. Roy. Astron. Soc. **422** (2012) 1203–1218 [`arXiv:1111.2048`].

[10] P. Svrcek and E. Witten, *Axions In String Theory*, JHEP **06** (2006) 051 [`arXiv:hep-th/0605206`].

[11] A. Arvanitaki, S. Dimopoulos, S. Dubovsky, N. Kaloper and J. March-Russell, *String Axiverse*, Phys. Rev. D **81** (2010) 123530 [`arXiv:0905.4720`].

[12] W. Hu, R. Barkana and A. Gruzinov, *Cold and fuzzy dark matter*, *Phys. Rev. Lett.* **85** (2000) 1158–1161 [arXiv:astro-ph/0003365].

[13] H.-Y. Schive, M.-H. Liao, T.-P. Woo, S.-K. Wong, T. Chiueh, T. Broadhurst and W.-Y. P. Hwang, *Understanding the Core-Halo Relation of Quantum Wave Dark Matter from 3D Simulations*, *Phys. Rev. Lett.* **113** (2014), no. 26 261302 [arXiv:1407.7762].

[14] H.-Y. Schive, T. Chiueh and T. Broadhurst, *Cosmic Structure as the Quantum Interference of a Coherent Dark Wave*, *Nature Phys.* **10** (2014) 496–499 [arXiv:1406.6586].

[15] J. Veltmaat, J. C. Niemeyer and B. Schwabe, *Formation and structure of ultralight bosonic dark matter halos*, *Phys. Rev. D* **98** (2018), no. 4 043509 [arXiv:1804.09647].

[16] L. Hui, J. P. Ostriker, S. Tremaine and E. Witten, *Ultralight scalars as cosmological dark matter*, *Phys. Rev. D* **95** (2017), no. 4 043541 [arXiv:1610.08297].

[17] I. L. Bogolyubsky and V. G. Makhankov, *Lifetime of Pulsating Solitons in Some Classical Models*, *Pisma Zh. Eksp. Teor. Fiz.* **24** (1976) 15–18.

[18] M. Gleiser, *Pseudostable bubbles*, *Phys. Rev.* **D49** (1994) 2978–2981 [arXiv:hep-ph/9308279].

[19] E. J. Copeland, M. Gleiser and H. R. Muller, *Oscillons: Resonant configurations during bubble collapse*, *Phys. Rev.* **D52** (1995) 1920–1933 [arXiv:hep-ph/9503217].

[20] S. Weinberg, *A New Light Boson?*, *Phys. Rev. Lett.* **40** (1978) 223–226.

[21] F. Wilczek, *Problem of Strong p and t Invariance in the Presence of Instantons*, *Phys. Rev. Lett.* **40** (1978) 279–282.

[22] J. E. Kim, *Weak Interaction Singlet and Strong CP Invariance*, *Phys. Rev. Lett.* **43** (1979) 103.

[23] M. A. Shifman, A. I. Vainshtein and V. I. Zakharov, *Can Confinement Ensure Natural CP Invariance of Strong Interactions?*, *Nucl. Phys.* **B166** (1980) 493–506.

[24] M. Dine, W. Fischler and M. Srednicki, *A Simple Solution to the Strong CP Problem with a Harmless Axion*, *Phys. Lett.* **104B** (1981) 199–202.

[25] E. W. Kolb and I. I. Tkachev, *Nonlinear axion dynamics and formation of cosmological pseudosolitons*, *Phys. Rev. D* **49** (1994) 5040–5051 [arXiv:astro-ph/9311037].

[26] E. W. Kolb and I. I. Tkachev, *Axion miniclusters and Bose stars*, *Phys. Rev. Lett.* **71** (1993) 3051–3054 [`arXiv:hep-ph/9303313`].

[27] L. McAllister, E. Silverstein and A. Westphal, *Gravity Waves and Linear Inflation from Axion Monodromy*, *Phys. Rev.* **D82** (2010) 046003 [`arXiv:0808.0706`].

[28] E. Silverstein and A. Westphal, *Monodromy in the CMB: Gravity Waves and String Inflation*, *Phys. Rev.* **D78** (2008) 106003 [`arXiv:0803.3085`].

[29] X. Dong, B. Horn, E. Silverstein and A. Westphal, *Simple exercises to flatten your potential*, *Phys. Rev. D* **84** (2011) 026011 [`arXiv:1011.4521`].

[30] S. Dubovsky, A. Lawrence and M. M. Roberts, *Axion monodromy in a model of holographic gluodynamics*, *JHEP* **02** (2012) 053 [`arXiv:1105.3740`].

[31] R. Kallosh and A. Linde, *Universality Class in Conformal Inflation*, *JCAP* **07** (2013) 002 [`arXiv:1306.5220`].

[32] R. Kallosh, A. Linde and D. Roest, *Universal Attractor for Inflation at Strong Coupling*, *Phys. Rev. Lett.* **112** (2014), no. 1 011303 [`arXiv:1310.3950`].

[33] R. Kallosh, A. Linde and D. Roest, *Superconformal Inflationary α-Attractors*, *JHEP* **11** (2013) 198 [`arXiv:1311.0472`].

[34] Y. Nomura, T. Watari and M. Yamazaki, *Pure Natural Inflation*, *Phys. Lett. B* **776** (2018) 227–230 [`arXiv:1706.08522`].

[35] S. Kasuya, M. Kawasaki and F. Takahashi, *I-balls*, *Phys. Lett.* **B559** (2003) 99–106 [`arXiv:hep-ph/0209358`].

[36] M. Kawasaki, F. Takahashi and N. Takeda, *Adiabatic Invariance of Oscillons/I-balls*, *Phys. Rev.* **D92** (2015), no. 10 105024 [`arXiv:1508.01028`].

[37] M. Ibe, M. Kawasaki, W. Nakano and E. Sonomoto, *Fragileness of Exact I-ball/Oscillon*, *Phys. Rev. D* **100** (2020), no. 12 125021 [`arXiv:1908.11103`].

[38] M. Ibe, M. Kawasaki, W. Nakano and E. Sonomoto, *Decay of I-ball/Oscillon in Classical Field Theory*, *JHEP* **04** (2019) 030 [`arXiv:1901.06130`].

[39] H.-Y. Zhang, M. A. Amin, E. J. Copeland, P. M. Saffin and K. D. Lozanov, *Classical Decay Rates of Oscillons*, *JCAP* **07** (2020) 055 [`arXiv:2004.01202`].

[40] B. Piette and W. J. Zakrzewski, *Metastable stationary solutions of the radial d-dimensional sine-Gordon model*, *Nonlinearity* **11** (1998) 1103–1110.

[41] J. Ollé, O. Pujolàs and F. Rompineve, *Oscillons and Dark Matter*, *JCAP* **02** (2020) 006 [`arXiv:1906.06352`].

[42] M. Kawasaki, W. Nakano and E. Sonomoto, *Oscillon of Ultra-Light Axion-like Particle*, *JCAP* **01** (2020) 047 [`arXiv:1909.10805`].

[43] J. Soda and Y. Urakawa, *Cosmological imprints of string axions in plateau, Eur. Phys. J. C* **78** (2018), no. 9 779 [`arXiv:1710.00305`].

[44] N. Kitajima, J. Soda and Y. Urakawa, *Gravitational wave forest from string axiverse, JCAP* **10** (2018) 008 [`arXiv:1807.07037`].

[45] Y. Shtanov, J. H. Traschen and R. H. Brandenberger, *Universe reheating after inflation, Phys. Rev.* **D51** (1995) 5438–5455 [`arXiv:hep-ph/9407247`].

[46] L. Kofman, A. D. Linde and A. A. Starobinsky, *Nonthermal phase transitions after inflation, Phys. Rev. Lett.* **76** (1996) 1011–1014 [`arXiv:hep-th/9510119`].

[47] L. Kofman, A. D. Linde and A. A. Starobinsky, *Towards the theory of reheating after inflation, Phys. Rev.* **D56** (1997) 3258–3295 [`arXiv:hep-ph/9704452`].

[48] P. Madau, A. Meiksin and M. J. Rees, *21-CM tomography of the intergalactic medium at high redshift, Astrophys. J.* **475** (1997) 429 [`arXiv:astro-ph/9608010`].

[49] C. Carilli, N. Y. Gnedin and F. Owen, *Hi 21cm absorption beyond the epoch of re-ionization, Astrophys. J.* **577** (2002) 22–30 [`arXiv:astro-ph/0205169`].

[50] S. Furlanetto and A. Loeb, *The 21 cm forest: Radio absorption spectra as a probe of the intergalactic medium before reionization, Astrophys. J.* **579** (2002) 1–9 [`arXiv:astro-ph/0206308`].

[51] R. Barkana and A. Loeb, *In the beginning: The First sources of light and the reionization of the Universe, Phys. Rept.* **349** (2001) 125–238 [`arXiv:astro-ph/0010468`].

[52] M. A. Amin, R. Easther, H. Finkel, R. Flauger and M. P. Hertzberg, *Oscillons After Inflation, Phys. Rev. Lett.* **108** (2012) 241302 [`arXiv:1106.3335`].

[53] M. A. Amin, R. Easther and H. Finkel, *Inflaton Fragmentation and Oscillon Formation in Three Dimensions, JCAP* **12** (2010) 001 [`arXiv:1009.2505`].

[54] M. A. Amin and P. Mocz, *Formation, gravitational clustering, and interactions of nonrelativistic solitons in an expanding universe, Phys. Rev. D* **100** (2019), no. 6 063507 [`arXiv:1902.07261`].

[55] H. Shimabukuro, K. Ichiki and K. Kadota, *Constraining the nature of ultra light dark matter particles with the 21 cm forest, Phys. Rev. D* **101** (2020), no. 4 043516 [`arXiv:1910.06011`].

[56] H. Shimabukuro, K. Ichiki and K. Kadota, *21 cm forest probes on axion dark matter in postinflationary Peccei-Quinn symmetry breaking scenarios, Phys. Rev. D* **102** (2020), no. 2 023522 [`arXiv:2005.05589`].

[57] J.-P. Hong, M. Kawasaki and M. Yamazaki, *Oscillons from Pure Natural Inflation, Phys. Rev.* **D98** (2018), no. 4 043531 [`arXiv:1711.10496`].

[58] M. Kawasaki, W. Nakano, H. Nakatsuka and E. Sonomoto, *Oscillons of Axion-Like Particle: Mass distribution and power spectrum*, `arXiv:2010.09311`.

[59] M. Kawasaki, W. Nakano, H. Nakatsuka and E. Sonomoto, *Probing Oscillons of Ultra-Light Axion-like Particle by 21cm Forest*, `arXiv:2010.13504`.

[60] L. D. Landau and E. M. Lifshitz, *Mechanics, Third Edition: Volume 1 (Course of Theoretical Physics).* Butterworth-Heinemann, 3 ed., Jan., 1976.

[61] N. G. Vakhitov and A. A. Kolokolov, *Stationary Solutions of the Wave Equation in a Medium with Nonlinearity Saturation, Radiophysics and Quantum Electronics* **16** (July, 1973) 783–789.

[62] T. Lee and Y. Pang, *Nontopological solitons, Phys. Rept.* **221** (1992) 251–350.

[63] E. Y. Nugaev and A. Shkerin, *Review of Nontopological Solitons in Theories with U(1)-Symmetry, J. Exp. Theor. Phys.* **130** (2020), no. 2 301–320 [`arXiv:1905.05146`].

[64] K. Mukaida, M. Takimoto and M. Yamada, *On Longevity of I-ball/Oscillon*, *JHEP* **03** (2017) 122 [`arXiv:1612.07750`].

[65] J. Eby, K. Mukaida, M. Takimoto, L. Wijewardhana and M. Yamada, *Classical nonrelativistic effective field theory and the role of gravitational interactions*, *Phys. Rev. D* **99** (2019), no. 12 123503 [`arXiv:1807.09795`].

[66] R. D. Peccei and H. R. Quinn, *CP Conservation in the Presence of Instantons*, *Phys. Rev. Lett.* **38** (1977) 1440–1443.

[67] R. D. Peccei and H. R. Quinn, *Constraints Imposed by CP Conservation in the Presence of Instantons, Phys. Rev.* **D16** (1977) 1791–1797.

[68] J. M. Pendlebury *et. al.*, *Revised experimental upper limit on the electric dipole moment of the neutron, Phys. Rev.* **D92** (2015), no. 9 092003 [`arXiv:1509.04411`].

[69] B. Graner, Y. Chen, E. G. Lindahl and B. R. Heckel, *Reduced limit on the permanent electric dipole moment of* ^{199}Hg, *Phys. Rev. Lett.* **116** (Apr, 2016) 161601.

[70] C. Vafa and E. Witten, *Parity Conservation in QCD, Phys. Rev. Lett.* **53** (1984) 535.

[71] G. 't Hooft, *Computation of the Quantum Effects Due to a Four-Dimensional Pseudoparticle, Phys. Rev. D* **14** (1976) 3432–3450. [Erratum: Phys.Rev.D 18, 2199 (1978)].

[72] A. Burrows, M. S. Turner and R. P. Brinkmann, *Axions and SN 1987a, Phys. Rev.* **D39** (1989) 1020.

[73] J. Engel, D. Seckel and A. C. Hayes, *Emission and detectability of hadronic axions from SN1987A*, *Phys. Rev. Lett.* **65** (1990) 960–963.

[74] A. Burrows, M. T. Ressell and M. S. Turner, *Axions and SN1987A: Axion trapping*, *Phys. Rev.* **D42** (1990) 3297–3309.

[75] P. Sikivie, *Of Axions, Domain Walls and the Early Universe*, *Phys. Rev. Lett.* **48** (1982) 1156–1159.

[76] J. Preskill, M. B. Wise and F. Wilczek, *Cosmology of the Invisible Axion*, *Phys. Lett. B* **120** (1983) 127–132.

[77] L. Abbott and P. Sikivie, *A Cosmological Bound on the Invisible Axion*, *Phys. Lett. B* **120** (1983) 133–136.

[78] M. Dine and W. Fischler, *The Not So Harmless Axion*, *Phys. Lett. B* **120** (1983) 137–141.

[79] T. Hiramatsu, M. Kawasaki, K. Saikawa and T. Sekiguchi, *Production of dark matter axions from collapse of string-wall systems*, *Phys. Rev. D* **85** (2012) 105020 [arXiv:1202.5851]. [Erratum: Phys.Rev.D 86, 089902 (2012)].

[80] J. S. Bullock and M. Boylan-Kolchin, *Small-Scale Challenges to the ΛCDM Paradigm*, *Ann. Rev. Astron. Astrophys.* **55** (2017) 343–387 [arXiv:1707.04256].

[81] A. A. Klypin, A. V. Kravtsov, O. Valenzuela and F. Prada, *Where are the missing Galactic satellites?*, *Astrophys. J.* **522** (1999) 82–92 [arXiv:astro-ph/9901240].

[82] V. Springel, J. Wang, M. Vogelsberger, A. Ludlow, A. Jenkins, A. Helmi, J. F. Navarro, C. S. Frenk and S. D. White, *The Aquarius Project: the subhalos of galactic halos*, *Mon. Not. Roy. Astron. Soc.* **391** (2008) 1685–1711 [arXiv:0809.0898].

[83] M. Kuhlen, P. Madau and J. Silk, *Exploring dark matter with milky way substructure*, *Science* **325** (2009), no. 5943 970–973 [arXiv:https://science.sciencemag.org/content/325/5943/970.full.pdf].

[84] J. Stadel, D. Potter, B. Moore, J. Diemand, P. Madau, M. Zemp, M. Kuhlen and V. Quilis, *Quantifying the heart of darkness with GHALO - a multi-billion particle simulation of our galactic halo*, *Mon. Not. Roy. Astron. Soc.* **398** (2009) L21–L25 [arXiv:0808.2981].

[85] S. Garrison-Kimmel, M. Boylan-Kolchin, J. Bullock and K. Lee, *ELVIS: Exploring the Local Volume in Simulations*, *Mon. Not. Roy. Astron. Soc.* **438** (2014), no. 3 2578–2596 [arXiv:1310.6746].

[86] B. F. Griffen, A. P. Ji, G. A. Dooley, F. A. Gómez, M. Vogelsberger, B. W. O'Shea and A. Frebel, *THE CATERPILLAR PROJECT: A LARGE SUITE OF MILKY WAY SIZED HALOS*, *The Astrophysical Journal* **818** (feb, 2016) 10.

[87] **DES** Collaboration, A. Drlica-Wagner *et. al.*, *Eight Ultra-faint Galaxy Candidates Discovered in Year Two of the Dark Energy Survey*, *Astrophys. J.* **813** (2015), no. 2 109 [`arXiv:1508.03622`].

[88] S. E. Koposov, V. Belokurov, G. Torrealba and N. W. Evans, *Beasts of the Southern Wild: Discovery of nine Ultra Faint satellites in the vicinity of the Magellanic Clouds*, *Astrophys. J.* **805** (2015), no. 2 130 [`arXiv:1503.02079`].

[89] D. Homma, M. Chiba, S. Okamoto, Y. Komiyama, M. Tanaka, M. Tanaka, M. N. Ishigaki, M. Akiyama, N. Arimoto, J. A. Garmilla, R. H. Lupton, M. A. Strauss, H. Furusawa, S. Miyazaki, H. Murayama, A. J. Nishizawa, M. Takada, T. Usuda and S.-Y. Wang, *A NEW MILKY WAY SATELLITE DISCOVERED IN THE SUBARU/HYPER SUPRIME-CAM SURVEY*, *The Astrophysical Journal* **832** (nov, 2016) 21.

[90] J. F. Navarro, C. S. Frenk and S. D. M. White, *A universal density profile from hierarchical clustering*, *The Astrophysical Journal* **490** (dec, 1997) 493–508.

[91] T. Fukushige and J. Makino, *On the Origin of Cusps in Dark Matter Halos*, *Astrophys. J.* **477** (1997) L9 [`arXiv:astro-ph/9610005`].

[92] J. F. Navarro, A. Ludlow, V. Springel, J. Wang, M. Vogelsberger, S. D. White, A. Jenkins, C. S. Frenk and A. Helmi, *The Diversity and Similarity of Cold Dark Matter Halos*, *Mon. Not. Roy. Astron. Soc.* **402** (2010) 21 [`arXiv:0810.1522`].

[93] W. de Blok, F. Walter, E. Brinks, C. Trachternach, S.-H. Oh and J. Kennicutt, R.C., *High-Resolution Rotation Curves and Galaxy Mass Models from THINGS*, *Astron. J.* **136** (2008) 2648–2719 [`arXiv:0810.2100`].

[94] R. Kuzio de Naray, S. S. McGaugh and W. de Blok, *Mass Models for Low Surface Brightness Galaxies with High Resolution Optical Velocity Fields*, *Astrophys. J.* **676** (2008) 920–943 [`arXiv:0712.0860`].

[95] S.-H. Oh, W. de Blok, F. Walter, E. Brinks and J. Kennicutt, Robert C., *High-resolution dark matter density profiles of THINGS dwarf galaxies: Correcting for non-circular motions*, *Astron. J.* **136** (2008) 2761 [`arXiv:0810.2119`].

[96] M. Boylan-Kolchin, J. S. Bullock and M. Kaplinghat, *Too big to fail? The puzzling darkness of massive Milky Way subhaloes*, *Mon. Not. Roy. Astron. Soc.* **415** (2011) L40 [`arXiv:1103.0007`].

[97] E. J. Tollerud, M. Boylan-Kolchin and J. S. Bullock, *M31 Satellite Masses Compared to LCDM Subhaloes*, *Mon. Not. Roy. Astron. Soc.* **440** (2014), no. 4 3511–3519 [`arXiv:1403.6469`].

[98] E. N. Kirby, J. S. Bullock, M. Boylan-Kolchin, M. Kaplinghat and J. G. Cohen, *The dynamics of isolated Local Group galaxies*, *Mon. Not. Roy. Astron. Soc.* **439** (2014), no. 1 1015–1027 [`arXiv:1401.1208`].

[99] S.-H. Oh *et. al.*, *High-resolution mass models of dwarf galaxies from LITTLE THINGS*, Astron. J. **149** (2015) 180 [`arXiv:1502.01281`].

[100] A. Burkert, *The Structure of dark matter halos in dwarf galaxies*, IAU Symp. **171** (1996) 175 [`arXiv:astro-ph/9504041`].

[101] J. F. Navarro, V. R. Eke and C. S. Frenk, *The cores of dwarf galaxy halos*, Mon. Not. Roy. Astron. Soc. **283** (1996) L72–L78 [`arXiv:astro-ph/9610187`].

[102] O. Y. Gnedin and H. Zhao, *Maximum feedback and dark matter profiles of dwarf galaxies*, Mon. Not. Roy. Astron. Soc. **333** (2002) 299 [`arXiv:astro-ph/0108108`].

[103] F. Governato, A. Zolotov, A. Pontzen, C. Christensen, S. H. Oh, A. M. Brooks, T. Quinn, S. Shen and J. Wadsley, *Cuspy no more: how outflows affect the central dark matter and baryon distribution in Λ cold dark matter galaxies*, Mon. Not. Roy. Astron. Soc. **422** (May, 2012) 1231–1240 [`arXiv:1202.0554`].

[104] A. Di Cintio, C. B. Brook, A. V. Macciò, G. S. Stinson, A. Knebe, A. A. Dutton and J. Wadsley, *The dependence of dark matter profiles on the stellar-to-halo mass ratio: a prediction for cusps versus cores*, Mon. Not. Roy. Astron. Soc. **437** (2014), no. 1 415–423 [`arXiv:1306.0898`].

[105] A. Zolotov, A. M. Brooks, B. Willman, F. Governato, A. Pontzen, C. Christensen, A. Dekel, T. Quinn, S. Shen and J. Wadsley, *Baryons Matter: Why Luminous Satellite Galaxies have Reduced Central Masses*, The Astrophysical Journal **761** (Dec., 2012) 71 [`arXiv:1207.0007`].

[106] K. S. Arraki, A. Klypin, S. More and S. Trujillo-Gomez, *Effects of baryon removal on the structure of dwarf spheroidal galaxies*, Mon. Not. Roy. Astron. Soc. **438** (Feb., 2014) 1466–1482 [`arXiv:1212.6651`].

[107] A. M. Brooks and A. Zolotov, *Why Baryons Matter: The Kinematics of Dwarf Spheroidal Satellites*, The Astrophysical Journal **786** (May, 2014) 87 [`arXiv:1207.2468`].

[108] T. Sawala *et. al.*, *The APOSTLE simulations: solutions to the Local Group's cosmic puzzles*, Mon. Not. Roy. Astron. Soc. **457** (2016), no. 2 1931–1943 [`arXiv:1511.01098`].

[109] J. Read, O. Agertz and M. Collins, *Dark matter cores all the way down*, Mon. Not. Roy. Astron. Soc. **459** (2016), no. 3 2573–2590 [`arXiv:1508.04143`].

[110] E. Tollet, A. V. Macciò, A. A. Dutton, G. S. Stinson, L. Wang, C. Penzo, T. A. Gutcke, T. Buck, X. Kang, C. Brook, A. Di Cintio, B. W. Keller and J. Wadsley, *NIHAO - IV: core creation and destruction in dark matter density profiles across cosmic time*, Mon. Not. Roy. Astron. Soc. **456** (Mar., 2016) 3542–3552 [`arXiv:1507.03590`].

[111] A. Fitts *et. al.*, *FIRE in the Field: Simulating the Threshold of Galaxy Formation*, Mon. Not. Roy. Astron. Soc. **471** (2017), no. 3 3547–3562 [`arXiv:1611.02281`].

[112] P. F. Hopkins *et. al.*, *FIRE-2 Simulations: Physics versus Numerics in Galaxy Formation*, Mon. Not. Roy. Astron. Soc. **480** (2018), no. 1 800–863 [`arXiv:1702.06148`].

[113] J. Goodman, *Repulsive dark matter*, New Astron. **5** (2000) 103 [`arXiv:astro-ph/0003018`].

[114] P. Peebles, *Fluid dark matter*, Astrophys. J. Lett. **534** (2000) L127 [`arXiv:astro-ph/0002495`].

[115] L. Amendola and R. Barbieri, *Dark matter from an ultra-light pseudo-Goldsone-boson*, Phys. Lett. B **642** (2006) 192–196 [`arXiv:hep-ph/0509257`].

[116] E. Braaten, A. Mohapatra and H. Zhang, *Dense Axion Stars*, Phys. Rev. Lett. **117** (2016), no. 12 121801 [`arXiv:1512.00108`].

[117] L. Visinelli, S. Baum, J. Redondo, K. Freese and F. Wilczek, *Dilute and dense axion stars*, Phys. Lett. B **777** (2018) 64–72 [`arXiv:1710.08910`].

[118] D. J. E. Marsh and J. Silk, *A Model For Halo Formation With Axion Mixed Dark Matter*, Mon. Not. Roy. Astron. Soc. **437** (2014), no. 3 2652–2663 [`arXiv:1307.1705`].

[119] A. X. González-Morales, D. J. Marsh, J. Peñarrubia and L. A. Ureña López, *Unbiased constraints on ultralight axion mass from dwarf spheroidal galaxies*, Mon. Not. Roy. Astron. Soc. **472** (2017), no. 2 1346–1360 [`arXiv:1609.05856`].

[120] V. Lora and J. Magaña, *Is Sextans dwarf galaxy in a scalar field dark matter halo?*, Journal of Cosmology and Astroparticle Physics **2014** (Sept., 2014) 011 [`arXiv:1406.6875`].

[121] T. Bernal, L. M. Fernández-Hernández, T. Matos and M. A. Rodríguez-Meza, *Rotation curves of high-resolution LSB and SPARC galaxies with fuzzy and multistate (ultralight boson) scalar field dark matter*, Mon. Not. Roy. Astron. Soc. **475** (Apr., 2018) 1447–1468 [`arXiv:1701.00912`].

[122] K. Hayashi and I. Obata, *Non-sphericity of ultralight axion dark matter haloes in the Galactic dwarf spheroidal galaxies*, Mon. Not. Roy. Astron. Soc. **491** (2020), no. 1 615–633 [`arXiv:1902.03054`].

[123] R. Hlozek, D. Grin, D. J. E. Marsh and P. G. Ferreira, *A search for ultralight axions using precision cosmological data*, Phys. Rev. D **91** (2015), no. 10 103512 [`arXiv:1410.2896`].

[124] V. Iršič, M. Viel, M. G. Haehnelt, J. S. Bolton and G. D. Becker, *First constraints on fuzzy dark matter from Lyman-α forest data and hydrodynamical simulations*, *Phys. Rev. Lett.* **119** (2017), no. 3 031302 [`arXiv:1703.04683`].

[125] T. Kobayashi, R. Murgia, A. De Simone, V. Iršič and M. Viel, *Lyman-α constraints on ultralight scalar dark matter: Implications for the early and late universe*, *Phys. Rev. D* **96** (2017), no. 12 123514 [`arXiv:1708.00015`].

[126] B. Bozek, D. J. Marsh, J. Silk and R. F. Wyse, *Galaxy UV-luminosity function and reionization constraints on axion dark matter*, *Mon. Not. Roy. Astron. Soc.* **450** (2015), no. 1 209–222 [`arXiv:1409.3544`].

[127] N. C. Amorisco and A. Loeb, *First constraints on Fuzzy Dark Matter from the dynamics of stellar streams in the Milky Way*, `arXiv:1808.00464`.

[128] R. Penrose, *Gravitational collapse: The role of general relativity*, *Riv. Nuovo Cim.* **1** (1969) 252–276.

[129] A. Arvanitaki and S. Dubovsky, *Exploring the String Axiverse with Precision Black Hole Physics*, *Phys. Rev. D* **83** (2011) 044026 [`arXiv:1004.3558`].

[130] A. Arvanitaki, M. Baryakhtar and X. Huang, *Discovering the QCD Axion with Black Holes and Gravitational Waves*, *Phys. Rev. D* **91** (2015), no. 8 084011 [`arXiv:1411.2263`].

[131] A. Arvanitaki, M. Baryakhtar, S. Dimopoulos, S. Dubovsky and R. Lasenby, *Black Hole Mergers and the QCD Axion at Advanced LIGO*, *Phys. Rev. D* **95** (2017), no. 4 043001 [`arXiv:1604.03958`].

[132] R. Brito, V. Cardoso and P. Pani, *Superradiance: New Frontiers in Black Hole Physics*, vol. 906. Springer, 2015.

[133] G. B. Field, *Excitation of the hydrogen 21-cm line*, *Proceedings of the IRE* **46** (1958), no. 1 240–250.

[134] S. Furlanetto and S. J. Stoever, *Secondary ionization and heating by fast electrons*, *Mon. Not. Roy. Astron. Soc.* **404** (2010) 1869 [`arXiv:0910.4410`].

[135] S. A. Wouthuysen, *On the excitation mechanism of the 21-cm (radio-frequency) interstellar hydrogen emission line.*, *Astron. J.* **57** (Jan., 1952) 31–32.

[136] G. B. Field, *Excitation of the Hydrogen 21-CM Line*, *Proceedings of the IRE* **46** (Jan., 1958) 240–250.

[137] S. Furlanetto, *The 21 Centimeter Forest*, *Mon. Not. Roy. Astron. Soc.* **370** (2006) 1867–1875 [`arXiv:astro-ph/0604223`].

[138] A. Lewis, A. Challinor and A. Lasenby, *Efficient computation of CMB anisotropies in closed FRW models*, *Astrophys. J.* **538** (2000) 473–476 [`arXiv:astro-ph/9911177`].

[139] C. Howlett, A. Lewis, A. Hall and A. Challinor, *Cmb power spectrum parameter degeneracies in the era of precision cosmology*, Journal of Cosmology and Astroparticle Physics **2012** (2012), no. 04 027.

[140] J.-c. Hwang and H. Noh, *Axion as a Cold Dark Matter candidate*, Phys. Lett. B **680** (2009) 1–3 [arXiv:0902.4738].

[141] C.-G. Park, J.-c. Hwang and H. Noh, *Axion as a cold dark matter candidate: Low-mass case*, Physical Review D **86** (Oct, 2012).

[142] W. H. Press and P. Schechter, *Formation of galaxies and clusters of galaxies by selfsimilar gravitational condensation*, Astrophys. J. **187** (1974) 425–438.

[143] R. K. Sheth and G. Tormen, *Large scale bias and the peak background split*, Mon. Not. Roy. Astron. Soc. **308** (1999) 119 [arXiv:astro-ph/9901122].

[144] J. F. Navarro, C. S. Frenk and S. D. White, *A Universal density profile from hierarchical clustering*, Astrophys. J. **490** (1997) 493–508 [arXiv:astro-ph/9611107].

[145] J. F. Hennawi, N. Dalal, P. Bode and J. P. Ostriker, *Characterizing the cluster lens population*, Astrophys. J. **654** (2007) 714–730 [arXiv:astro-ph/0506171].

[146] J. M. Comerford and P. Natarajan, *The Observed Concentration-Mass Relation for Galaxy Clusters*, Mon. Not. Roy. Astron. Soc. **379** (2007) 190–200 [arXiv:astro-ph/0703126].

[147] J. S. Bullock, T. S. Kolatt, Y. Sigad, R. S. Somerville, A. V. Kravtsov, A. A. Klypin, J. R. Primack and A. Dekel, *Profiles of dark haloes. Evolution, scatter, and environment*, Mon. Not. Roy. Astron. Soc. **321** (2001) 559–575 [arXiv:astro-ph/9908159].

[148] A. Cooray and R. K. Sheth, *Halo Models of Large Scale Structure*, Phys. Rept. **372** (2002) 1–129 [arXiv:astro-ph/0206508].

[149] N. Makino, S. Sasaki and Y. Suto, *X-ray gas density profile of clusters of galaxies from the universal dark matter halo*, Astrophys. J. **497** (1998) 555 [arXiv:astro-ph/9710344].

[150] B. Greig *et. al.*, *Interpreting LOFAR 21-cm signal upper limits at z~9.1 in the context of high-z galaxy and reionisation observations*, arXiv:2006.03203.

[151] B. Greig, C. M. Trott, N. Barry, S. J. Mutch, B. Pindor, R. L. Webster and J. S. B. Wyithe, *Exploring reionisation and high-z galaxy observables with recent multi-redshift MWA upper limits on the 21-cm signal*, arXiv:2008.02639.

[152] P. Madau and M. Kuhlen, *The dawn of galaxies*, in *Multiwavelength Mapping of Galaxy Evolution*, ESO Astrophysics Symposia European Southern Observatory, pp. 1–11, 2005. arXiv:astro-ph/0303584.

[153] I. T. Iliev, P. R. Shapiro, A. Ferrara and H. Martel, *On the direct detectability of the cosmic dark ages: 21-cm emission from minihalos, Astrophys. J.* **572** (2002) 123 [`arXiv:astro-ph/0202410`].

[154] B. M. R. *et. al.*, *Sloan Digital Sky Survey IV: Mapping the Milky Way, Nearby Galaxies, and the Distant Universe, The Astronomical Journal* **154** (July, 2017) 28 [`arXiv:1703.00052`].

[155] B. Abolfathi *et. al.*, *The fourteenth data release of the sloan digital sky survey: First spectroscopic data from the extended baryon oscillation spectroscopic survey and from the second phase of the apache point observatory galactic evolution experiment, The Astrophysical Journal Supplement Series* **235** (Apr., 2018) 42 [`arXiv:1707.09322`].

[156] E. Bañados, C. Carilli, F. Walter, E. Momjian, R. Decarli, E. P. Farina, C. Mazzucchelli and B. P. Venemans, *A powerful radio-loud quasar at the end of cosmic reionization, The Astrophysical Journal* **861** (Jul, 2018) L14.

[157] S. Belladitta *et. al.*, *The first blazar observed at z > 6, Astron. Astrophys.* **635** (2020) L7 [`arXiv:2002.05178`].

[158] Y. Xu, X. Chen, Z. Fan, H. Trac and R. Cen, *THE 21 cm FOREST AS a PROBE OF THE REIONIZATION AND THE TEMPERATURE OF THE INTERGALACTIC MEDIUM, The Astrophysical Journal* **704** (oct, 2009) 1396–1404.

[159] S. S. Komissarov and M. V. Barkov, *Supercollapsars and their X-ray bursts, Monthly Notices of the Royal Astronomical Society: Letters* **402** (02, 2010) L25–L29 [`arXiv:https://academic.oup.com/mnrasl/article-pdf/402/1/L25/4894965/402-1-L25.pdf`].

[160] K. Toma, T. Sakamoto and a. Mészáros, *Population iii gamma-ray burst afterglows: Constraints on stellar masses and external medium densities, The Astrophysical Journal* **731** (04, 2011) 127.

[161] P. Meszaros and M. Rees, *Population III Gamma Ray Bursts, Astrophys. J.* **715** (2010) 967–971 [`arXiv:1004.2056`].

[162] Y. Suwa and K. Ioka, *Can Gamma-Ray Burst Jets Break Out the First Stars?, Astrophys. J.* **726** (2011) 107 [`arXiv:1009.6001`].

[163] H. Yoshida, *Construction of higher order symplectic integrators, Physics Letters A* **150** (1990), no. 5 262 – 268.

Appendix A

Einstein Coefficients

In a two-level system, there are three processes that we should take into consideration; spontaneous emission, absorption, and stimulated emission. The intuitive picture of these processes is shown in Fig. A.0.1. Let us consider them in order and derive the Einstein relation to be used in the following section.

The first is spontaneous emission. Generally, the higher state decays to the lower state as emitting photons. When we define Einstein A coefficient as A_{10}, which represents how many photons are spontaneously emitted from the higher state per second per unit volume, the rate of change of n_1 is written by

$$\dot{n}_1 = -A_{10}n_1, \tag{A.0.1}$$

where the dot represents the time derivative.

The second and third processes are absorption and stimulated emission. In the absorption process, the lower state is excited to the higher one by the absorption of radiated photons. This process is described by Einstein B coefficient $B_{01}(\nu)$, which represents the same meaning as A_{10} when multiplied by the energy density per frequency of radiated photons $\rho(\nu)$. In the stimulated emission process, photons are emitted from the higher state by radiated photons and the Einstein coefficient is given by $B_{10}(\nu)$. Then, the rate of change by these processes is written as

$$\dot{n}_0 = -B_{01}(\nu)\rho(\nu)n_0, \quad \dot{n}_1 = -B_{10}(\nu)\rho(\nu)n_1. \tag{A.0.2}$$
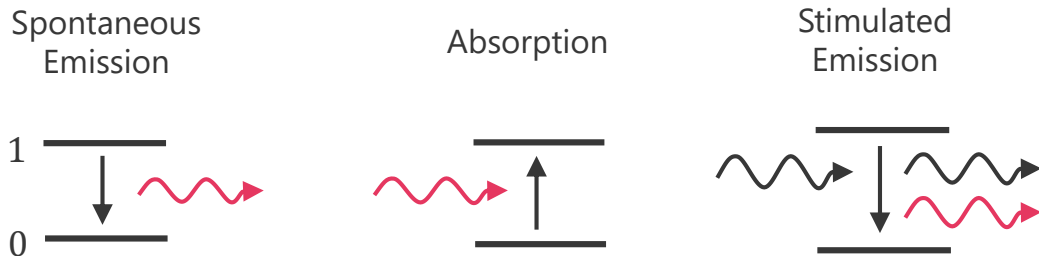

Figure A.0.1: The three processes in a two-level system.

When these three processes are in equilibrium, the rate of change becomes zero and

$$0 = \dot{n}_0 = -\dot{n}_1 = [A_{10} + B_{10}(\nu)\rho(\nu)]\, n_1 - B_{01}(\nu)\rho(\nu)n_0. \tag{A.0.3}$$

$$\therefore \quad \rho(\nu) = \frac{A_{21}n_2}{B_{12}n_1 - B_{21}n_2} = \frac{A_{12}/B_{12}}{n_1 B_{12}/(n_2 B_{21}) - 1}. \tag{A.0.4}$$

When the radiated photons follow the Planck's law, $\rho(\nu)$ is written as

$$\rho(\nu) = \frac{8\pi h\nu^3}{c^3} \frac{1}{\exp\left(\frac{h\nu}{k_B T}\right) - 1}. \tag{A.0.5}$$

On the other hand, because in an equilibrium system particles obey Boltzmann distribution $n = g\exp\left(-h\nu/k_B T\right)$ with g and T being degrees of freedom and the temperature of n, we can derive the Einstein relation as

$$\frac{A_{10}}{B_{10}(\nu)} = \frac{8\pi h\nu^3}{c^3}, \quad \frac{g_0 B_{01}(\nu)}{g_1 B_{10}(\nu)} = 1, \tag{A.0.6}$$

where g_0, g_1 are the degrees of freedom of n_0, n_1.

Appendix B

Classical Lattice Simulation

In this section, we briefly explain the basics of the classical lattice simulation we use in Part II. To derive the generalized formula, we will consider both in physical and conformal time and D dimensional space. Then, the FRW metric is represented by

$$g_{\mu\nu} = a^{2A} d\tau^2 - a^2 \sum_{i=1}^{D} dx_i^2. \quad (A = 0 - 1, \ D = 1 - 3) \tag{B.0.1}$$

In the following explanation, we use a dash $'$ to denote the derivative of physical time when $A = 0$ and conformal time when $A = 1$.

We simplify the explanation by only considering a single scalar field with Lagrangian

$$\mathcal{L} = \frac{1}{2} g^{\mu\nu} \partial_\mu \phi \partial_\nu \phi - V(\phi), \tag{B.0.2}$$

but the application to multi-scalar fields or complex scalar fields is fairly straightforward.

B.1   Time Evolution

First, we discuss the time evolution scheme of the simulation because it deeply relates to the formulation of equations of motion. We use the symplectic integration scheme for the time evolution because it exactly conserves the Hamiltonian of the system. In this section, we show the simple derivation of the symplectic integration scheme in the second-order, often called "leapfrog" method, and its application result in the fourth-order.

Because equations of motion are second-order differential equations, let us consider a second-order differential equation simplified as

$$\frac{d^2\phi}{dt^2} = f[\phi(t)]. \tag{B.1.1}$$

In the leapfrog method, we regard it as series of first-order differential equations as

$$\frac{d\phi}{dt} = \pi(t), \tag{B.1.2}$$

$$\frac{d\pi}{dt} = f[\phi(t)]. \tag{B.1.3}$$

As for ϕ, for example, one of the most simple numerical solution is just expanding it in Taylor series and erasing $\phi(t)$ by taking the sum, that is,

$$\phi\left(t + \frac{\Delta t}{2}\right) = \phi(t) + \dot{\phi}(t)\frac{\Delta t}{2} + \frac{1}{2!}\ddot{\phi}(t)\left(\frac{\Delta t}{2}\right)^2 + \cdots, \tag{B.1.4}$$

$$\phi\left(t - \frac{\Delta t}{2}\right) = \phi(t) - \dot{\phi}(t)\frac{\Delta t}{2} + \frac{1}{2!}\ddot{\phi}(t)\left(\frac{\Delta t}{2}\right)^2 - \cdots, \tag{B.1.5}$$

$$\therefore \quad \phi(t + \frac{\Delta t}{2}) = \phi(t - \frac{\Delta t}{2}) + \left[\dot{\phi}(t) + \mathcal{O}\left(\Delta t^2\right)\right]\Delta t, \tag{B.1.6}$$

$$= \phi(t - \frac{\Delta t}{2}) + \left[\pi(t) + \mathcal{O}\left(\Delta t^2\right)\right]\Delta t. \tag{B.1.7}$$

Obtaining the equation of π in a similar way, we can derive the formalism of the second-order symplectic integration scheme as

$$\phi(t + \frac{\Delta t}{2}) = \phi\left(t - \frac{\Delta t}{2}\right) + \left[\pi(t) + \mathcal{O}\left(\Delta t^2\right)\right]\Delta t, \tag{B.1.8}$$

$$\pi(t) = \pi(t - \Delta t) + \left(f\left[\phi\left(t - \frac{\Delta t}{2}\right)\right] + \mathcal{O}\left(\Delta t^2\right)\right)\Delta t. \tag{B.1.9}$$

As you can see from these equations, the future value at is calculated by the value between the future and the previous ones in a staggered way. That is why this integration scheme is called "leapfrog" method.

The application of the leapfrog method to a higher order is developed in Ref. [163]. We omit details of the derivation because of its complexity, but the formula is written as

$$\phi\left(t + c_i\Delta t\right) = \phi\left(t + c_{i-1}\Delta t\right) + \pi\left(t + d_{i-1}\Delta t\right)c_i\Delta t, \tag{B.1.10}$$

$$\pi\left(t + d_i\Delta t\right) = \pi\left(t + d_{i-1}\Delta t\right) + f\left[\phi\left(t + c_i\Delta t\right)\right]d_i\Delta t, \tag{B.1.11}$$

where $i = 1, \cdots, 4$ ($i - 1$ should be taken as 4 when $i = 1$) and

$$c_1 = c_4 = \frac{1}{2}\frac{1}{2 - 2^{1/3}}, \quad c_2 = c_3 = \frac{1}{2}\frac{1 - 2^{1/3}}{2 - 2^{1/3}}, \tag{B.1.12}$$

$$d_1 = d_3 = \frac{1}{2 - 2^{1/3}}, \quad d_2 = -\frac{2^{1/3}}{2 - 2^{1/3}}, \quad d_4 = 0. \tag{B.1.13}$$

We use this fourth-order formulation in simulations for the time evolution executed in Sec. 5.

B.2   Equations of Motion

As we saw in the previous section, because we use the symplectic integration scheme in the simulation, we should evolve the fields by Hamilton's equation. When the Lagrangian

is give by Eq. (B.0.2), the momentum density conjugate to $\phi(x)$ is defined by

$$\pi \equiv \frac{\partial \sqrt{-g}\mathcal{L}}{\partial \phi'} = a^{D-A}\phi'. \tag{B.2.1}$$

Then, Hamiltonian density is derived as

$$\mathcal{H} = \phi'\pi - \sqrt{-g}\mathcal{L}, \tag{B.2.2}$$

$$= \frac{1}{2}\frac{\pi^2}{a^{D-A}} + a^{D+A}\left[\frac{1}{2}\left(\frac{\nabla\phi}{a}\right)^2 + V(\phi)\right]. \tag{B.2.3}$$

Therefore, Hamilton's equations are obtained as

$$\phi' = \frac{\partial \mathcal{H}}{\partial \pi} = \frac{\pi}{a^{D-A}}, \tag{B.2.4}$$

$$\pi' = -\frac{\partial \mathcal{H}}{\partial \phi} = a^{D+A}\left[\frac{\Delta\phi}{a^2} - \frac{\partial V(\phi)}{\partial \phi}\right], \tag{B.2.5}$$

where we approximate $\Delta\phi$ by the fourth-order central differential scheme, which is calculated as, for example, in the x direction,

$$\frac{\partial^2\phi(x_i)}{\partial x^2} \simeq \frac{-\phi_{i-2} + 16\phi_{i-1} - 30\phi_i + 16\phi_{i+1} - \phi_{i-2}}{12\Delta x^2}, \tag{B.2.6}$$

where the lower indices show x positions $\phi_{i-2} = \phi(x_i - 2\Delta x)$, etc. and Δx is the grid spacing. We evolve these two Hamilton's equations by Eqs. (B.1.10), (B.1.11) in our simulation code.

B.3 Initial Conditions

Finally, let us summarize how we set the initial conditions in our simulation. Here, we denote the simulation start time as the lower index i.

When the parameter of the equation of state is expressed by w, the scale factor in the flat universe is described by

$$a(t) = \left(\frac{t}{t_i}\right)^{\frac{2}{3(1+w)}}, \tag{B.3.1}$$

$$\therefore \quad H = \frac{\dot{a}}{a} = \frac{2}{3(1+w)}\frac{1}{t}, \quad \tau = \int_0^t \frac{dt}{a(t)} = \frac{3(1+w)}{1+3w}\left(t_i^2 t^{1+3w}\right)^{\frac{1}{3(1+w)}}. \tag{B.3.2}$$

where the dot represents the physical time derivative and t and τ are physical and conformal time, respectively.

In lattice simulation of FRW universe, two parameters, the initial scale factor a_i and the initial time t_i, should be determined by hand to set the initial condition.

- The scale factor at the beginning of the simulation is generally normalized as 1, that is,

$$a_i = 1. \tag{B.3.3}$$

- The initial time is often determined by the condition $H_i = cm$ where c is some constant, which roughly corresponds to the time of the onset of the oscillation of a scalar field with mass m.

$$H_i = cm, \tag{B.3.4}$$

$$\Leftrightarrow \quad t_i = \frac{2}{3mc(1+w)}. \tag{B.3.5}$$

In conformal time,

$$\tau_i = \frac{3(1+w)}{1+3w} t_i = \frac{2}{mc(1+3w)}. \tag{B.3.6}$$

Under these condition, the evolution of the scale factor and Hubble parameter are calculated as [1]

$$a = \left[\frac{3c(1+w)}{2} mt\right]^{\frac{2}{3(1+w)}} = \left[\frac{c(1+3w)}{2} m\tau\right]^{\frac{2}{1+3w}}, \tag{B.3.7}$$

$$\left(\frac{H}{m}\right)^{-1} = \frac{t}{ct_i} = \frac{1}{c}\left[\frac{c(1+3w)}{2} m\tau\right]^{\frac{3(1+w)}{1+3w}}. \tag{B.3.8}$$

In this thesis, we simulate in the radiation dominated universe, i.e. $w = 1/3$, and use $c = 1$ for the initial time.

---

[1]Note that the relation between t and τ is simplified as

$$\frac{t}{t_i} = \left[\frac{c(1+3w)}{2} m\tau\right]^{\frac{3(1+w)}{1+3w}}.$$

Appendix C

Simulation Result

In this Appendix, we explain how the change of the threshold values $\overline{\rho}_{\text{th}}$ and the initial field values $\overline{\phi}_m$ affects our simulation results shown in Sec. 5.2. To reduce the computational time, we use different simulation parameters shown in Table C.1. Note that we performed the same calculations in two dimensions only for $p = 2$ and confirmed similar results.

C.1 Threshold Dependence

First, to observe the threshold dependence of simulation quantities, we show a result of the time evolution of the oscillon number N_{osc} and the oscillon energy ratio r_{osc} varying the threshold value $\overline{\rho}_{\text{th}}$. One of the results of, for example, $p = -1/2$ and $\overline{\phi}_0 = 5\pi$ is shown in Fig. C.1.1.

The left figure shows the number of oscillons. After the formation around $\overline{\tau} \sim 20$, N_{osc} slightly decreases until $\overline{\tau} \sim 40$ because of the damping of fluctuations by the gradient term and the cosmic expansion and the merger of the produced oscillons. By the end of the simulation N_{osc} becomes stable independent of the threshold values.

The right figure shows the time evolution of the fraction of oscillons to the total

Table C.1: Simulation parameters. Note that we also simulate in two dimensions only for $p = -1/2$.

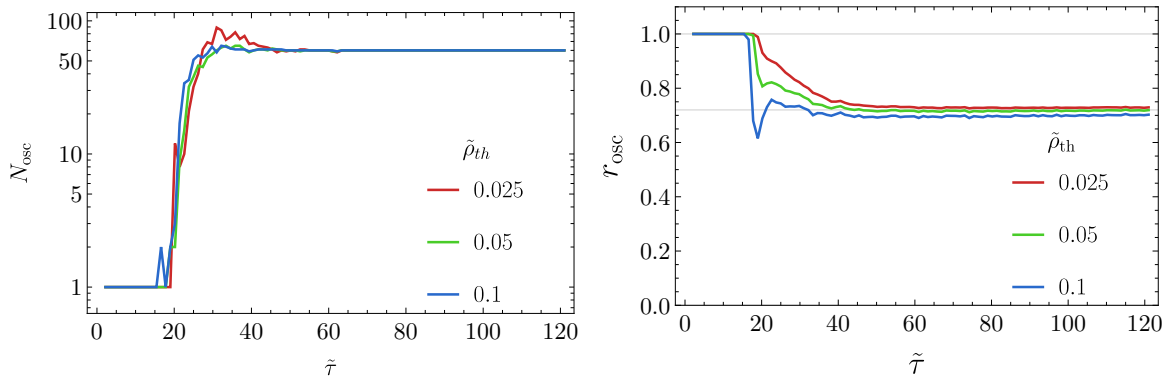|	Index p		
	$-3/4$	$-1/2$	2
Box Size L	8	4	4
Grid Size N	512^3	256^3	256^3
Time Step $\Delta\overline{\tau}$	4.0×10^{-3}	4.0×10^{-3}	4.0×10^{-3}
Final Time	81.0	121.0	121.0

Figure C.1.1: The time evolution of the number (left figure) and energy ratio (right figure) of oscillons. The red, green, and blue lines represent $\overline{\rho}_{\mathrm{th}} = 0.025,\ 0.05,\ 0.1$, respectively.

energy r_{osc}. As the same as N_{osc}, the energy ratio also becomes stable around $\overline{\tau} \sim 40$. Although r_{osc} gets smaller slightly when we use larger $\overline{\rho}_{\mathrm{th}}$ because of the tails of oscillon profiles, r_{osc} at the simulation end hardly depends on the threshold values.

From these two figures and other simulation results, we can conclude that the change of the threshold value by a factor of $\mathcal{O}(1)$ we use with our oscillon identification method hardly affect our simulation results.

C.2   Initial Field Value Dependence

Next, we examine the dependence of r_{osc} on the initial field value $\overline{\phi}_0$ by changing the initial field value and show how we determine $\overline{\phi}_0$ in Sec. 5.2.

Before the result, we briefly explain the mechanism of the fluctuation growth that deeply relates to oscillon formation. When the background field coherently oscillates as $\propto \cos mt$, the Fourier component of the field ϕ_k generally follows the well-known Mathieu equation,

$$\frac{d^2}{d(mt)^2}\phi_k + [A_k - 2q\cos(2mt)]\phi_k = 0, \tag{C.2.1}$$

where A_k and q depend on the shape of the potential of the field. It is well known that the field value ϕ_k is exponentially amplified when $A_k \simeq 1, 2^2, \cdots$, and so on. This instability is called parametric resonance [45, 46, 47] and the major process to produce oscillons. The oscillon formation becomes effective when the perturbations with the wavelength of the oscillon size are amplified enough by the parametric resonance. If these instabilities amplify the perturbations up to $\mathcal{O}(1)$, oscillon can be formed.

On the other hand, ϕ_k is also exponentially amplified when the second term of Eq. (C.2.1) is negative. This instability is called tachyonic instability because the effective mass becomes negative, which hinders the coherent oscillation necessary for the oscillon formation. In the case of the potential we use Eq. (5.2.1), the effective mass
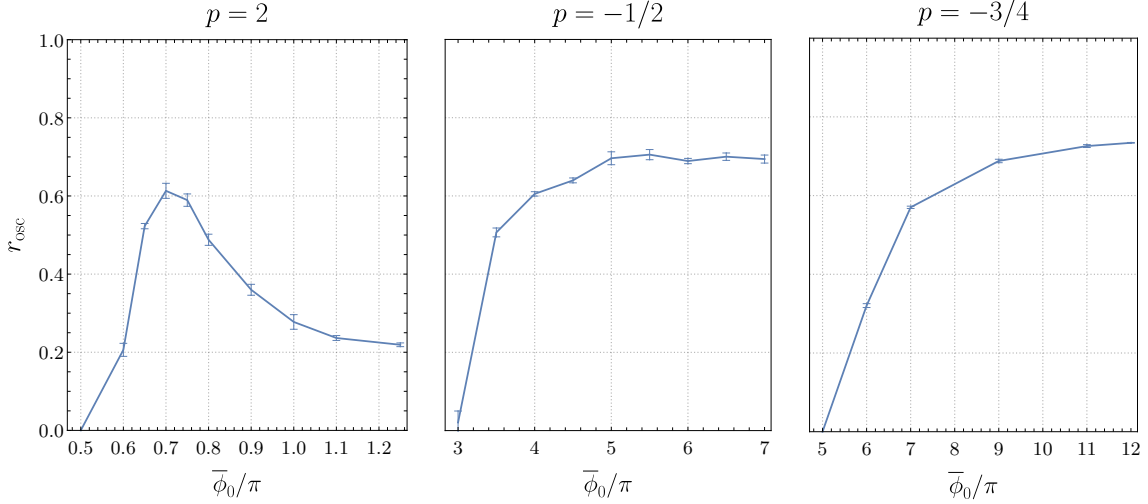
Figure C.2.1: The oscillon energy ratio with different index p and initial field value $\overline{\phi}_0$. The error bars show the variance over three times of simulations with different random seeds.

becomes negative only when

$$\frac{\partial^2 V}{\partial \phi^2} < 0 \quad \Leftrightarrow \quad \frac{\phi}{F} > \frac{1}{\sqrt{1+2p}} \equiv \frac{\phi_c}{F}. \tag{C.2.2}$$

Thus, when $p > -1/2$, the tachyonic instability occurs and could prevent the oscillon formation.

Based on the above discussion, let us see Fig. C.2.1 which shows $r_{\rm osc}$ as a function of $\overline{\phi}_0$ for each p. For a small $\overline{\phi}_0$, $r_{\rm osc}$ ends up in zero because the instability growth is too small for oscillon formation. For a larger $\overline{\phi}_0$, $r_{\rm osc}$ gets larger because the parametric resonance becomes more effective. For $p \leq -1/2$, $r_{\rm osc}$ converges on a plateau of which typical field value is defined as the initial field value in Sec. 5.2. On the other hand, because the tachyonic instability amplifies the modes different from the oscillon size when $p > -1/2$, the subsequent oscillon formation is hindered. Therefore, the oscillon formation rate has a peak at some value of $\overline{\phi}_0$ and we define it as the initial field value in Sec. 5.2. [1] Note that we perform the same analysis in two dimensions with $p = -1/2$ and obtain $\overline{\phi}_0 = 5\pi$.

---

[1]To confirm the effect of tachyonic instability, we calculate $r_{\rm osc}$ with smaller initial noise $\mathcal{P}_\xi$ for $p = 2$. When $\overline{\phi}_0$ is larger than the peak value, $r_{\rm osc}$ increases because the small initial noise delays the tachyonic instability. On the other hand, when $\overline{\phi}_0$ is not more than the peak value, $r_{\rm osc}$ decreases because $\overline{\phi}_0$ is small enough to avoid the tachyonic instability and the small noise just results in a smaller amount of oscillons. This result is consistent with the effect of tachyonic instability.